Master's thesis

2021

Marcus Hoseth Bentzen

Master's thesis

NTNU
Norwegian University of
Science and Technology
Faculty of Natural Sciences
Department of Materials Science and Engineering

NTNU
Norwegian University of
Science and Technology

Marcus Hoseth Bentzen

Aerosol Deposited Piezoelectric Ceramic Coatings for Biomedical Applications

Master thesis in Structural Chemistry
Main Supervisor: Assoc. Prof. Julia Glaum
Co-supervisor: Dr. Magnus Rotan

June 2021

NTNU
Norwegian University of
Science and Technology

Abstract

The objective of this Master thesis was to develop a post-processing procedure for aerosol deposited $BaTiO_3$ on 304SUS stainless steel and Ti6Al4V alloy substrates with the goal of improving biomedical in-vivo functionality.

Commonly used biomaterials such as 304SUS stainless steel and Ti6Al4V alloy have high mechanical strength, corrosion resistance and wear properties, which protect them from degradation within the harsh conditions found in the human body. However, neither of these two materials interact actively or beneficially with the tissue surrounding them in-vivo and as such are left susceptible to loosening and chemical reactions leading to implant failure or toxic effects.

This thesis consequently aims to improve the bioactive properties of ceramic coatings deposited onto bioinert metal substrates with aerosol deposition by developing a post-processing heat-treatment procedure. The aerosol deposition method generally results in coatings containing nano-sized crystallites which are detrimental to the electrical properties of materials such as barium titanate ($BaTiO_3$). Therefore, this thesis attempted to induce temperature dependent consolidation of the coating and increase the crystallite sizes in order to enhance the coating's electrical properties such as the generation of surface charge under stress.

The generation of surface charge has been linked with enhanced bone-mineralization and proliferation of osteoblasts on biomedical implant surfaces and, as a result, increasing biocompatibility and implant fixation. This is achieved through shielding the implant from its chemically harsh surroundings by the formation of bone-like calcium phosphates on electrically active surfaces and bonding it to surrounding tissues through the formation of collagen fibers in the calcium phosphate layer.

Heat-treatments were found to improve electrical properties with the best polarization behavior and emergence of ferroelectric character occurring at applied temperatures of 750 °C for $BaTiO_3$ deposited on stainless steel. These changes were linked to temperature-induced microstructural changes observed by scanning electron microscopy (SEM), such as grain growth on the coating surface and fusing of coating particles observed at the coating-substrate interface.

However, different material combinations revealed a strong dependence of sample mechanical integrity on the choice of substrate as thermal expansion mismatch between the coating and substrate lead to the degradation of the coating at elevated temperatures. This was apparent through the loss of contact at the coating-substrate interface and the introduction of cracks and voids. These defects were observed both in the SEM and when subjecting the samples to nano-indentation.

Nano-indentation showed that coating consolidation and densification was achieved, but the average mechanical properties did not improve much due to the introduction of defect and inhomogeneities causing large variations in the measurement. XRD, ToF-SIMS and EDS analysis revealed that the heat-treatment temperatures were generally insufficient to create new chemical products. However, some diffusion of elements from the metal substrate into the ceramic coatings was observed in the form of depletion regions at the interface and aggregation at the coating surface.

A subsequent soaking study, where heat-treated and charged $BaTiO_3$ samples were submerged into simulated body fluid (SBF) for seven days, revealed complete dissolution of the coatings depending on the degree of surface charge. These findings suggest that aerosol deposited $BaTiO_3$ does not provide beneficial bioactivity to metal substrates in-vivo, but more research is needed to understand the chemistry and kinetics of the coating dissolution.

Sammendrag

Formålet med denne masteravhandlingen var å utvikle en prosedyre for post-prosessering av aerosol deponert $BaTiO_3$ på 304SUS rustfritt stål og Ti6Al4V legering substrater med mål om å forbedre biomedisinsk funksjonalitet in-vivo.

Biomaterialer som 304SUS rustfritt stål og Ti6Al4V legering er kjent for å ha høy mekanisk styrke, korrosjonsmotstand og slitasjeegenskaper som til sammen beskytter dem mot degenerasjon i de tøffe kjemiske forholdene i kroppen. Til tross for dette er begge materialene sårbare for kjemiske reaksjoner som kan føre til giftige biprodukter og har en tildens til å løsne fra vertsvevet hvis de er implantert lenge nok. Dette skyldes en mangel på gunstige interaksjoner mellom implantatsmaterialet og nærliggende vev.

Denne masteravhandlingen sikter derfor mot å forbedre de bioaktive egenskapene til bioinerte metallsubstrater ved å utvikle en varmebehandlingsprosedyre for aerosol deponerte keramiske belegg. Aerosol deposisjon metoden produserer vanligvis belegg med krystallitter i nanostørrelse, noe som forverrer de elektriske egenskapene til materialer som bariumtitanat ($BaTiO_3$). Denne masteravhandlingen har derfor forsøkt å produsere varmeavhengig konsolidasjon og økning i krystallittstørrelsene for å forbedre de elektriske egenskapene til belegget som generering av overflateladninger under påført stress.

Genereringen av overflateladninger har blitt knyttet til forbedret beinmineralisering og proliferasjon av osteoblaster på biomedisinske implantater, noe som fører til økt biokompatibilitet og fiksering av implantatet. Disse effektene kommer av at elektrisk aktive belegg kan beskytte implantater fra de kjemisk tøffe forholdene i menneskelig kroppsvæske ved å initiere formasjon av kalsiumfosfat på overflaten. Kalsiumfosfat er kjemisk likt bein og fremmer binding med kollagen fibere, noe som forbedrer forbindelsen til vertsvevet.

Varmebehandlingene forbedret beleggets elektriske egenskaper. Den beste polariseringsresponsen og utvikling av ferroelektriske egenskaper ble observert etter varmebehandling på 750 °C for $BaTiO_3$ deponert på rustfritt stål. Disse egenskapene ble koblet til mikrostrukturelle endringer observert med elektronmikroskop (SEM) som partikkelvekst på beleggoverflaten og fusjon av partikler ved belegg-substrat interfasen.

De ulike materialkombinasjonene viste en sterk sammenheng mellom valg av substrat og prøvenes mekaniske integritet ettersom ulikheter i termisk ekspansjon førte til at belegget ble revet i stykker på høye temperaturer. Dette ble observert med SEM som en økt forekomst av sprekker og hull samt tap av kontakt i belegg-substrat interfasen etter varmebehandlingene.

Nanoinduksjon målte en økning i konsolidasjon og fortetning i belegget, men de gjennomsnittlige mekaniske egenskapene ble ikke bedre som følge av ulikheter i målingene etter introduksjonen av sprekker. Røntgendiffraksjon, ToF-SIMS og EDS analyse viste at varmebehandlingene var generelt sett ikke høye nok til å skape nye kjemiske biprodukter. Noe diffusjon be observert mellom substratet og belegget i form av legeringselementer i form av utarming ved interfasen og aggregering på overflaten til belegget.

En studie av $BaTiO_3$s effekt i simulert kroppsvæske ble gjennomført ved å introdusere en vedvarende elektrisk ladning til beleggets overflate før prøven ble lagt i kroppsvæsken i syv dager. Dette førte til at belegget gikk i komplett oppløsning basert på styrken til overflateladningen. På grunn av dette kan en anta at aerosol deponert $BaTiO_3$ ikke tilbyr gunstig bioaktivitet til metallsubstrater in-vivo, men mer forskning trengs for å forstå de underliggende kjemiske reaksjonene og kinetikken som førte til at belegget gikk i oppløsning.

Acknowledgements

My heartfelt gratitude goes out to my supervisors Assoc. Prof. Julia Glaum and Dr. Magnus Rotan, whose encouragement, guidance and scientific input has been invaluable. In addition to my supervisors I would like to thank the wider FACET group at NTNU whom I would meet with every week. Their interest and input into my work, which often differed from their own, was thoroughly appreciated and valuable. Thank you to all the engineers and laboratory staff at NTNU who trained me in the use of the different instruments used to characterize my samples. A special thanks goes to Yingda Yu at the Electron Microscopy Lab who spent much of his valuable time facilitating my work during a period of time when booking equipment was difficult.

Lastly, this thesis would not have been possible without the assistance of several amazing collaborators. Dr. Anja Henß at the Justus-Liebig University kindly performed time-consuming ToF-SIMS which increased my understanding of my samples' diffusion behavior, while Prof. Jianying He and the NTNU Nanomechanical Lab performed a large number of important nanoindentation measurements. Lastly, I want to especially thank Dr. Neamul Khansur, Udo Eckstein and Juliana Maier from the Functional Ceramics group at the Friedrich-Alexander Universität Erlangen in Germany for producing the aerosol deposited samples used in this thesis, and offering valuable insight into my work.

List of Figures

List of Tables

Contents

1 Introduction

Orthopedics often involve the use of implanted biomaterials, which can be defined as any material which has been engineered to interact with a biological system for a medical purpose, either for diagnosis or treatment. In orthopedics, these materials are generally used to repair or replace damaged hard-tissues such as bone with the goal of restoring function and improving patient quality of life. The extensive use of biomaterials seen today for applications such as the correction of fractures or the replacement of joints was not possible before the advent of safe anesthesia, sterilization of implants and improvement of implant material properties seen in the mid-20th century [5]. The invention of the modern hip-replacement by Sir John Charnley in the 1960s [6, 7] formed the basis of what is now a multi-billion dollar industry, with approximately 2.9 million joint replacement surgeries being performed annually worldwide [8].

Generally, two classes of materials have been used for such applications, metals and ceramics. Metals are chosen based on their high strength and fracture toughness, making them ideal for load-bearing and articulating implants, while ceramics can stay implanted for for long periods of time due to their low toxicity within the body [9, 10]. Historically there has been three generations of biomaterials [11]. The first generation included biotolerant and bioinert materials whose main function was to simply replace damaged or missing tissue, titanium alloys are examples of this generation. The second generation of materials, represented by bioglass were characterized by being responsive to biological systems and mainly concerned with offering a substrate for bone bonding and for bone-forming cells (osteoblasts) to attach. Lastly, the third generation seeks to actively instruct the biological system for instance by inducing the formation of new bone, facilitating biomolecule delivery and engineering tissues. This last generation is currently being developed and often involves the functionalization of "tried and true" first generation materials such as load-bearing metals.

This master thesis is therefore concerned with the development and characterization of aerosol deposited piezoelectric/ferroelectric ceramic coatings on metal substrates. The objective of the thesis is to develop functional barium titanate $BaTiO_3$ coatings on Ti6Al4V and 304SUS stainless steel substrates using aerosol deposition (in collaboration with Prof. Kyle Webber, Friedrich-Alexander University, Erlangen, Germany) for use in biomedical hard-tissue applications, mainly orthopedics.

The motivation for this thesis is to improve the interaction of load-bearing metallic implants with surrounding hard-tissues through the use of electrically active coating materials such as $BaTiO_3$ in order to enhance the initiation of bone mineralization. It is believed that this will enhance the lifetime of the respective metallic implant materials and improve patient welfare through added corrosion resistance, elevated biocompatibility, mechanical adhesion and integration into surrounding tissues.

The aerosol deposition processing method was chosen based on its industrial potential, low processing temperatures, compatibility with almost any substrate, relatively low cost and high speed of deposition. The characterization methods used in this thesis were chosen in order to evaluate the microstructure, chemical composition, electrical properties, mechanical properties and chemical activity of the coated samples which all have an effect on the final functionality of the sample.

2 Theory

2.1 Biomaterials intended for hard tissue applications

If a biomaterial is to be suitable for hard-tissue applications, it must successfully mimic the properties of bone and ideally, improve upon them. Saini [9] proposed a list of bulk and surface properties which are vital to the success of a bone-replacement implant. The desired bulk properties are generally concerned with maintaining the overall mechanical and structural integrity of the implant.

First, the material must have an elastic modulus similar to bone (7-30 GPa [12]), that is the material's ability to resist non-permanent deformation when subjected to an applied stress. This is vital for the proper distribution of stress within the implant to minimize the amount of movement between it and surrounding hard tissues in order to keep the implant in place. Secondly, the implant should have high compressive and tensile strength in order to prevent fracture and damage to the implant, as well as high yield strength to ensure that the implant retains its shape under cyclic loading and does not deform. Third, the material needs to have a minimum ductility of 8% in order to be shaped into the often complex shapes found in the biological systems. Lastly, the material needs to have a high hardness value in order to decrease wear and the release of particles into the body. The prevention of particle release from the implant is especially important as it is one of the main reasons for modern implant failure as the released particles cause osteolysis (destruction of bone), inflammation and infection in surrounding tissues [13].

Surface properties are more focused on the interactions the implant has with the surrounding environment. The first surface property of import is surface energy. Surface energy is the work associated with the appearance of a unit area of surface [14] and is particularly important if the implant material possesses nano-sized features as nanomaterials have a high surface are relative to their volume. High surface energy is a result of atoms and molecules in a material's surface region having fewer nearest neighbours (i.e. lower coordination numbers) than atoms and molecules within the bulk of the material. This leads to the surface region containing unsatisfied (often called "dangling") chemical bonds, making it thermodynamically metastable or unstable. As such, biomaterials with high surface energy will tend to undergo changes which reduces surface energy such as restructuring itself (e.g. sintering at elevated temperatures, explained further in section. 2.5.1) or by forming new chemical bonds with surrounding tissues. Because of this effect, an implant material will often be roughened or smoothed in order to minimize or maximize the surface energy.

The second important surface property which runs slightly counter to the surface energy is corrosion resistance as maximisation of surface energy increases reactivity while increased corrosion resistance is generally associated with the surface being inert. The inside of the human body is a remarkably harsh chemical environment [15] it contains dissolved oxygen, hydronium and various ions such as chloride, and hydroxide (the concentrations of some of these ions in blood plasma can be found in Table. 3.8). As such, any material implanted into this environment needs to be able to withstand chemical attack from these species at an average temperature of 36.5 °C.

The last important property is the biocompatibility of the implant material and is closely linked with corrosion resistance. Corrosion of biomaterials lead to the leaching of the elements making up the material into the surrounding medium, which depending on the element can have dire consequences as they might interact with the bodies in a way which causes toxic effects (section 2.4). As such, there is a balance between the various surface properties which leads to materials either being bioactive or bioinert, meaning that the material reacts with its biological surroundings, or does not.

The most famous bioinert material used in hard-tissue application is the medical grade titanium alloy Ti6Al4V [16] while bioactive materials are often different kinds of ceramics which can be functionalized such as perovskites [17]. Generally speaking, the Ti6Al4V and other metals have superior mechanical properties to ceramics and are therefore used in load-bearing or mechanically demanding hard-tissue applications. However, bioinert materials largely remain as foreign objects in the body as they do by design not interact with surrounding tissue. Bioactive materials such as ceramics on the other hand can be made to react with their surrounds in targeted ways which full integrates the material, yet these materials are often not suitable for load-bearing applications and are susceptible to brittle fracture.

A potential solution to this issue is to combine load-bearing, largely bioinert metals with bioactive ceramics as substrates and coatings respectively. One class of coating materials which is of considerable interest is piezoelectrics.

2.2 Electromechanical effects

2.2.1 Piezoelectricity

Piezoelectricity can be observed in the form of the direct and indirect piezoelectric effect. The direct effect (Fig. 2.1a) occurs when a piezoelectric material is subjected to mechanical stress, and responds by developing a surface charge without the presence of an external electrical field. Conversely, the indirect piezoelectric effect (Fig. 2.1b) occurs when an external electrical field is applied, resulting in a change in the material's dimensions.

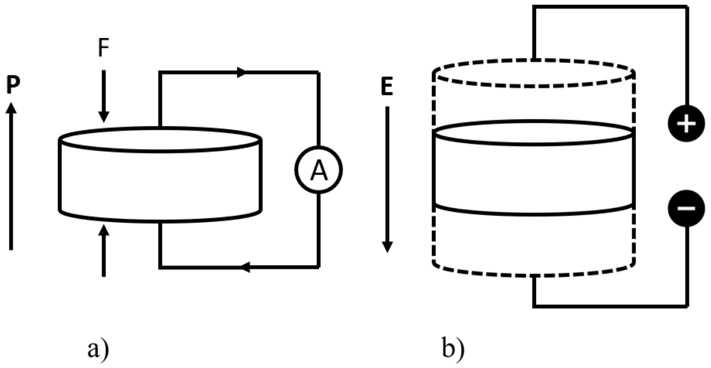

Figure 2.1: Direct (a) and indirect (b) piezoelectric effects, with the dotted lines indicating the original dimensions of the sample. Adapted from [1].

The piezoelectric effects can be understood mathematically as the derivative of polarisation with respect to strain, but when simplified the direct and indirect effects can be represented as:

$$D = dX + \epsilon^X E \tag{2.1}$$

$$S = s^E X + dE \tag{2.2}$$

Where D is the displacement or generated charge, S is the mechanical strain, X is mechanical stress, ϵ^X is the permittivity measured at constant stress, s^E is elastic compliance and E is the electric field [18]. Lastly d denotes the piezoelectric coefficient which is dependent on several properties of a given material and quantifies the magnitudes of either the direct effect (as dielectric displacement per unit stress (C/N)) or the indirect effect (as strain per unit voltage (m/V)) [19].

However, the piezoelectric coefficient is itself very complex as the piezoelectric effect is highly an-isotropic due to the directional nature of applied stress and the crystal structure. Because of this, the induced polarization will depend heavily on the stress tensor and the orientation of the crystal, resulting in 27 different moduli (d_{ijk}) [20]. This is further complicated by the fact that depending on the symmetry operators within the unit cell, there might be several points of redundancy with moduli being equal to each-other or having a value of 0.

Consequently one would not expect piezoelectricity to be observed in poly-crystalline materials as individual, differently oriented grains/domains should polarize in random directions and cancel out. Ironically, many piezoelectric materials are poly-crystalline, and so this issue is circumvented by poling the material.

Poling involves heating the material past its Curie temperature (T_C), above which the material loses its piezoelectric behavior, and cooling them after in a strong applied electric field. This orients the dipoles in a way which creates an observable piezoelectric effect, with one of the most frequently used orientations corresponding to the d_{33} modulus.

These effects are an emergent property of distortions in the crystal structure of the ceramic and is found in 20 non-centrosymmetric point-groups [20]. This is well illustrated in the perovskite class of materials.

The perovskite structure refers to it being isostructural with the mineral perovskite ($CaTiO_3$) with a generalized structure of ABO_3. This bonding structure can be represented by an idealized close-packed cubic arrangement (Fig. 2.2). In this representation, the large cations (A, blue) are located in the corners with 12-fold coordination, small cations (B, green) are located at the body centre with 6-fold coordination, and lastly the face-centered anions (O, red) form octahedra surrounding the small cations (B, green).

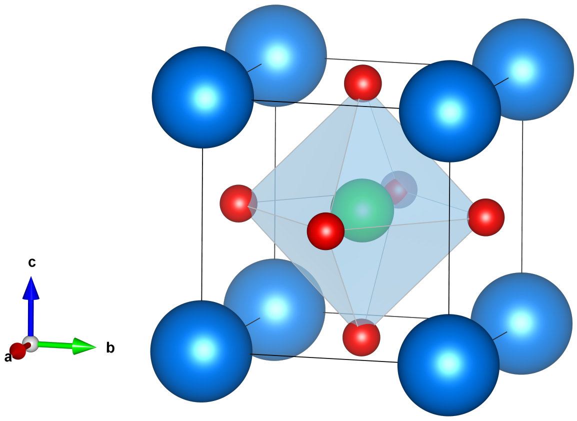

Figure 2.2: Idealized cubic structure of a perovskite.

The relationship between atomic radii and how they fit within the unit cell can be described by the Goldschmidt tolerance factor which is given by the following expression [18]:

$$t = \frac{R_A + R_O}{\sqrt{2}(R_B + R_O)} \tag{2.3}$$

Where R_A, R_B and R_O denotes the atomic radii of species A, B and O respectively, while t is a "tolerance factor". This value is a ratio which denotes the size of ion the structure can accommodate within its octahedra. Piezoelectrics generally have a tolerance factor between $0.955 < t < 1.06$. When $t \neq 1$ the unit cell distorts in order to accommodate the mismatch and increased lattice energy.

These distortions is what in turn generate the polarization seen in piezoelectric materials through a loss of centro-symmetry. In the idealized cubic structure (Fig. 2.2) any polarization within the crystal will come out to a net zero due to its centre of symmetry. This occurs because any dipole vector it may have in one direction will be cancelled out by a corresponding dipole in the opposite direction. However, if the crystal is distorted into a tetragonal structure by the elongation of one of its lattice vectors (Fig. 2.3), the dipoles no longer cancel each-other, leading to a net charge development.

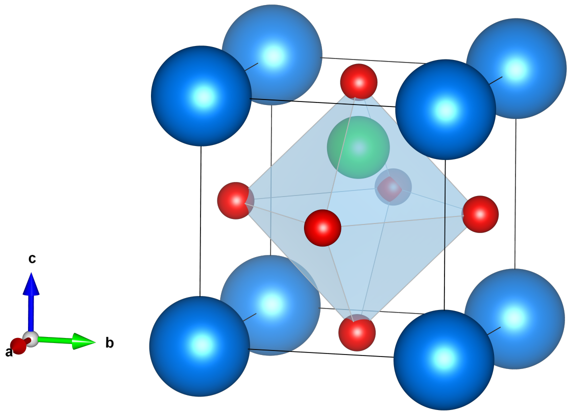

Figure 2.3: Unit cell of an idealized tetragonal perovskite.

2.2.2 Piezoelectricity and ferroelectricity in ceramics

Having explained piezoelectricty in general as a crystal property, it is important to know that there are additional considerations for piezoelectric ceramics. Ceramics are often not single crystals, but rather polycrystalline amalgamation and made up of randomly oriented grains in different shapes and sizes [20]. Because the grains are randomly oriented, any developing polarization under stress will be randomly oriented as well resulting in a net-zero polarization and the absence of an observable piezoelectric effect.

Perovskites however, are not just piezoelectric, but belong to a sub-class of materials called ferroelectrics. What separates a ferroelectric from a piezoelectric is that in addition to not having centro-symmetry ferroelectric have a unique polar axis as well. This allows ferroelectrics to not just have an induced polarization under strain, but to have a spontaneous polarization in the absence of external stress or electric fields [20]. This polarization arises in distorted perovskites due to the central B-site ion being able move along one of two equivalent directions within the octahedral void producing a permanent charge separation (Fig. 2.4).

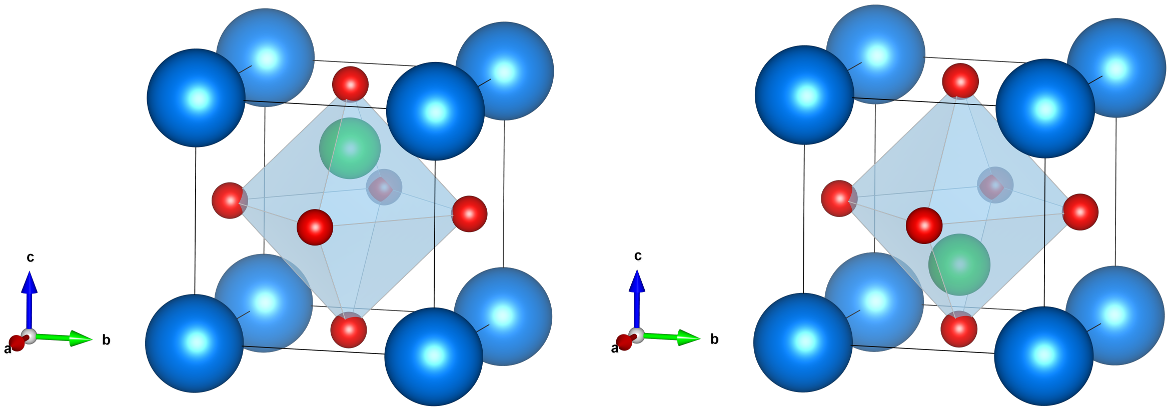

(a) Ferroelectric configuration one (b) Ferroelectric configuration two

Figure 2.4: Movement of central B-site (green) ion within the octahedral void of a perovskite in the direction of an applied electric field.

This gives rise to two energetically equivalent structural confirmations which each represent a potential energy minima separated by an energy barrier. A crystal within a ferroelectric material can occupy either of these two states at random, but local interactions between adjacent crystals will reduce the overall free energy of the structure by aligning their local dipoles in the same direction. These local groupings are called domains and are separated from other spatially oriented dipole groupings by a boundary called a domain wall (Fig. 2.5).

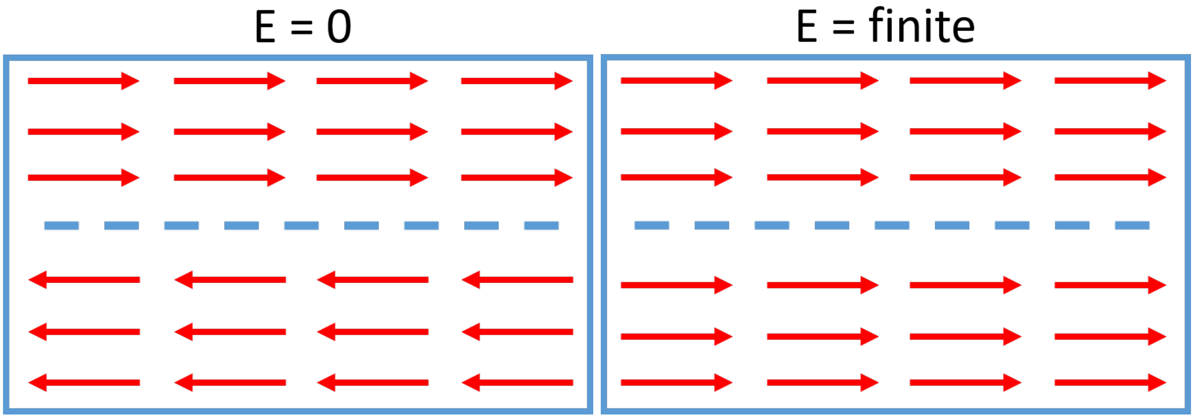

(a) Unaligned domains (b) Switched domains

Figure 2.5: Unaligned and aligned domains before and after the application of an external electrical field. The blue dashed lines denote the domain walls.

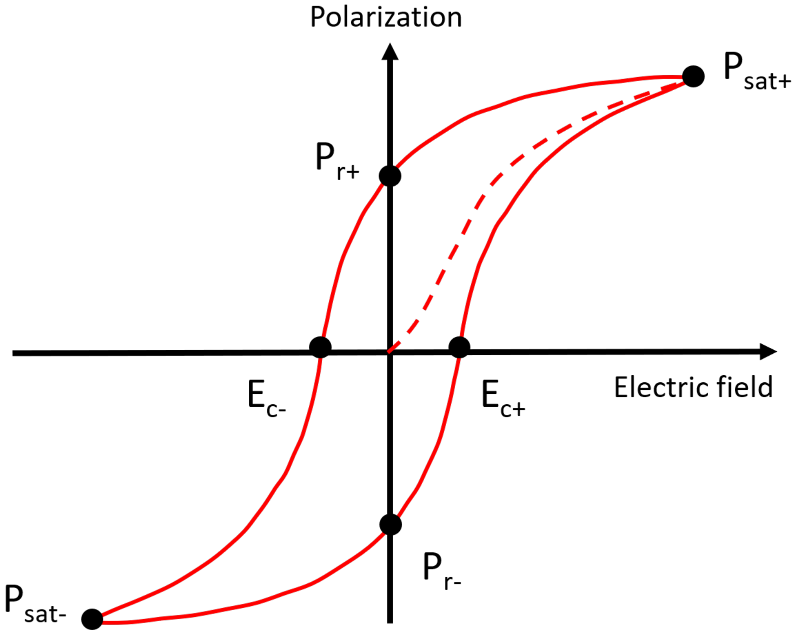

Figure 2.6: Example of a ferroelectric hysteresis curve.

These randomly oriented domains can all be brought into the same alignment/state if a large enough electric field is applied to overcome the associated energy barrier. This phenomenon is called "switching" and results in hysteresis behavior as seen in Fig. 2.6. Where E_c is the coercive electric field, i.e. the electric field strength needed to overcome the energy barrier and start switching domains. Once all domains have been switched one reaches the saturation polarization P_{sat} at which point increasing the applied electric field will not yield further polarization. Once the field is removed, the domains largely settle within their new orientations and retain a certain amount of polarization, this is called remanent polarization P_r.

2.3 Electrically active bone implant materials

Ferroelectric materials can be utilized to improve the biocompatibility and integration of implant materials by exploiting the initiation mechanism for bone mineralization and proliferation. Bone is generally described as a inorganic composite of hydroxyapatite which is a class of calcium phosphate with the general formula $Ca_{10}(PO_4)_6(OH)_2$ in an organic collagen matrix [17]. This composite can take on two major forms, either compact bone which forms the dense outer parts, or cancellous bone which forms a porous inner network within the core. The compact bone layer is what gives bone its load-bearing properties while cancellous bone allows for the presence of marrow and the production of new blood-cells [17].

It is well established that bone is a "living" material and constantly renews itself through the attachment of bone-forming cells called osteoblasts [17]. The processes of osteoblast attachment and proliferation is complex but can be simplified as the attraction of osteoblasts to the bone surface by an electrical attraction, followed by chemical bonding between the proteins of the osteoblast and the surface hydroxypapatite layer of the bone [21]. This initial electrical attraction was attributed to the generation of surface charge by the piezoelectric effect in collagen fibers as bone is stressed already in 1957 by Fukada and Yasuda [22].

Consequently, the literature has suggested for a long time that bone proliferation is therefore improved by the enhanced generation of surface charge if bone is frequently stressed. One observed effect which supports this is the significantly higher reported bone density in athletes compared to non-athletes and is even more pronounced in strength athletes who subject their bones to higher levels of stress by lifting heavy loads [23–25].

The ability of a surface charge to attract oppositely charged species at a distance stems from the formation of an electric double layer (Fig. 2.7). The electric double layer results from the build-up of surface charge in a material which creates an electrostatic potential which propagates into its surroundings. The potential will attract opposite charges (counter-ions) and repel similar ones (counter-ions) forming three main regions called the Stern layer, the diffuse layer and the bulk of the solution or medium [26].

The Stern layer is an immobile region relative to the charged surface and is made up of a layer of counter-ions which are interacting with the surface. The diffuse layer is the region at a certain distance from the surface where the surface charge of the biomaterial has an effect on charged species (i.e. the potential). The bulk of the solution is the region where the potential of the charged surface goes to zero. The size and potential of these regions are dependent on the magnitude of the surface charge and and the permittivity of the surroundings.

It is this effect which is exploited by ferroelectric biomaterials. A ferroelectric can either generate surface charge through stress or it can retain a high remanent polarization by the application of a high enough electric field. This allows ferroelectrics such as barium titanate $BaTiO_3$ to attract calcium and phosphate ions from surrounding body fluid when implanted. This leads to the formation of various calcium phosphates on the surface of the ceramic which in mimics bone allowing for future bonding with proteins and subsequently osteblasts [27]. Because of this, calcium phosphate formation onto piezoelectric and ferroelectric ceramics is considered an indication of improved bioactivity. However, in order to be able to test the efficacy of different calcium phosphate forming materials without conducting expensive and complicated in vivo trials, the simulated body fluid (SBF) was developed [28, 29].

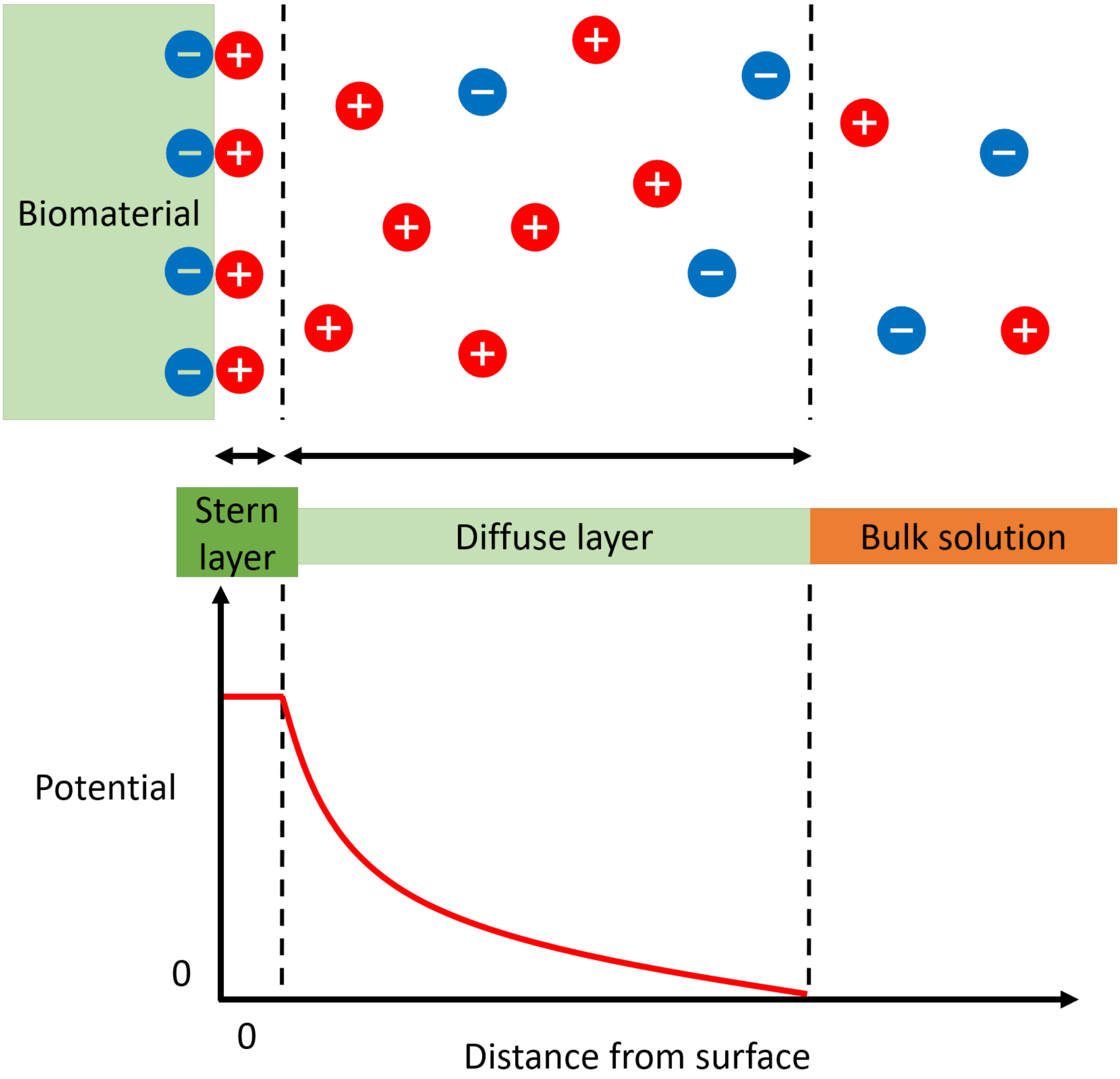

Figure 2.7: Diagram of the electric double layer (EDL) showing the distribution of ions and the potential at a given distance from the surface.

SBF is a prepared supersaturation with respect to calcium phosphate formation which mimics the consentrations of human blood plasma (Table. 3.8). Standard procedure in trials utilizing SBF to asses the calcium phosphate formation onto a biomaterial generally involves the material being submerged in SBF for a pre-determined amount of time and measuring the amount of calcium phosphate present on its surface after retrieval [28, 29].

Due to the desired bulk properties mentioned in section 2.1 and the efficacy of ferroelectrics in biological systems one can combine metal implants with ceramic coatings in order to account for the inherent weaknesses of each class of material. As such, this thesis combines aerosol deposited $BaTiO_3$ with 304SUS stainless steel and Ti6Al4V titanium alloy.

2.4 Materials in this study

2.4.1 Barium titanate

Barium titanate $BaTiO_3$ was the first ferro-piezoelectric oxide with perovskite structure, as well as the first non-hydrogen bonded ferroelectric to be discovered and has been thoroughly studies since [30, 31]. $BaTiO_3$ has a paraelectric cubic ($Pm\bar{3}m$) structure as seen in Fig. 2.2 above its Curie temperature (T_C: approx. 130 °C) but, as it cools to temperatures lower than 130 °C it transitions into a P4mm ferroelectric tetragonal structure [32]. As such, $BaTiO_3$ is ferroelectric within the operating temperature range of the human body which is 36.5 °C on average. As a biomaterial, $BaTiO_3$ is well known for being highly biocompatible due to the low toxicity of its composite Ba^{2+} and Ti^{4+} ions [33] and for its efficacy in calcium phosphate formation resulting from its high piezoelectric coefficient $d_{33} = 350\,\mathrm{pC/N} - 500\,\mathrm{pC/N}$ and dielectric constant of 4000 (for bulk ceramics) [32, 34–36]. Based on these properties, $BaTiO_3$ should make an excellent coating material, however it should be noted that as it is a ceramic it has undesirable mechanical properties such as susceptibility to brittle fracture [37]. Apart from this, bulk $BaTiO_3$ has a compressive strength and elastic modulus well over that of bone (Table. 2.1). Furthermore, there are reported issues with the solubility of $BaTiO_3$ in water due to perovskites not being thermodynamically stable in aqueous solution on account of the structure's ionic character [38].

Table 2.1: Bulk properties of $BaTiO_3$ compared to bone.

Material	σ_c [MPa]	E [GPa]
$BaTiO_3$	656-913 [39]	115 [39]
Compact bone	100-230 [12]	7-30 [12]
Cancellous bone	2-12 [12]	0.005-0.5 [12]

2.4.2 304SUS stainless steel

Stainless steel is a generic term which encompasses multiple alloys of iron with varying amounts (11-30 wt%) of chromium [40]. The stainless steel used in this thesis is 304SUS stainless steel which is known for its high corrosion resistance and is commonly found in temporary implants after physical bone trauma such as screws, fracture plates and hip-nails [16]. This is mainly due to the material's low cost and good bulk properties when compared to bone (as presented in section 2.1) shown in Table 2.3.

However, the pervasive issue with 304SUS stainless steel and why it is only used in temporary implants is its relatively low biocompatibility compared to other alloys such as Ti6Al4V based on its tendency to corrode within the body [40]. The relatively low biocompatibility of 304SUS stainless steel can be explained by the leaching of its alloying ions over time (Table. 2.2), but chromium and nickel are especially problematic.

Table 2.2: Elemental composition of 304SUS stainless steel [3].

$C \leq$	$Si \leq$	$Mn \leq$	$P \leq$	$S \leq$	Cr	Ni
0.08	1.00	2.00	0.045	0.030	18.00-20.00	8.00-10.50

Table 2.3: Bulk properties of 304SUS stainless steel compared to bone.

Material	σ_c [MPa]	E [GPa]
304SUS stainless steel	205-310 [41]	190-203 [41]
Compact bone	100-230 [12]	7-30 [12]
Cancellous bone	2-12 [12]	0.005-0.5 [12]

Chromium

Although chromium is vital to the corrosion resistance of 304SUS stainless steel through the formation of a chromium oxide passivation layer [42, 43], it is still possible for chromium to leach into surrounding mediums if given enough time. Chromium is released into the body either in its Cr^{3+} or Cr^{6+} oxidation states. The Cr^{3+} state is water insoluble and an essential trace element in the body for the metabolism of insulin and the creation of the glucose tolerance factor [44, 45]. As such Cr^{3+} does not pose a health risk [16]. The Cr^{6+} state on the other hand is a well-documented toxin and carcinogen due to it being a strong oxidation agent which can cause apoptosis, specific gene mutations and prevention of gene repair [44, 45]. Despite this, the danger posed by chromium leaching is offset enough by the small diffusion constant of chromium in steel that it can be used as an implant material temporarily [46].

Nickel

Similar to chromium, nickel is added to stainless steels in order to increase their resistance to corrosion [16]. Specifically, nickel stabilizes the austenite structure if iron within the stainless steel and forms passivation films similar to chromium [40]. However, nickel is also highly toxic to humans [47], but while chromium toxicity is mainly connected to chromium ions, nickel toxicity is related to nickel containing compounds rather than free Ni^{2+} such as Ni_3S_2 which has been shown to cause cancer and inflammation [48]. Furthermore, one of the factors adding to the dangers of nickel within the body is that nickel is remarkably mobile in biological systems. Studies have shown that increased concentrations (116 - 1200 mg/L) of nickel could be found in tissues adjacent to stainless steel implants as well as in distant organs [49]. It is believed that nickel is able to spread so far due to it using existing biological pathways used to transport Mg^{2+}, allowing it to reach different areas of the body and bind to different cytoplasmic ligands [50, 51]. Because of these issues with nickel, several types of nickel-free stainless steel exist, but these materials suffer from inferior corrosion resistance [52].

Based on these factors, the 304SUS stainless steel should ideally not be in contact with the surrounding body fluid. Therefore, it is of great interest to protect implants utilizing stainless steel from the surrounding body-fluid by coating it with bioactive materials. Ferroelectrics are of special interest for such applications as they could ideally lead to the full encapsulation of the implant in calcium phosphate, effectively removing it from the body-fluid entirely and integrating it with surrounding bone.

2.4.3 Ti6Al4V alloy

Titanium alloys were initially used for aerospace engineering applications but is currently the most frequently used load-bearing biomaterial for orthopedic applications [53, 54]. This is due to the Ti6Al4V alloy's high stability in vivo due to its resistance to corrosion and high biocompatibility as titanium is considered non-toxic even at high doses [55–57]. As with stainless steel, Ti6Al4V has a significantly higher compression strength and elastic modulus compared to bone (Table. 2.4), making it suitable for load-bearing applications. However, Ti6Al4V greatest strength i.e. its inert nature can also cause significant issues when used as a bone replacement material as it does not bond with the surrounding tissue. Ti6Al4V is generally used for long-term implants which preferably should stay implanted for the remainder of a patient's life, however Ti6Al4V have a lifetime of roughly 20 years [58]. Implant failure is largely caused by loosening which reportedly stems from the degradation of surrounding bone by the release of particles or by stress shielding. The release of particles occurs when repeated stress cycling of the implant causes movement in the surface passivation layer of the implant which over time causes cracking to occur [59]. These cracks release particles which can induce osteolysis in surrounding bone [13] until the implant does not have enough contact with the bone and detaches. Similarly, stress-shielding occurs over the long implantation time due to the large mismatch in elastic modulus between Ti6Al4V and bone (Table. 2.4). Ti6Al4V therefore absorbs a significant amount of the stress applied to the implant, preventing its transfer into the surrounding bone effectively minimizing the amount of stress it is exposed to i.e. shielding it. As mentioned in section 2.3, this can lead to the loss of bone-density by disrupting the proliferation of new osteoblasts and eventually cause loosening of the implant [60].

In light of these issues, coating Ti6Al4V surfaces with bioactive materials could yield positive results as Chen et al. [61] found that applied hydroxyapatite coatings promoted the attachment of collagen fibers. In addition, previous work showed that bioactive glass-ceramic implant connected to collagen fibers dramatically improved the bonding between the implant and bone to the degree that under critical stress, cracking would occur in surrounding healthy bone, and not at the interface between the bone and the implant [62, 63]. As such, Ti6Al4V is a prime candidate for the application of bioactive ferroelectric coatings in order to prevent implant loosening.

Table 2.4: Bulk properties of Ti6Al4V-alloy compared to bone.

Material	σ_c [MPa]	E [GPa]
Ti6Al4V	848-1080 [64]	110 [65]
Compact bone	100-230 [12]	7-30 [12]
Cancellous bone	2-12 [12]	0.005-0.5 [12]

2.5 Processing

2.5.1 Sintering theory

Sintering involves the fusing of particles into larger single structures by the loss of porosity and the transfer of mass under the effects of temperature and pressure without melting. The process is dependent on two main factors: a mechanism for material transport, and a source of energy to sustain this mechanism. The primary mass transport mechanism is diffusion and viscous flow with heat being the primary energy source, in conjunction with surface energy at particle-particle interfaces [37].

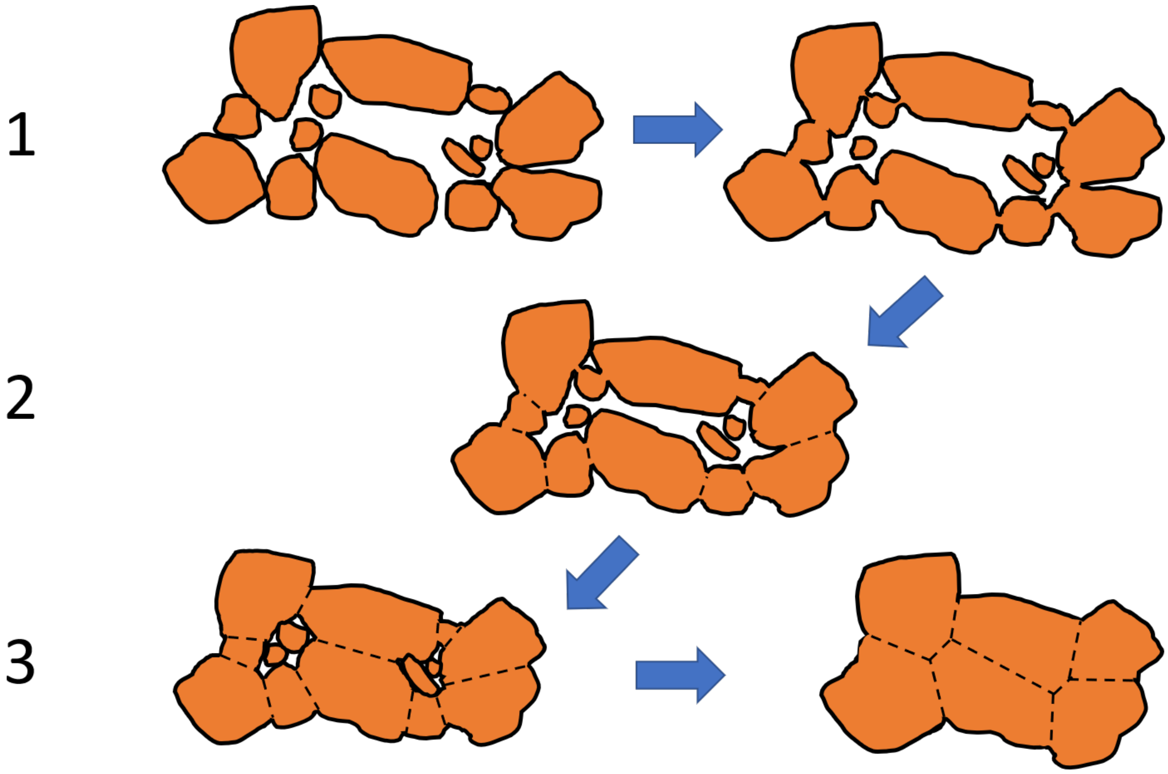

Figure 2.8: The three stages of sintering.

Sintering is often categorized as having three main stages, each with their own characteristic processes [37]. The first stage (Fig. 2.5.1.1) starts with a rearrangement of the particles in space combined with the formation of "necks" at particle-particle contact points. These necks are bonds between particles at the adjacent areas where the surface energy of each particle is the greatest, these necks allow for mass transport between particles. The second stage (Fig. 2.5.1.2) involves the growth of the necks between the different particles, a reduction of porosity and the center of the original particles moving closer together. Some particles start growing at the expense of others by absorbing their mass and form grains, this stage accounts for most of the overall shrinkage in the system. Lastly, the third stage (Fig. 2.5.1.3) involves the final removal of porosity by the diffusion of vacancies along the gran boundaries (dashed lines) and grain growth which is driven by surface energy.

2.5.2 Aerosol deposition

The fabrication of ceramics and ceramic coatings from particles often require high temperatures as mentioned in section 2.5.1. However this can often lead to issues when trying to fabricate ceramic composites and coatings as high temperatures could lead to undesired chemical reactions or uncontrolled grain growth. As such, there is a strong interest in developing room-temperature processing methods. Aerosol deposition is one such method and involves the rapid deposition of particles at high velocities onto almost any substrate [4].

The method was first developed in the late 1990s by Akedo et al. [66–68] and has garnered significant interest for industrial applications. So far, aerosol deposition has been used to produce various thick coatings for use in areas such as microelectronics, biomedical implants, wear- and corrosion resistance, solid oxide fuel cells, humidity sensors and gas sensors [69]. The attractiveness of AD for industrial applications mainly stems from its high cost-effectiveness, the speed at which it can deposit thick (> 1 µm) coatings, low temperature conditions and its ability to integrate different material systems [70–79].

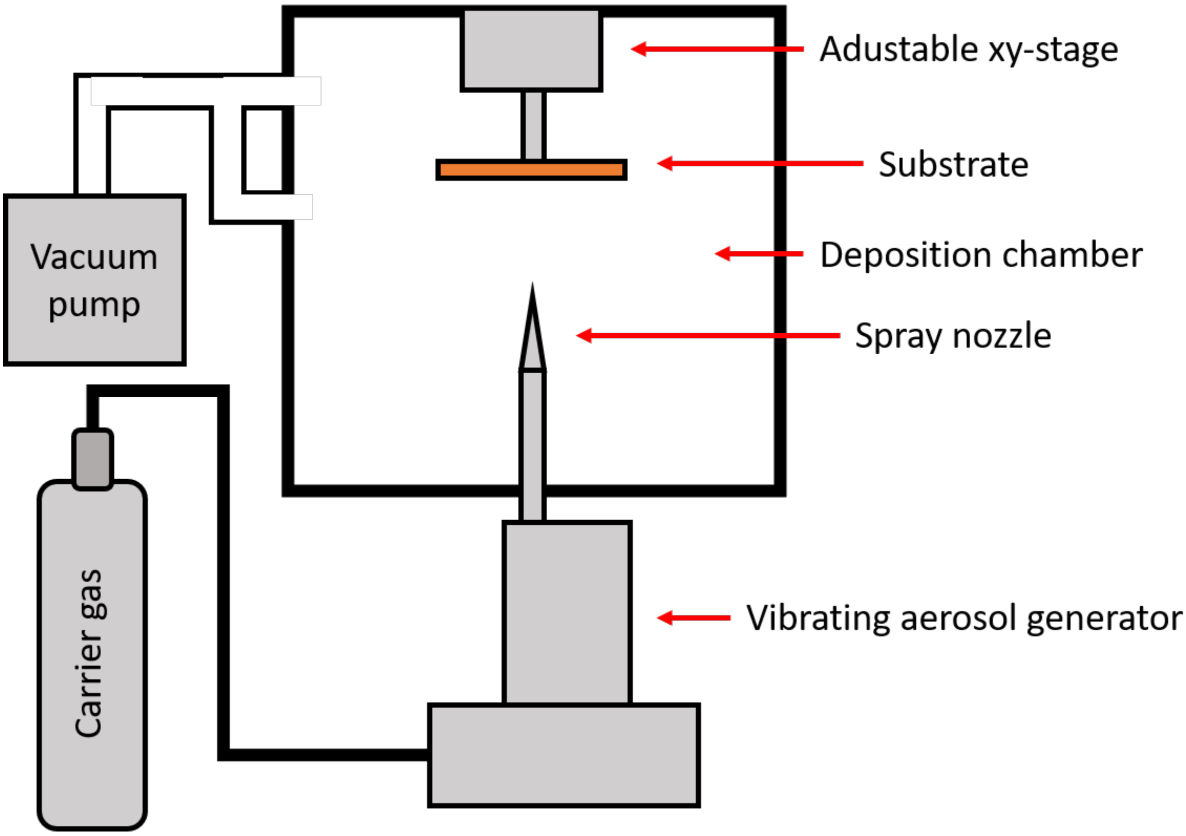

Figure 2.9: Simplified representation of an aerosol deposition set-up.

An aerosol deposition setup is made up of four main components which are shown in Fig. 2.9, these include a vibrating aerosol generation unit, a specialized nozzle connected to the aerosol generator, a deposition chamber with an adjustable substrate holder, and a vacuum pump [4]. The aerosol deposition process starts by placing the desired powders within the vibrating aerosol generator after which carrier gas is passed through it, creating a fluidized bed. This prevents the formation of agglomerates which have a negative impact on the quality of the final coating [80, 81]. Once the aerosol is generated, the pressure difference generated by the vacuum pump and the carrier gas pressure accelerated the aerosolized particles through the spray nozzle onto the substrate in the deposition chamber. The nozzle helps accelerate the aerosol by utilizing a converging-diverging (de Laval) geometry which can achieve velocities ranging from 100 to 600 m/s [4]. The ejected particles then impact with the substrate, causing the powders to fracture into nano-sized fragments which form a ceramic film [68]. Table. 2.5 shows typical aerosol deposition processing parameters, however the speed of deposition is mainly determined by scanning speed and the rate of consumption for the carrier gas. This is due to the carrier gas determining the pressure difference between the aerosol generating unit and the deposition chamber and subsequently the kinetic energy and momentum of the ejected particles [68].

Table 2.5: Typical processing parameters for aerosol deposition as reported by Hanft et al. [4].

Parameter	Value
Deposition chamber pressure	0.2 - 20 mbar
Aerosol generating unit pressure	60 - 1066 mbar
Nozzle geometry	Slit nozzle 2.5 x 0.2 to 25 x 0.8 mm^2
Carrier gas	Air, N_2, O_2, Ar, He
Gas flow rate	1 L/min - 30 L/min
Scan speed	0.05 - 10 mm/s
Distance between nozzle and substrate	0.5 - 50 mm

When depositing ceramics using aerosol deposition the resulting coatings generally have a similar appearance when measured using scanning electron microscopy (SEM) [4]. Characteristic features include non-distinct nano-sized grains, lack of porosity, intimate contact at coating-substrate interface, and the presence of micro-sized craters and elevated ridges on the coating surface. This last meso-feature results from the repeated impact of larger particles which displaces the already deposited coating [82]. In addition, a cross sectional view of aerosol deposited films will generally reveal horizontal additive layers forming a lamellar structure, with each layer roughly corresponding to a scan cycle [83–85].

3 Materials and Methods

3.1 Materials

3.1.1 Aerosol deposition

Commercial ceramic powders were processed and subsequently aerosol deposited onto different substrates by the Functional Ceramics group at the Friedrich-Alexander-Universität Erlangen in Germany. The procedure varied slightly by material system and it outlined below by coating material:

Barium titanate

Barium titanate coatings with thicknesses in the range of 10 µm-12 µm were deposited onto 304SUS stainless steel and Ti6Al4V alloy substrates using aerosol deposition. Commercial barium titanate powders (Helsa-automotive GmbH & Co.KG. Gefrees. Germany) made from conventional solid-state processing using $BaCO_3$ and TiO_2 as starting materials were wet milled in ethanol using a rolling mill to obtain a median particle size of $d_{50} \approx 1.2\,\mu m$. No additives were used. The powders were then vacuum dried at 180 °C for at least 24h.

The aerosol deposition process utilized a special rectangular nozzle with an orifice size of 0.5mm x 10mm and N_2 carrier gas accelerated through at a rate of 4L/min. Distance between the nozzle and substrate was kept fixed at 7mm. The stainless steel substrate was polished to a mirror finish before spraying, while the Ti6Al4V were unpolished and did not receive any additional treatment before spraying.

Barium calcium zirconium titanate

The BCZT powders were made through conventional solid state sintering using $BaCO_3$. $CaCO_3$. ZrO_2 and TiO_2 precursors. The precursors were mixed over a period of 24h in ethanol with the ethanol being subsequently filtered and evaporated off. The mixed powder was then calcined at 1300 °C utilizing a 5 °C heating rate, 3hr holding time and then cooling at an increasing rate of 1 °C-2 °C. Milling followed for 15h in ethanol which was then filtered and evaporated off before running the powders through a 100 µm sieve to obtain the appropriate particle size for aerosol deposition.

Powders were then sprayed onto a Ti6Al4V substrate for a total of 75 scans: 50 with a velocity of 5 mm/sec, followed by 25 scans with a reduced velocity of 2 mm/sec. Working distance between the nozzle and the substrate was reported as being 7.1mm with a N_2 carrier gas flow rate of 4L/min.

3.1.2 Substrates

304SUS stainless steel substrates were procured by the Functional Ceramics Group (Friedrich-Alexander-Universität Erlangen) from INOX-COLOR GmbH & Co KG. The substrates were received in a polyethylene film covered in a carbon based adhesive to protect the supplier's mirror finish (2P/no.7 and 2P/no.8). This adhesive was washed off using an ethanol/acetone mixture right before aerosol deposition commenced. The Ti6Al4V substrates were obtained at the university and were not polished before aerosol deposition.

3.2 Post-processing

3.2.1 Heat-treatment

The heat-treatments were performed using a Kanthal Super box furnace with a maximum temperature range of 1300 °C. Samples were put into a cylindrical Al_2O_3 crucible with a Al_2O_3 disk as a partial cover on top. All samples were heated in air up to temperatures of 400 °C, 550 °C, 650 °C, 750 °C, 1000 °C depending on the individual sample. The heating and cooling rates were 3 °C/min with a holding time of 2h.

3.2.2 Sawing

Due to a relatively small supply of samples, it was decided that they would be cut into four smaller pieces in order complete all the scheduled tests. This was done using a Wells 3500 Series Diamond Wire Saw with a 0.3 mm thick wire as larger saws were too destructive to the sample coatings. The samples were all mounted in place on a ceramic disc using a silicon based-wax with a low melting point such that it could be rinsed off in hot water after cutting.

3.3 Characterization

3.3.1 Composition

Phase Purity and Composition of Ceramic Coatings on Metal Substrates

X-ray diffraction analysis - XRD

The phase purity of as-sprayed BT and BCZT coatings were determined by X-ray diffraction (XRD). Samples were cleaned with ethanol and mounted on deep silica sample holders using molding clay. The instrument used was of the type Bruker D8 A25 DaVinci X-ray Diffractometer using Bragg-Bretano geometry with CuKα radiation of 1.54Å initially utilizing a 60min time-interval from 15-85 °using a variable slit (VS-XRD).

This procedure was later discontinued in favor of a fixed 0.2mm slit (FS-XRD) procedure using a 2h time-interval from 15-85°. This range was later expanded to 3-85°in order to include any potential apatite/calcium phosphate peaks which might develop after the soaking study was concluded, increasing the scanning time to 2.5h. Phase purity and the presence of new chemical species was then assessed using DIFFRAC.EVA software from the Bruker Corporation which matched the diffraction peaks to a PDF database containing diffraction information on a wide range of chemicals. The resulting diffractograms and PDFs formed the basis of subsequent DIFFRAC.TOPAS analysis of crystal structures within the aerosol deposited coatings using the Pawley method of peak-fitting.

Energy Dispersive X-Ray Spectroscopy - EDS

In addition to XRD, elemental composition at the coating-substrate interface was explored using scanning electron microscopy energy dispersive X-ray spectroscopy (EDS). The instrument used was a Zeiss Supra 55VP FESEM (Carl Zeiss AG. Oberkochen. Germany) and Quantax EDS system (Bruker. USA). EDS analysis was subsequently performed using TEAM^{TM} EDS Analysis System software using the characteristic energies of the elements found in the coating and substrates (Table 3.1) to conduct map scans. The maps were collected over 32 frames using a 120µm aperture with high current, an accelerating voltage of 10kV and a dwell time of 200s.

Table 3.1: Characteristic energies of different coating and substrate elements

Element	keV	Series
O	0.525	K
Al	1.486	K
Ca	3.692	K
Ti	4.512	K
V	4.953	K
Cr	5.415	K
Fe	6.405	K
Ni	7.480	K
Zr	2.044	L
Ba	4.466	L

In order to properly conduct EDS analysis on the coating/substrate interface, the samples' interface region needed to be polished flat. To do this, samples were initially cold mounted in epoxy (EpoFix Hardener and Resin. Struers) overnight, with subsequent grinding and polishing being performed using a LaboPol-21 (Struers Inc.. Cleveland. USA) and Tegramin-20 (Struers Inc. Cleveland. USA) respectively.

The grinding steps utilized silicon carbide (SiC) foil (Fig. 3.2) and colloidal diamond particles (Fig. 3.2) for polishing. Samples were cleaned in an ultrasonic bath for 5min between grinding steps, with a final cleaning step of 15min in order to remove remaining debris and particles. However, it turned out that the contraction of the epoxy as it hardened destroyed the sample coatings by delamination. The procedure was therefore abandoned.

An alternative procedure was subsequently developed using the same steps except this time they were performed by mounting samples on glass slides using silicone wax and holding onto these as the samples were ground on the LaboPol-21. After this, the last three polishing steps were done by hand as outlined in Table 3.2. The OP-S colloidal silica suspension mixed with H_2O_2 was used to remove any debries left over from previous grinding/polishing steps before samples were removed from the glass slides using warm water and cleaned in an ultrasonic bath for 5min in ethanol.

Table 3.2: Grinding/polishing procedure used to prepare samples for EDS

Grinding surface	Particle size (µm)	Lubricant/Suspension	Instrument
SiC foil #320	46	Water	LaboPol-21/By hand
SiC foil #1200	15	Water	LaboPol-21/By hand
SiC foil #4000	5	Water	LaboPol-21/By hand
MD Nap	3	Diamond particle suspension	By hand
MD Nap	1	Diamond particle suspension	By hand
MD Chem	0.25	OP-S + H_2O_2 (vol. ratio 4:1)	By hand

Secondary Ion Mass Spectrometry - SIMS

Two barium titanate on stainless steel (BTSS) samples which had been heat-treated at 750 °C, two as-sprayed BTSS samples and lastly a clean substrate were sent to Dr. Anja Henss at the Justus-Liebig University Department of Physical Chemistry in Gießen, Germany. She performed ToF-SIMS measurements on the samples, analysed the data and aided in their interpretation. Samples had to be made flat in order for them to be analysed. The four BTSS samples therefore had their interface region grinded and polished as outlined in Table 3.2, while the substrate had its entire surface treated in the same manner to achieve a mirror-like polish. In addition, half of the coating surface of the BTSS samples were sanded down by passing a piece of 4000 grit silicon carbide sandpaper over the coating in one light stroke. This was sufficient to remove a substantial amount of the coating.

ToF-SIMS measurements were conducted using a M6 instrument (IONTOF GmbH), which is equipped with a 30 kV Bi cluster primary-ion gun for analysis and a 20 kV gas cluster ion beam (GCIB), as well as a dual-source column with O_2^+ and Cs^+ low-energy guns for depth profiling. Depth profiles were measured in spectrometry mode (bunched). The spectrometry mode provides high signal intensity and high mass resolution 40,000 cts/s, FWHM $m/\Delta m$ = 8000 at m/z = 47.94 (Ti^+)). Surface measurements were recorded in spectrometry mode (100 μm^2 × 100 μm^2) keeping the ion dose density below 1012 cm^{-1} depth profiles in spectrometry mode were acquired with O_2^+ ions (2 keV, 150 μm^2 × 150 μm^2) as sputter species and Bi^+ (1.2 pA, 75 μm^2 × 75 μm^2) as primary ions. All measurements were carried out in positive. Data evaluation was carried out with the software SurfaceLab 7.2 (IONTOF GmbH).

3.3.2 Microstructure

Scanning electron microscopy (SEM)

Microsturcture was evaluated using a a Zeiss Supra 55 and Ultra 55 SEM. Parameters for all surface images were kept at 5kV using a 30µm aperture at low current with a working distance of 10mm. All samples were carbon coated prior to SEM imaging to avoid charging and drift (208 carbon High Vacuum Carbon Coated. Cressington Scientific Instruments Ltd.. Watford. UK). To remain consistent, all samples were subjected to 5 cycles of sputtering with each cycle lasting for 8s using a voltage of 4.8V in a 10^{-4}bar vacuum. This resulted in a ∼ 10-20nm layer of carbon depending on the state of the carbon tips used.

Focused ion beam (FIB)

Focused Ion Beam (FIB) microscopy (FEI Helios NanoLab DualBeam) was used to investigate the coating-substrate interface of a single BTSS sample. The $BaTiO_3$ coating was sanded down from 11 µm to ∼ 1 µm using 4000 grit silicon carbide foil to reduce the time needed to make a FIB cross-section. The sample was then placed in the FIB instrument and covered with a platinum protective coating through which a cleaning cross-section was made by sputtering Ga-ions. An accompanying electron beam was then used to image the coating-substrate interface at a 52°angle. Table 3.3 shows the instrument parameters used for each step. The measurement was performed by fellow master student Sondre Bjørø.

Table 3.3: FIB process parameters.

Process	Beam type	Current	Accelerating voltage
Pt-deposition	Ion	0.28nA	30kV
Cleaning cross-section	Ion	6.5nA	30kV
Imaging	Electron	86pA	5kV

3.3.3 Piezoelectric and dielectric properties

Strain, polarization and piezoelectric coefficient measurements were carried out using a TF Analyser 2000 (aixACCT (aixPES). Aachen, Germany). Before being tested, every sample was cleaned in an ultrasonic bath for 5min using ethanol as a solvent. Silver electrodes (Auromal®50L Silberleitlack. Ami Doduco GmbH) were painted onto the samples using a fine haired brush and left to dry for 5min before being tested. Insulating silicone oil (Wacker®AP 100 Silicone Fluid) was used in the test-chamber to prevent dielectric breakdown of air. The parameters used are included in Table. 3.4 and 3.5.

Table 3.4: Polarization and strain parameters

Parameter	Value
Frequency	100Hz
Waveform	Triangle
Amplitude	100kV/cm - 500kV/cm

Table 3.5: Piezoelectric coefficient parameters

Parameter	Value
Mode	100Hz
Amplitude	100kV/cm - 500kV/cm
Small signal frequency	1kHz
Small signal amplitude	3V
No. points	100

Additional piezoelectric coefficient d_{33} measurements were performed using a Berlincourtmeter (APC Ceramics. Mackeyville, PA) which measures the direct piezoelectric effect using resonance. The Berlincourtmeter consists of two parts, a force head and accompanying control electronics. The force head is situated at the end of a threaded screw vice and is made up of two rounded contact probes connected to a loading actuator and reference sample. The sample is clamped between the force heads by adjusting the screw vice so that a static force is applied, keeping the sample in place and preventing it from rattling during measurements. Once the sample is fastened, the control electronics supply an amplified AC signal which drives a loudspeaker type coil. The coil then applies an oscillating force to the sample through the force heads, inducing a piezoelectric response which can be measured. A simplified diagram for the force heads can be seen in Fig. 3.1. All samples measured in the Berlincourtmeter had silver electrodes (Auromal®50L Silberleitlack. Ami Doduco GmbH) painted on the ceramic coating.

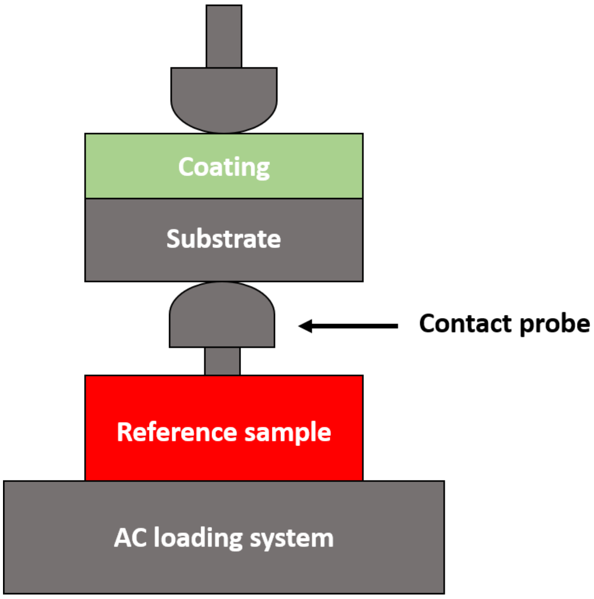

Figure 3.1: Simplified diagram of a Berlincourtmeter.

3.3.4 Mechanical properties

Reduced modulus E_r and hardness H of the coatings were measured by nano-indentation (NI) using a Hysitron TI 950 TriboIndenter. Samples were handed off to Prof. Jianying He at the Norwegian University of Science and Technology Department of Structural Engineering, who performed the measurement. The measurement was made by making a series of 7-9 indentation (sample dependent) across a 60 µm x 60 µm area. The indentation followed a linear load/deload function which can be seen in Fig. 3.2. This load function is used to apply 100nN-10mN of mechanical force with a maximal indenter displacement of 5 µm. The instrument can detect changes in force and displacement down to 0.4nN and 0.01nm respectively.

The resulting force/displacement curves were used to calculate reduced modulus and hardness of each coating using the following equations (4.3-6) found in the Hysitron TI 950 TriboIndenter manual [2]. The reduced modulus is related to the Elastic modulus by equation 3.1 to account for the contribution of the indenter material on the measurement.

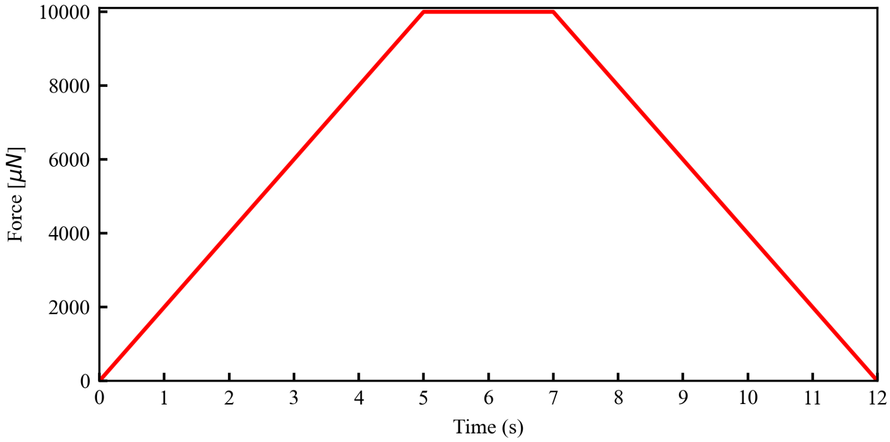

Figure 3.2: Load function used for nano-indentation of aerosol deposited samples.

$$\frac{1}{E_r} = \frac{1-\nu^2}{E_{sample}} + \frac{1-\nu^2}{E_{indenter}} \tag{3.1}$$

The reduced modulus itself is calculated by using equation 3.2. Where S denoted the stiffness of the unloading curve (slope of the initial portion of the unloading curve) and $A(h_c)$ is the the contact area of the indenter with the sample.

$$E_r = \frac{S\sqrt{\pi}}{2\sqrt{A(h_c)}} \tag{3.2}$$

Contact area $A(h_c)$ is itself a variable property as there is not a perfect transfer of force to the contact area from the indenter. The value of the contact area therefore uses the h_c modifier to account for this inefficiency expressed by equation 3.3

$$h_c = h_{max} - 0.75 \times \frac{P_{max}}{S} \tag{3.3}$$

Where h_c is the Contact Depth, h_{max} is the Maximum Depth, P_{max} is the Maximum Force and S is the stiffness. The 0.75 value is usually given in different forms of the equation as epsilon and accounts for edge effects including deflection of the surface at the contact perimeter. Lastly, the hardness is calculated by equation 3.4, and is simply the general definition of hardness, but with the h_c modifier worked into it. Fig. 3.3 visualises how all of these parameters are physically linked.

$$H = \frac{P_{max}}{A(h_c)} \tag{3.4}$$

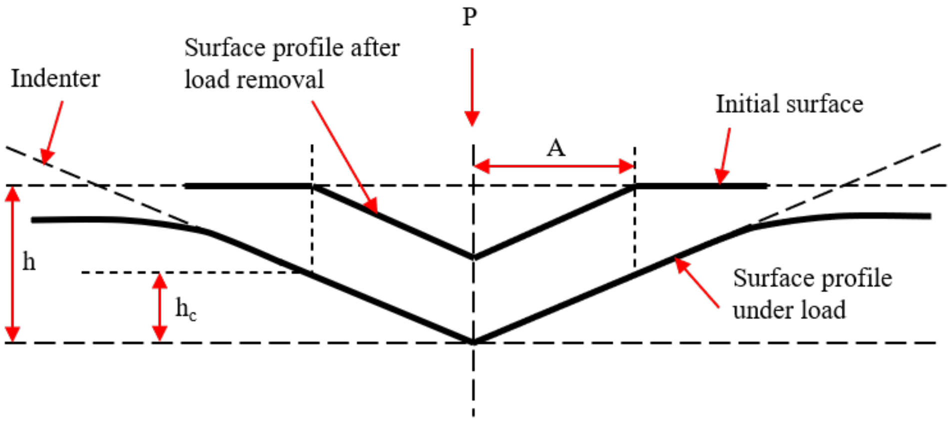

Figure 3.3: Indenter diagram adapted from [2]

3.4 Simulated body fluid (SBF) procedure

3.4.1 Preperation

Simulated body fluid (SBF) for subsequent soaking studies was made in-house following the Kokubo method [28]. A simplified flow-chart of the procedure is outlined in Fig. 3.4. The procedure makes 1000mL of SBF using the equipment shown in Table 3.6

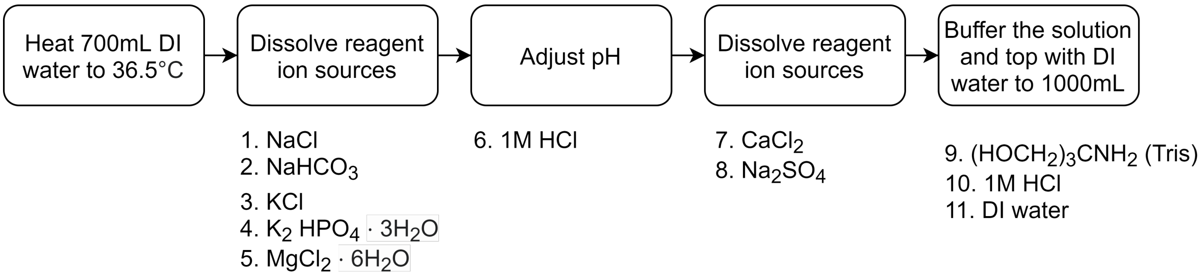

Figure 3.4: Simplified flow-chart of the SBF preparation procedure.

Reagents listed in Table. 3.7 were added in the order noted. Due to the hygroscopic character of many of the reagents, they were all weighed out as quickly as possible to prevent contamination from moisture and stored in a desiccator before and after weighing out the appropriate amounts. Since SBF is a supersaturation with respect to apatite formation, any error in the mentioned steps could lead to precipitation. As such, one has to make sure that the solution is always colorless and transparent with no solids forming on the walls of the beaker. If precipitations does occur, the solution must be discarded. All dry ingredients were weighed out using weighing paper while the 1M HCl solution was made by diluting a 37% 12M stock solution with DI water (4.1667mL HCl measured then topped to 50mL).

Table 3.6: Equipment list for preparation of SBF

Type	Amount
Hot-plate with magnetic top	1
1000mL glass Erlenmeyer flask	1
2500mL Glass beaker	1
Thermometer	1
Magnetic stirrer	2
Clamped stand	1
Volumetric flask (1000mL)	1
Parafilm for storage	As appropriate
Closed 1000mL plastic container for storage	1
pHmeter	1

Table 3.7: Reagent list.

Order	Chemical	Amount required	Actual amount	Purity (%)	Supplier
1	NaCl	8.035g	8.0343g	99.5	Sigma Aldrich
2	$NaHCO_3$	0.355g	0.3553g	99.5	Sigma Aldrich
3	KCl	0.225g	0.2241g	99.5	Sigma Aldrich
4	$K_2HPO_4 \cdot 3H_2O$	0.231g	0.2297g	99.0	Sigma Aldrich
5	$MgCl_2 \cdot 6H_2O$	0.311g	0.3122g	98.0	Sigma Aldrich
6	1M HCl	39mL	39mL	n/a	Sigma Aldrich
7	$CaCl_2$	0.292g	0.2979g	95.0	Sigma Aldrich
8	Na_2SO_4	0.072g	0.0749g	99.0	Sigma Aldrich
9	$(HOCH_2)_3CNH_2$ (Tris)	6.118g	7.1339	99.0	Sigma Aldrich
10	1M HCl	0-5ml	11mL	n/a	Sigma Aldrich

After weighing out all the appropriate reagents (Table. 3.7) the relevant equipment was arranged as pictured in Fig. 3.5. Although glassware should not be used as reaction vessels when making SBF due to their tendency to form apatite on the silicate surface, a glass 1000mL Erlenmeyer flask was used in this instance as there was no plastic beakers available. Ideally, one should use unscratched plastic beakers as the sharp edges of the scratch can serve as high energy nucleation sites.

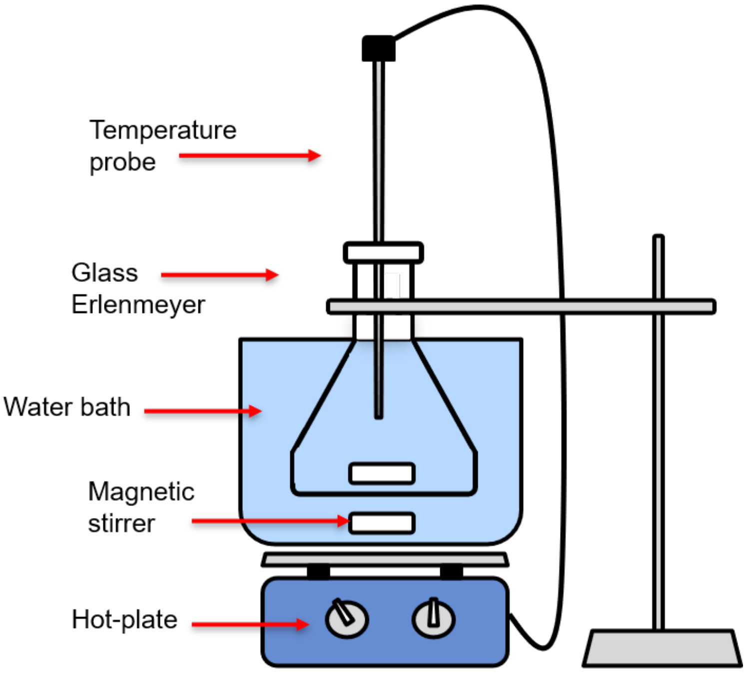

Figure 3.5: Main arrangement of equipment used in preparing the SBF

3.4.2 Dissolving ion sources

A large water-bath was positioned on top of a hot-plate before placing the Erlenmeyer into it. Two stirring bars of different sizes (one large and one small) were added to the water-bath and the Erlenmeyer respectively before filling the water-bath with tap-water until it reached the 900mL mark of the immersed Erlenmeyer. 700mL deionized water (DI) was then added to the Erlenmeyer before turning on the hot-plate to 38 °C and setting the magnetic stirrer to a gentle stir. The Erlenmeyer was then left to reach 36.5 ± 1.5 °C

At 36.5 ± 1.5 °C reagent 1-8 was then slowly added one at the time, taking great care to add only small amounts and letting everything dissolve completely before adding more. This was especially important for the $CaCl_2$ which was packed into large granules, reducing the surface area which the solvent could access.

3.4.3 Creating the buffer system

Once reagent 1-8 had been dissolved, the critical part of the procedure was making the buffer system for the solution so that it would remain stable over time. This part was especially delicate and required additional care compared to step 1-8, especially in monitoring the pH and temperature. As such, the temperature was kept within 36.5 ± 0.5 °C for all the subsequent steps. DI water was then added up to the 900mL mark before inserting the pH meter electrode into the solution after calibration in 4 and 7pH standard solution. The initial pH was 1.43, well within the 2.0 ± 1.0 parameter set by Kukobo et al. [28].

Tris-hydroxyymethyl aminomethane (Tris) was then added little by little while measuring the pH fluctuations after each addition. No more Tris was added before the pH had stabilized/become constant again and the reagent was completely dissolved. This was done step-wise until the pH rose to 7.45 ± 0.01. To reach this point, extra Tris had to be added in addition to the amount described in the literature (see Table. 3.7) When the pH had stabilized at 7.45 ± 0.01, drops of 1.0M HCl was added with a syringe until the pH reached 7.42 ± 0.01. while making sure to not let it fall under 7.40. Once at this value. Tris and HCL was added alternately into the solution until all of the Tris was dissolved and the solution pH was kept within the range of 7.42-7.45. The temperature was then kept at 36.5 ± 0.2 °C while adding HCl dropwise until it reached pH 7.40 at exactly at 36.5 °C (meaning that solution temperature fluctuation was less than 0.1 °C/min).

3.4.4 Washing and cooling

Once the buffer was stabilized, the pH-meter and thermometer were removed from the Erlenmeyer and rinsed with DI water. The washings were collected in a small beaker and poured back into the Erlenmeyer before removing it from the water bath and replacing it with a 1000mL volumetric flask. The volumetric flask was left to reach the same temperature as the surrounding water-bath before proceeding. A separate magnet was used to fix the magnetic stirring bar to the base of the Erlenmeyer, preventing it from falling out. The buffered SBF was transferred from the Erlenmeyer into the volumetric flask. The Erlenmeyer and stirring bar were then rinsed with DI water several times with the washings being added to the volumetric flask.

Lastly, DI water was added to the 1000mL mark of the volumetric flask before withdrawing it from the water-bath and leaving it to cool to room temperature. Once cooled, a little more DI water needed to be added in order to account from the temperature dependent shrinkage of the solution. The solution was then transferred to a clean plastic container which was capped and sealed with parafilm before being put in a 5 °C refrigerator. The solution is stable up to 30 days if refrigerated [28]. The produced solution had the calculated ion concentrations outlined in Table 3.8 based on the weighed amounts.

Table 3.8: Ion concentrations of blood plasma and finished SBF

Ion	Blood plasma concentration (mM)	Finished SBF (mM)
Na^+	142.0	142.8
K^+	5.0	5.0
Mg^{2+}	1.5	1.5
Ca^{2+}	2.5	2.7
Cl^-	103.0	198.9
HCO_3^-	27.0	4.2
HPO_4^-	1.0	1.0
SO_4^-	0.5	0.5
pH	7.2-7.4	7.4

3.5 Soaking study

In order to evaluate the potential functionality of the BTSS material system for hard tissue applications, a soaking study was conducted. The study was meant to determine the effect of poling on the rate of apatite formation on sample surfaces immersed in SBF. Specifically, the goal was to identify whether there was a specific surface charge threshold value which needed to be reached for effective apatite formation to occur.

Aerosol deposited 12 µm BTSS samples were heat-treated in a Kanthal Super box furnace to 750 °C with a heating/cooling rate of 3 °C/min and 2hr holding time. Samples were then cleaned in an ultrasonic bath for 5min in ethanol before being dried in a Termaks Series TS9000 heating cabinet for 10min.

After cleaning, each sample was weighed using a Sartorius Entris™ Toploading Balance before being poled using an in-house corona discharge poling device (CDP). A CDP is a non-contact method that aligns ferroelectric domains by applying a high electric field between a sharp tip electrode with adjustable spacing and a grounded plate which sits on top of a hot-plate (Fig. 3.6). In this process, a secondary effective field arises across the sample as ions are produced around the corona electrode and led onto the sample surface. The temperature of the BTSS samples were kept constant at 25 °C with varying poling times which are outlined in Table. 3.9.

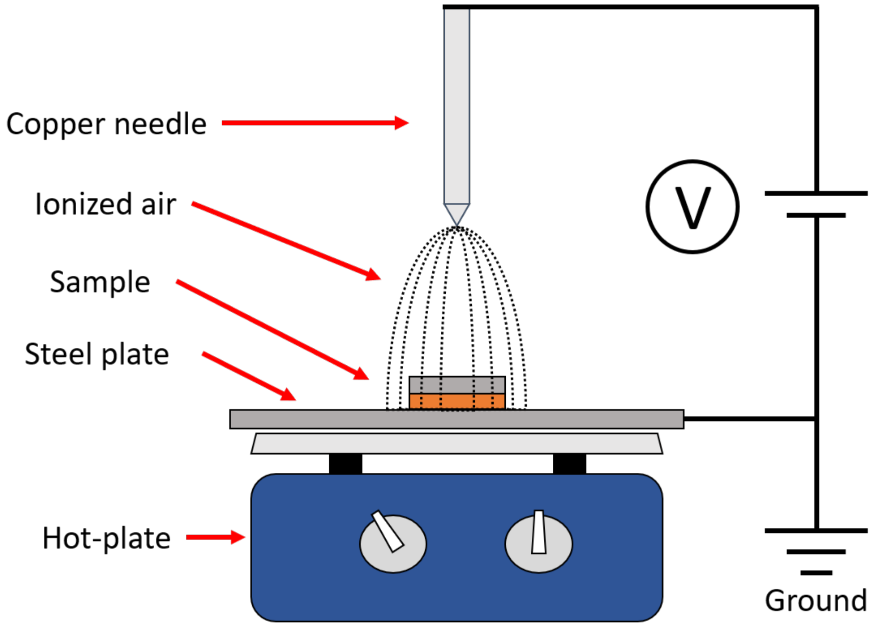

Figure 3.6: Diagram of the in-house corona discharge setup used.

Table 3.9: Poling conditions for BTSS samples 4.1-6.4 meant for SBF soaking.

Sample ID	Poling time	Days of SBF soaking
BTSS 4.1	0	1
BTSS 4.2	10	1
BTSS 4.3	30	1
BTSS 4.4	300	1
BTSS 5.1	0	3
BTSS 5.2	10	3
BTSS 5.3	30	3
BTSS 5.4	300	3
BTSS 6.1	0	7
BTSS 6.2	10	7
BTSS 6.3	30	7
BTSS 6.4	300	7

Once poled, the BTSS samples were put into 100mL plastic bottles before adding 30mL of the prepared SBF to each bottle using a 30mL bulb pipette. The bottles were then sealed and placed a Termaks Series TS9000 incubator, which was set to run continuously at 36.5 °C. Samples removed from the incubator after 1, 3 and 7 days and rinsed with DI water before being left to dry in a desiccator overnight. The dried samples were then weighed again as done previously before undergoing SEM, FS-XRD and EDS analysis as outlined in Section 3.3.2 and 3.3.1.

3.6 Sample overview and nomenclature

The samples used in this work was received from Dr. Neamul Hayet Khasur on behalf of the Functional Ceramics Group at the Friedrich–Alexander University in Erlangen, Germany. The samples initially arrived in the form of coatings deposited on various 1cm x 1cm x 0.5cm square metal substrates. These samples included 9 barium titanate coatings deposited on stainless steel (BTSS), and 3 barium titanate coatings deposited on Ti6Al4V alloy (BTTi). In addition to these, there were also 3 circular 1cm diameter x 0.5cm thick Ti6Al4V substrates coated with calcium/zirconium-doped barium titanate (BCZTTi) which were already in Assoc. Prof Julia Glaum's possession which had been sent from Erlangen at an earlier occasion, but had remained untested. These initial samples were named BTSS 1-9, BTTi 1-3, and BCZTTi 1-3 respectively before being cut into several equally sized pieces as outlined in Section 3.2.2 in order to have more samples to work with. These initial samples were only used for preliminary VS-XRD and SEM before cutting and further testing to establish a reference standard. After cutting, each resulting piece received a new decimal ID based on which of the original integer samples it originated from. These samples and their received treatments/measurements are outlined in Table 3.10. The abbreviations SEM, VS-XRD, FS-XRD, EDS, NI, SIMS and BCM refer to scanning electron microscopy, variable slit x-ray diffraction, fixed slit x-ray diffraction, energy dispersive X-ray spectroscopy, nano-indentation, secondary ion mass spectrometry and Berlincourtmeter measurements respectively.

Table 3.10: Overview of the samples used in this thesis.

Sample ID	**Heat-treatment**	**Measurements**
BTSS 1.1	As-sprayed	None, destroyed in prep
BTSS 1.2	As-sprayed	None, destroyed in prep
BTSS 1.3	400 °C	SEM, VS-XRD, FS-XRD, EDS, NI, Piezo-testing, BCM
BTSS 1.4	550 °C	SEM, VS-XRD, FS-XRD, EDS, NI, Piezo-testing, BCM
BTSS 2.1	650 °C	SEM, VS-XRD, EDS, FIB, Piezo-testing
BTSS 2.2	750 °C	SEM, VS-XRD, EDS, FIB, Piezo-testing
BTSS 2.3	750 °C	SEM, FS-XRD, NI, Piezo-testing

Continued on next page

Table 3.10 – continued from previous page

Sample ID	Heat-treatment	Measurements
BTSS 2.4	1000 °C	None, destroyed by heat-treatment
BTSS 3.1	As-sprayed	FS-XRD, NI, Piezo-testing
BTSS 3.2	650 °C	FS-XRD, NI, Piezo-testing
BTSS 3.3	As-sprayed	Piezo-testing, BCM
BTSS 3.4	650 °C	Piezo-testing
BTSS 4.1	750 °C	SEM, FS-XRD, EDS, Corona poled, Soak
BTSS 4.2	750 °C	SEM, FS-XRD, EDS, Corona poled, Soak
BTSS 4.3	750 °C	SEM, FS-XRD, EDS, Corona poled, Soak
BTSS 4.4	750 °C	SEM, FS-XRD, EDS, Corona poled, Soak
BTSS 5.1	750 °C	SEM, FS-XRD, EDS, Corona poled, Soak
BTSS 5.2	750 °C	SEM, FS-XRD, EDS, Corona poled, Soak
BTSS 5.3	750 °C	SEM, FS-XRD, EDS, Corona poled, Soak
BTSS 5.4	750 °C	SEM, FS-XRD, EDS, Corona poled, Soak
BTSS 6.1	750 °C	SEM, FS-XRD, EDS, Corona poled, Soak
BTSS 6.2	750 °C	SEM, FS-XRD, EDS, Corona poled, Soak
BTSS 6.3	750 °C	SEM, FS-XRD, EDS, Corona poled, Soak
BTSS 6.4	750 °C	SEM, FS-XRD, EDS, Corona poled, Soak
BTSS 7.1	750 °C	SEM, SIMS
BTSS 7.2	750 °C	SEM, SIMS
BTSS 7.3	As-sprayed	SEM, SIMS
BTSS 7.4	As-sprayed	SEM, SIMS
BTSS 8.1	650 °C	Piezo-testing
BTSS 8.2	650 °C	Piezo-testing
BTSS 8.3	750 °C	BCM, Corona poled/depoled
BTSS 8.4	750 °C	BCM, Corona poled/depoled
BTSS 9.1	750 °C	BCM, Corona poled/depoled, Soak
BTSS 9.2	750 °C	BCM, Corona poled/depoled
BTSS 9.3	750 °C	BCM, Corona poled/depoled
BTSS 9.4	750 °C	BCM, Corona poled/depoled
BTTi 1.1	400 °C	SEM, VS-XRD, FS-XRD, NI, Piezo-testing, BCM
BTTi 1.2	550 °C	SEM, VS-XRD, Piezo-testing
BTTi 1.3	650 °C	SEM, VS-XRD, Piezo-testing
BTTi 1.4	750 °C	SEM
BTTi 2.1	As-sprayed	FS-XRD, SEM, EDS, NI

Continued on next page

Table 3.10 – continued from previous page

Sample ID	**Heat-treatment**	**Measurements**
BTTi 2.2	As-sprayed	Piezo-testing
BTTi 2.3	750 °C	FS-XRD
BTTi 2.4	550 °C	FS-XRD, NI, BCM
BTTi 3.1	650 °C	FS-XRD, NI, BCM, Piezo-testing
BTTi 3.2	As-sprayed	None, in reserve
BTTi 3.3	As-sprayed	None, in reserve
BTTi 3.4	As-sprayed	None, in reserve
BCZTTi 1.1	400 °C	SEM, VS-XRD, FS-XRD, EDS, NI, Piezo-testing, BCM
BCZTTi 1.2	550 °C	SEM, VS-XRD, FS-XRD, EDS, NI, Piezo-testing, BCM
BCZTTi 1.3	650 °C	SEM, VS-XRD, FS-XRD, EDS, FIB, NI, Piezo-testing, BCM
BCZTTi 1.4	750 °C	SEM, VS-XRD, FS-XRD, EDS, FIB, NI, Piezo-testing, BCM
BCZTTi 2.1	As-sprayed	SEM, FS-XRD, EDS, NI, Piezo-testing, BCM
BCZTTi 2.2	As-sprayed	Piezo-testing
BCZTTi 2.3	As-sprayed	Piezo-testing
BCZTTi 2.4	As-sprayed	None, in reserve
BCZTTi 3.1	650 °C	Piezo-testing
BCZTTi 3.2	As-sprayed	Piezo-testing
BCZTTi 3.3	As-sprayed	None, in reserve
BCZTTi 3.4	As-sprayed	None, in reserve

4 Results

4.1 Composition

Heat-treatment had a varying impact on the samples with two main categories arising. These were either changes to the main $BaTiO_3$/$Ba_{0.85}Ca_{0.15}Zr_{0.10}Ti_{0.90}O_3$ phases, or the formation of new reaction products. Two BTSS samples (2.1-2) showed substantial chemical change in the form of many new peaks in their respective diffractograms. However, as these results were not reproducible in any other samples, they were treated mainly as outliers. Most samples across all material systems showed few or no new peaks outside of their respectable main coating phases. This section will present the XRD diffractograms of each material system and the calculated crystal parameters.

4.1.1 Phase purity and crystal structure of as received samples

VS-XRD measurements were carried out on the as-sprayed samples received from Erlangen in order to compare them with the commercial powders before spraying. Fig. 4.1 shows substantial peak broadening in the as-sprayed samples compared to the commercial powders.

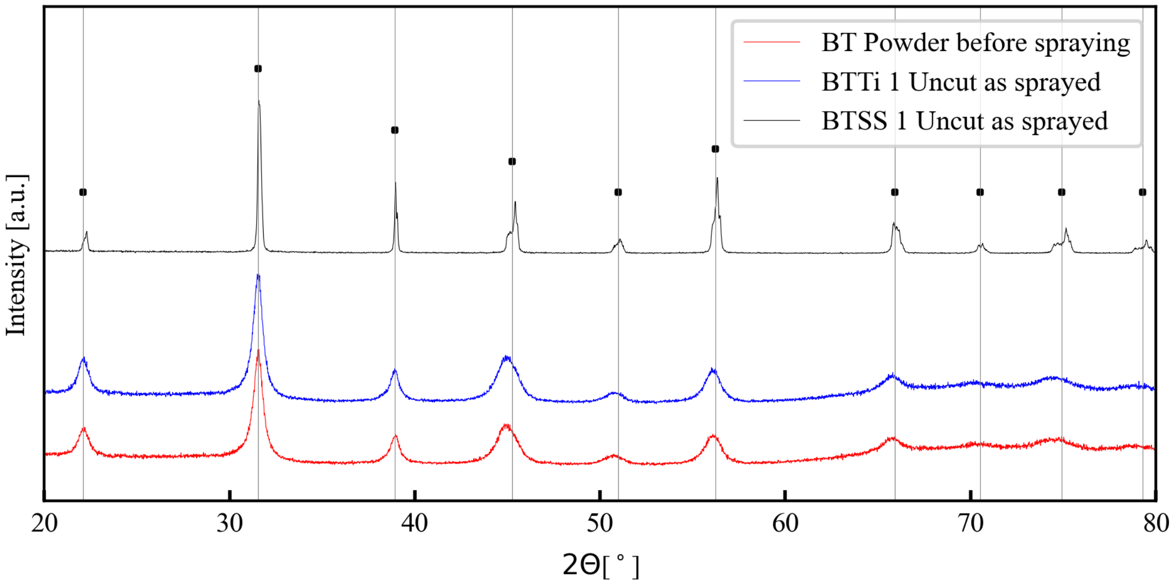

Figure 4.1: VS-XRD diffractogram for the uncut BTSS 1 and BTTi 1 samples with the accompanying powder diffractogram supplied by the collaborator in Erlangen. Tetragonal $BaTiO_3$ (PDF 04-010-4893) is identified as the main phase and marked with (■)

DIFFRAC.EVA software was used to match the peaks with tetragonal $BaTiO_3$ (PDF 04-010-4893) as described in section 3.3.1. DIFFRAC.TOPAS version 5 was used to calculate the crystal parameters from the obtained diffractograms, revealing significant increases in lattice parameters a(Å), c(Å) and consequently the cell volume ($Å^3$) (Table 4.1). Crystalite size was drastically reduced and is reported as LVol-IB which is a volume-weighted mean of the Lorentzian and Gaussian crystallite sizes obtained by calculating the full width at half maximum (FWHM) and integral breadth of the peaks.

Table 4.1: Lattice parameters, crystallite size and cell volume of initial starting $BaTiO_3$ powders and as-sprayed BTTi 1 and BTSS 1 samples.

Sample	a(Å)	c(Å)	LVol-IB (nm)	Cell Volume ($Å^3$)
Powder	3.9951802	4.0242268	47.308	64.23255
BTTi 1	4.0150210	4.0722836	8.861	65.64682
BTSS 1	4.0072418	4.0588458	9.127	65.17689

4.1.2 Crystal structure and chemical products after heat-treatment

The presence of new chemical products after heat-treatment was evaluated using two different X-ray based measurements. The first was FS-XRD in tandem with EVA.BRUKER software to match new diffraction peaks with a PDF-database of potential chemical species. The second method involves EDS imaging at the coating-substrate interface.

FS-XRD diffractograms of the main body of BTSS samples remained largely phase pure with the exception of four minor peaks between 25°-29° and a small contribution at 41.5° (Fig. 4.2. These peaks were collectively matched with PDF 04-008-7985 which corresponded to barium chromate ($BaCrO_4$). These peaks were only visible in samples heat-treated at 750 °C.

Two BTSS samples (2.1-2) stood out from the rest of the BTSS samples in this thesis in that they showed several new non-reproducible peaks. Fig. 4.3 shows sample BTSS 2.2 (750 °C) and the peaks are noticeable sharper than in the other BTSS samples. DIFFRAC.EVA PDF database matching paired the various peaks with tetragonal $BaTiO_3$ (PDF 04-010-4893), graphite (PDF 00-056-0159), barium oxide (PDF 04-022-3039), manganese silicon oxide (PDF 04-012-1729) and nickel chromium oxide phosphate (PDF 04-015-3501). All products contained elements commonly found in the substrate or coating.

The presence of graphite was further investigated by making a cross-section into the BTSS 2.2 sample with a focused ion beam (FIB). Fig. 4.4 shows the cross-section, and one can see what appears to be a dense interlayer of black carbon interdispersed between the $BaTiO_3$ coating and stainless steel substrate. A subsequent partial atom probe tomography (APT) measurement confirmed the presence of carbon at the coating/substrate interface.

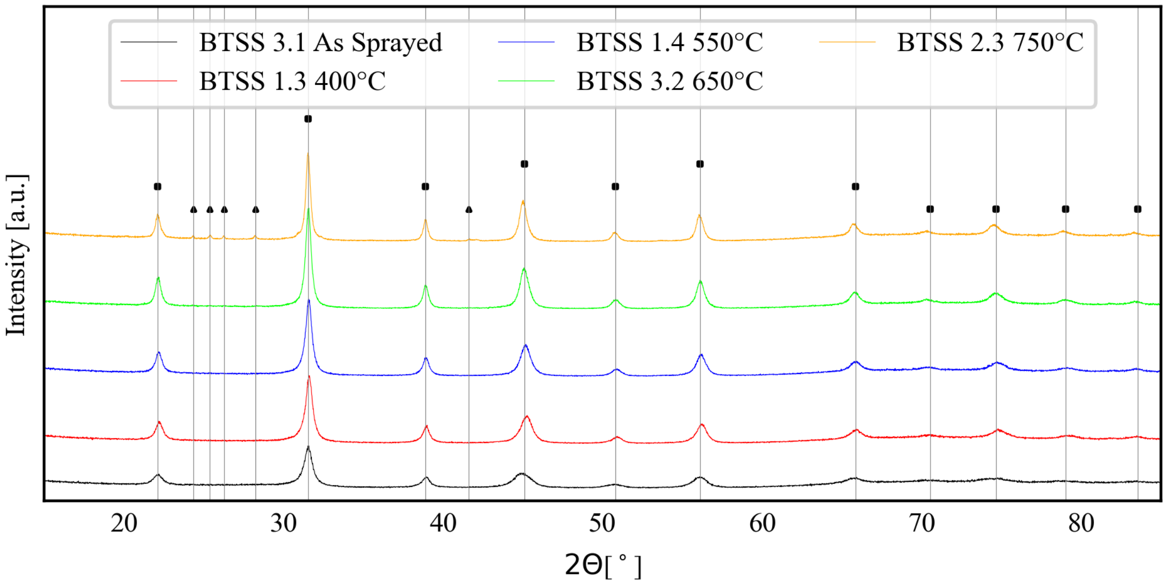

Figure 4.2: FS-XRD diffractogram for BTSS samples. Tetragonal $BaTiO_3$ (PDF 04-010-4893) (■) was present in all temperature programs, with the appearance of $BaCrO_4$ (PDF 04-008-7985) (▲) at 750 °C.

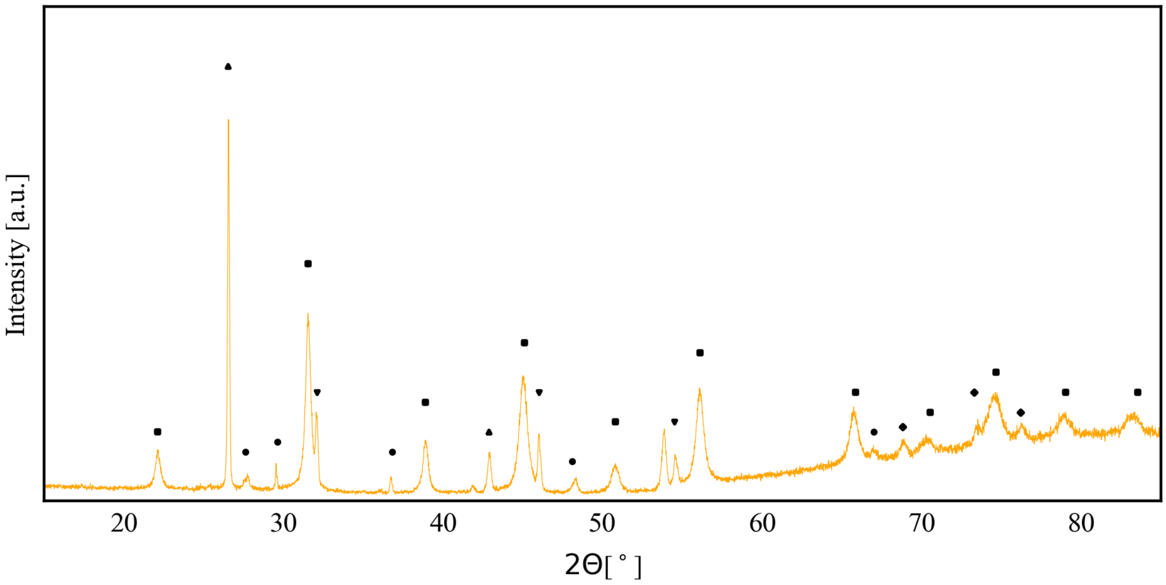

Figure 4.3: VS-XRD diffractogram for BTSS 2.2 (750 °C). The marked peaks correspond to tetragonal barium titanate (PDF 04-010-4893)(■), graphite (PDF 00-056-0159)(▲), barium oxide (PDF 04-022-3039)(▼), manganese silicon oxide (PDF 04-012-1729)(◆) and nickel chromium oxide phosphate (PDF 04-015-3501)(●).

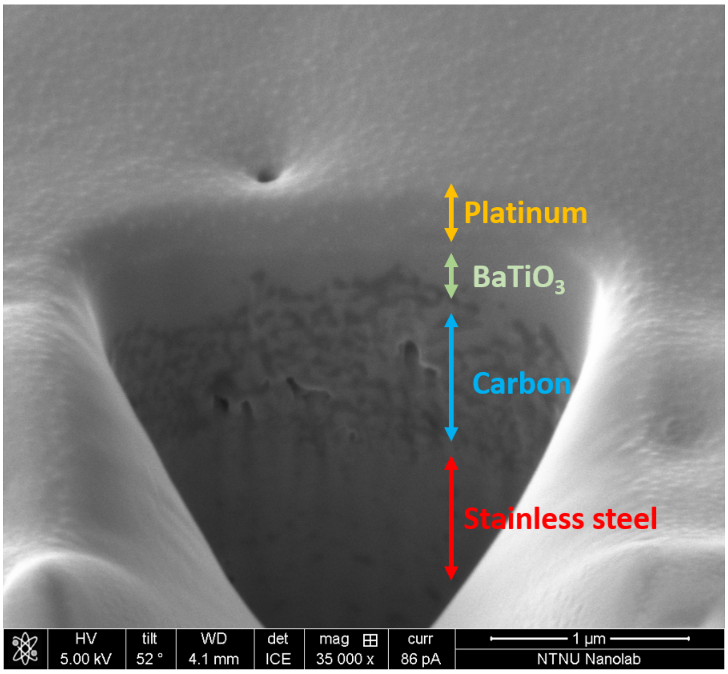

Figure 4.4: FIB-milled wedge on BTSS 2.2 (750 °C)

BTSS 2.1 shared most of its new peaks with BTSS 2.2, but the barium oxide peaks seen in BTSS 2.2 were absent (Fig. 4.5. Instead, the BTSS 2.1 sample showed the barium chromate peaks seen in all other samples heat-treated at 750 °C. The BTSS 2.1 graphite peak was less substantially less intense than the one in BTSS 2.2.

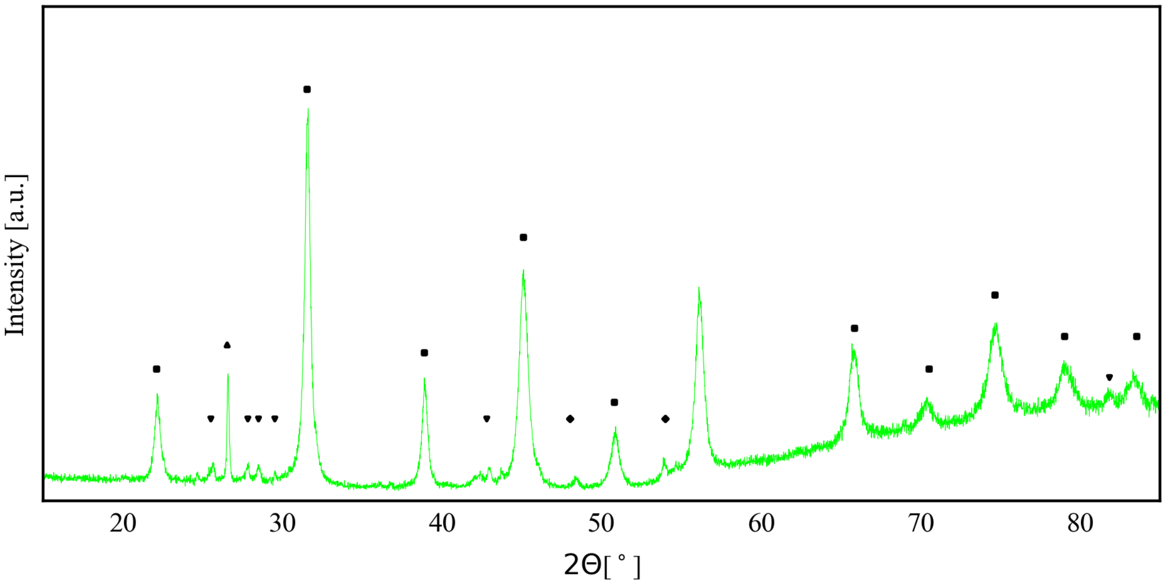

Figure 4.5: VS-XRD diffractogram for BTSS 2.1 (650 °C). The marked peaks correspond to tetragonal barium titanate (PDF 04-010-4893)(■), graphite (PDF 00-056-0159)(▲), barium chromate (PDF 04-007-9581)(▼) and nickel chromium oxide phosphate (PDF 04-015-3501)(◆).

Diffractograms for BTTi samples changed little with increasingly high heat-treatments as seen in Fig. 4.6. The only new visible peaks were associated with rutile TiO_2 (PDF 04-003-0648) in sample BTTi 2.3. Note that the BTTi 2.3 750 °C diffractogram seen in Fig. 4.6 is collected from the remains of the delaminated sample coating, not an intact sample.

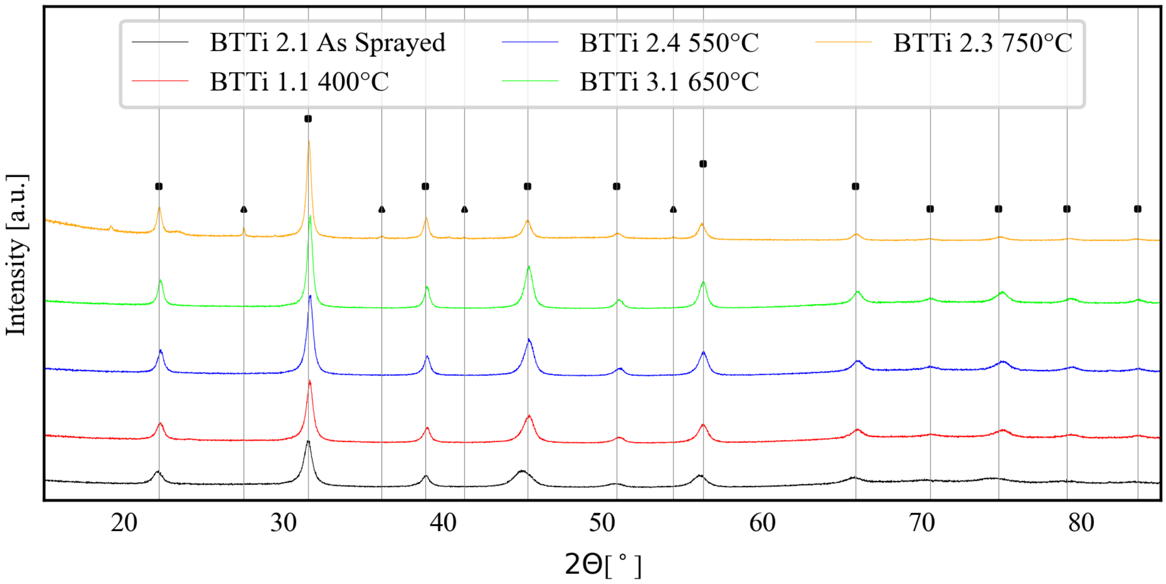

Figure 4.6: FS-XRD diffractogram for BTTi samples showing tetragonal barium titanate (PDF 04-010-4893) (■), Rutile (PDF 04-003-0648) (▲).

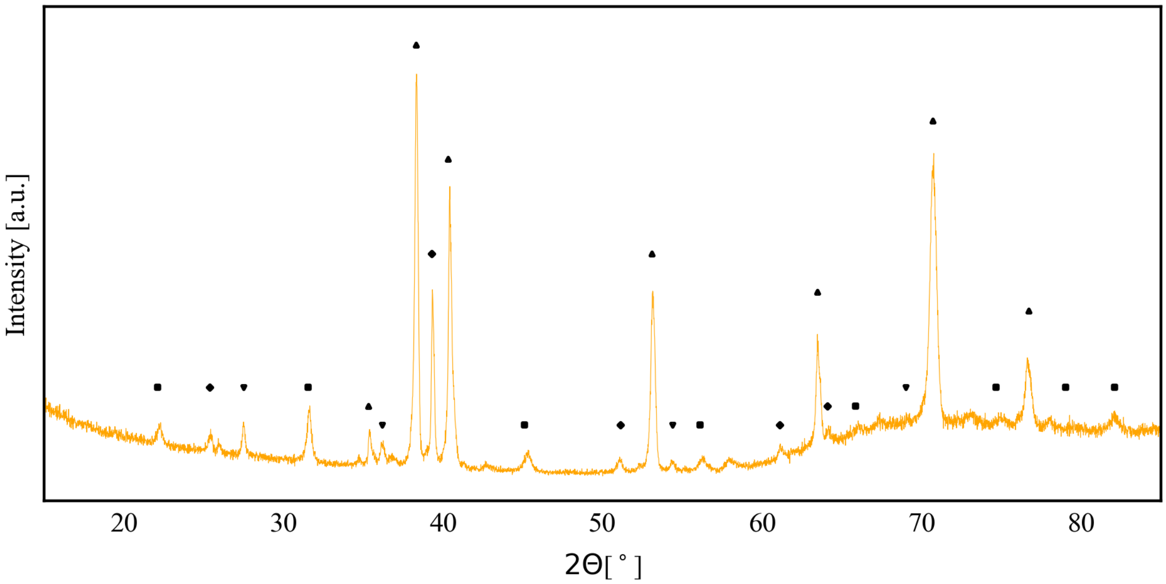

Figure 4.7: FS-XRD diffractogram for BTTi 2.3 substrate. The marked peaks correspond to tetragonal barium titanate (PDF 04-010-4893)(■), $Ti_{0.86}Al_{0.10}V_{0.04}$ (PDF 04-023-7232)(▲), TiO_2 (PDF 04-003-0648)(▼), and Ti_2N (PDF 04-002-0574)(◆).

The remaining BTTi 2.3 substrate was also analyzed after delamination (Fig. 4.7) and small peaks for the remains of $BaTiO_3$ coating was still visible. The substrate main main peaks came from titanium-alloy (PDF 04-023-7232), rutile TiO_2 (PDF 04-003-0648), and Ti_2N (PDF 04-002-0574). Note that the PDF which matched the titanium alloy was highly deficient in aluminum and vanadium compared to the Ti6Al4V, yet PDF 04-023-7232 was the closest substitution which could be found.

The BCZTTi samples showed no new peaks, with only the coating main phase (tetragonal BCZT, PDF 01-086-8334) and substrate (Ti6Al4V, PDF 04-020-7055) peaks being visible after each heat-treatment. Constant contributions from the substrate to the XRD measurements of BCZTTi compared to BTSS and BTTi samples are due to the differences in coating thickness between the samples. BCZTTi samples had coatings which were 4 µm thick while BTSS and BTTi samples had coatings ranging from 10 µm to 12 µm. Since the DaVinci 1 XRD instrument has a penetration depth of roughly 10 µm, it is highly likely that the incident beam has penetrated all the way down to the substrate for the BCZTTi samples.

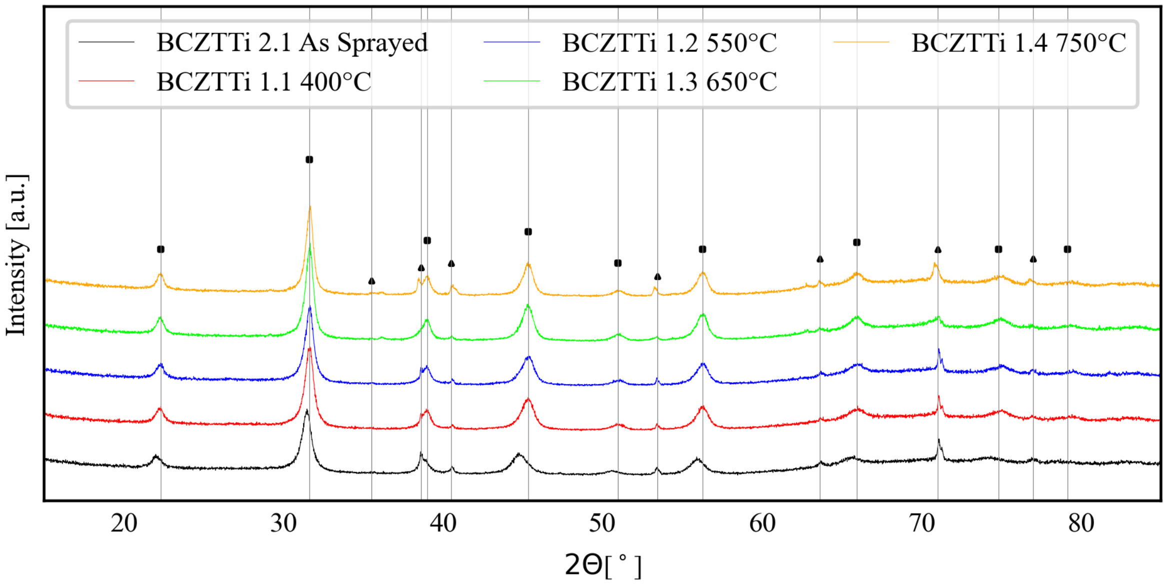

Figure 4.8: FS-XRD diffractogram for BCZTTi samples showing tetragonal BCZT (PDF 01-086-8334)(■), and Ti6Al4V (PDF 04-020-7055) (▲)

EDS mapping was conducted after FS-XRD in order to directly observe potential new chemical phases. However, it was not possible to achieve a complete data-set as the BTTi coatings were too mechanically unstable after heat-treatment to undergo the grinding/polishing procedure needed to take proper SEM images of the interface. Grinding would tear off the coating at the edges of the sample, leaving only the polished substrate and debris on top. BTSS and BCZTTi samples however remained stable enough to image.

Results from EDS mapping at the coating/substrate interface did not align very well with the FS-XRD analysis in that it showed little indication of new chemical side products. Specifically, BTSS samples did not show a clear interlayer or expanded interface region as a result of heating. Rather, there existed a clear separation of the coating and substrate, in both the as-sprayed and 750 °C sample conditions with little apparent diffusion of elements between the two (Fig. 4.9a-d). This is mainly seen in the clear separation of the iron (red) rich substrate and oxygen rich coating (teal).

There was some evidence of chromium depletion at the interface in the form of thin dark strips right below the edge of the main chromium containing region (Fig. 4.9e). Furthermore, there is a small number of chromium signals dispersed through the otherwise dark coating phase, in conjunction with the clear presence of oxygen in the substrate. Note that the EDS elemental overlays are the summed maps of all the elemental contributions, with the strongest signals dominating the map, while specific elemental maps only include signals from one element.

The BCZTTi samples were markedly changed by the heat-treatment. As-sprayed samples show the characteristic close contact and clear separation of the substrate and coating seen previously (Fig. 4.10a-b) but samples treated at 750 °C show signs of aluminum diffusion and considerable cracking. Fig. 4.11 shows a clear overlap between the oxygen rich coating and the aluminum content of the substrate. The oxygenated region of the EDS map corresponds well to ceramic coating, pictured as the more lightly colored material which extends down to the lower cracks in the SEM image (Fig. 4.11a). Conversely, the aluminum content can be seen as migrating "bands" extending well into the oxygen map (Fig. 4.11c-d). The red dotted line shows the coating/substrate interface.

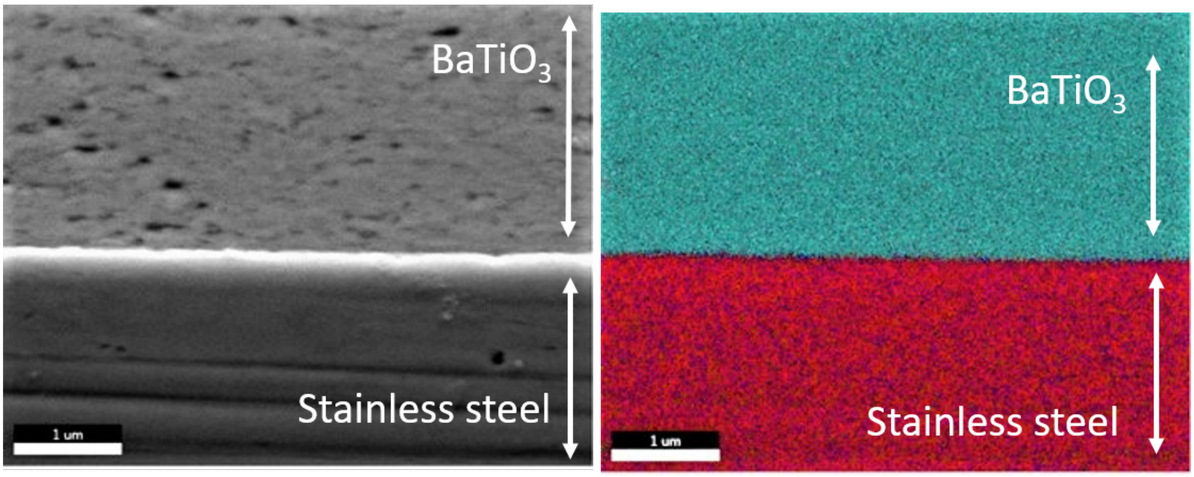

(a) SEM BTSS 3.1

(b) EDS Elemental overlay BTSS 3.1

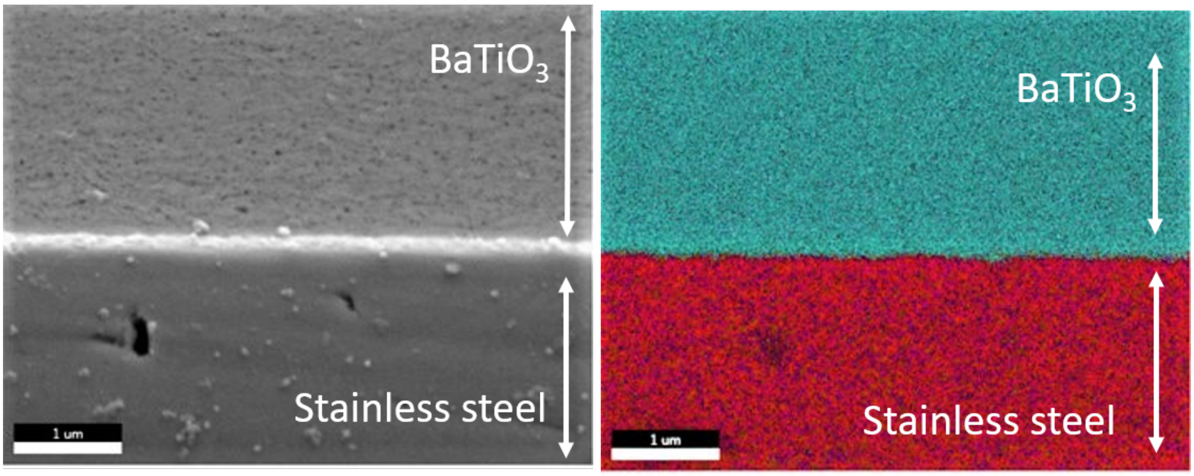

(c) SEM BTSS 2.3

(d) EDS Elemental overlay BTSS 2.3

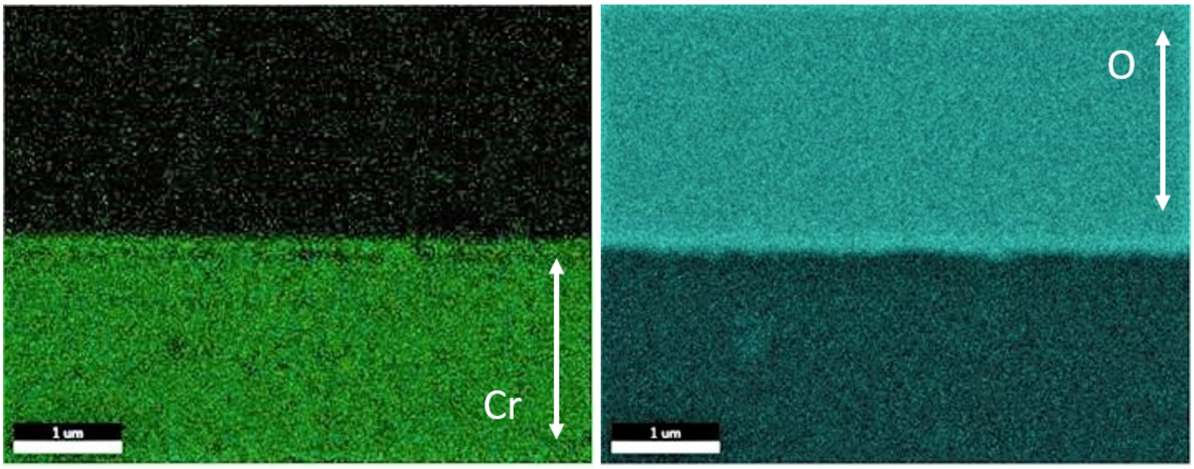

(e) Chromium map BTSS 2.3

(f) Oxygen map BTSS 2.3

Figure 4.9: EDS elemental maps of BTSS 3.1 (as-sprayed) and BTSS 2.3 (750 °C). The elemental overlays are the summations of all the different signals.

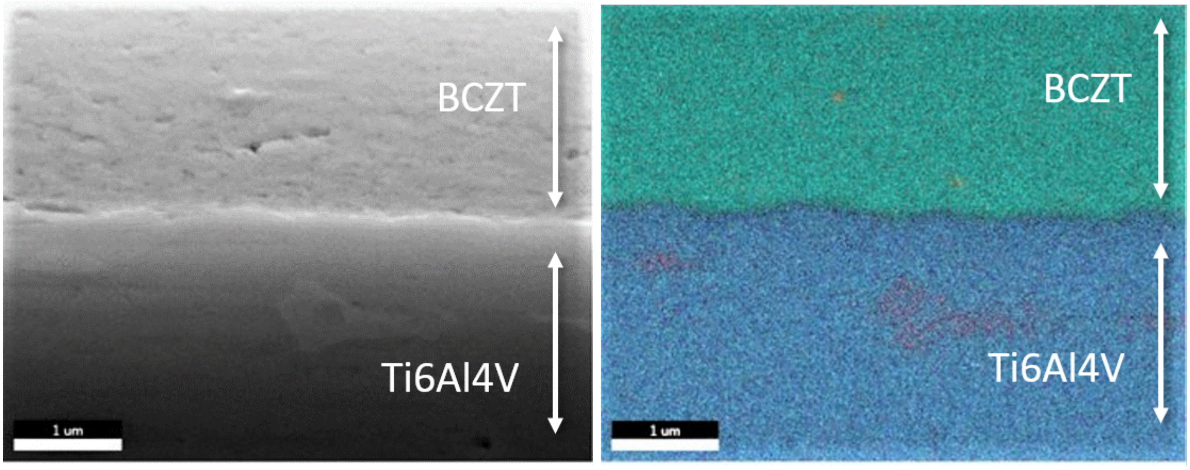

(a) SEM BCZTTi 2.1 (b) EDS Elemental overlay BCZTTi 2.1

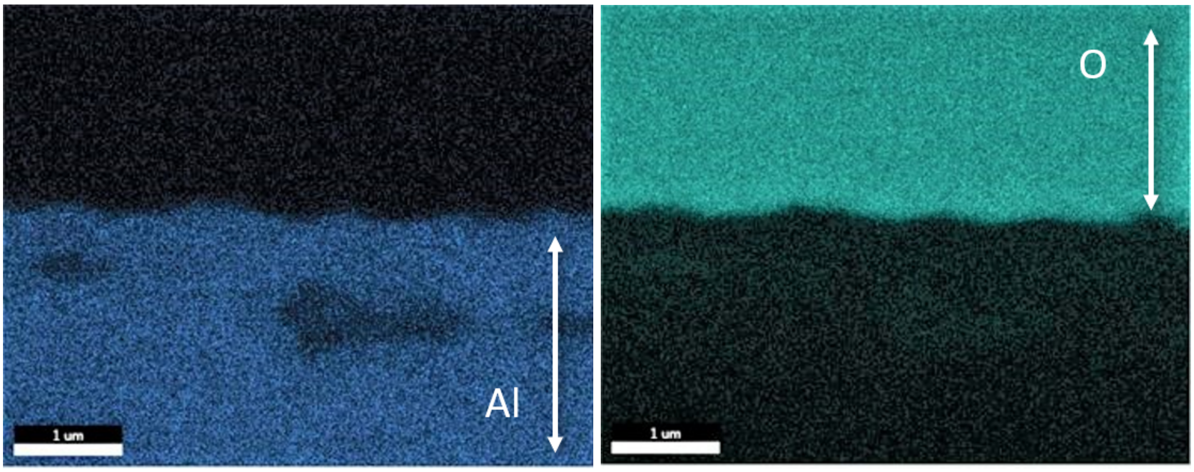

(c) Aluminium map BCZTTi 2.1 (d) Oxygen map BCZTTi 2.1

Figure 4.10: EDS elemental maps of BCZTTi 2.1 (as-sprayed), the elemental overlays are the summations of all the different signals.

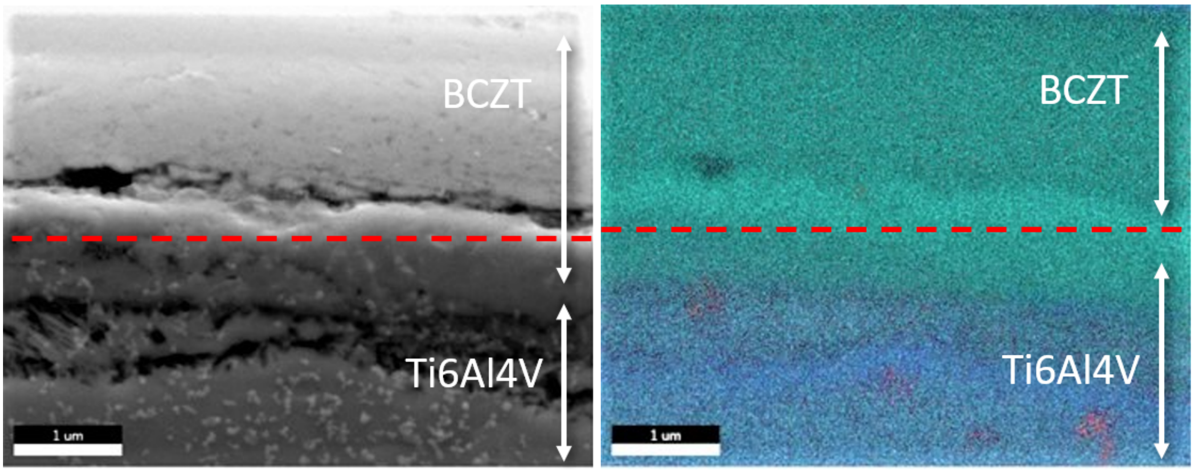

(a) SEM BCZTTi 1.4

(b) EDS Elemental overlay BCZTTi 1.4

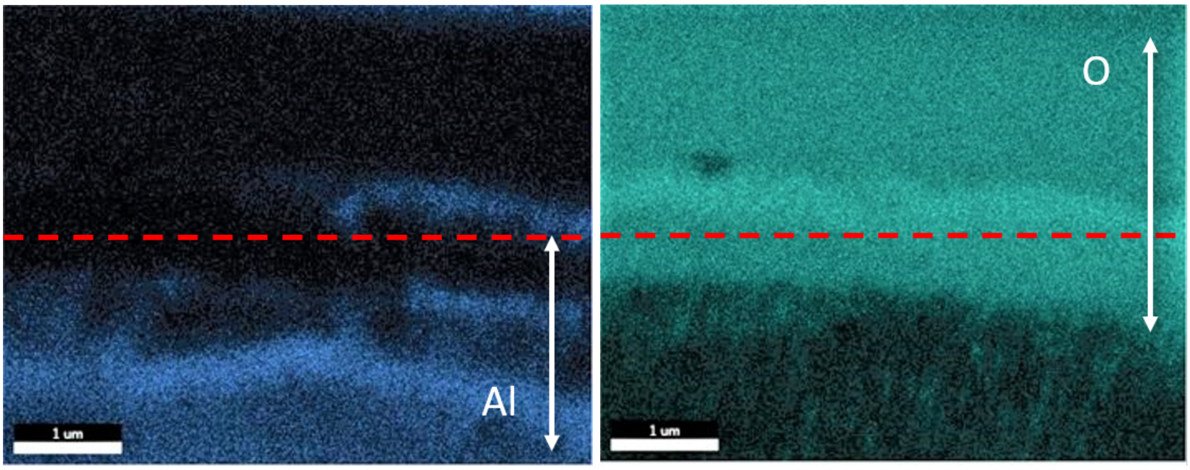

(c) Aluminium map BCZTTi 1.4

(d) Oxygen map BCZTTi 1.4

Figure 4.11: EDS elemental maps of BCZTTi 1.4 (750 °C), the elemental overlays are the summations of all the different signals. The red dotted line shows the coating/substrate interface.

Tof-SIMS measurements on two BTSS samples (one as-sprayed and one heat-treated at 750 °C are presented below. Fig. 4.12 shows the depth profile the as-sprayed sample. The Fig. is divided into three parts, the region left of the first dashed red line is the $BaTiO_3$ coating, the region between the two dashed lines is an interlayer/interface region and the region right of the last dashed line is the substrate. In the coating region, the intensity of barium and titanium dominate over trace amounts of iron, chromium, manganese and nickel. The barium/titanium signals have several matching dips in the signal intensity throughout the coating, until the interface is reached where a sharp decrease in barium and titanium is observed, coupled with a sharp increase in the stainless steel alloying elements. The ratios of the various elemental signals to each other stays largely constant in the different regions, showing slightly non-stoichiometric $BaTiO_3$ (more titanium and barium) and a stainless steel composition roughly matching the one seen in Table. 2.2 by the intensities' order of magnitude.

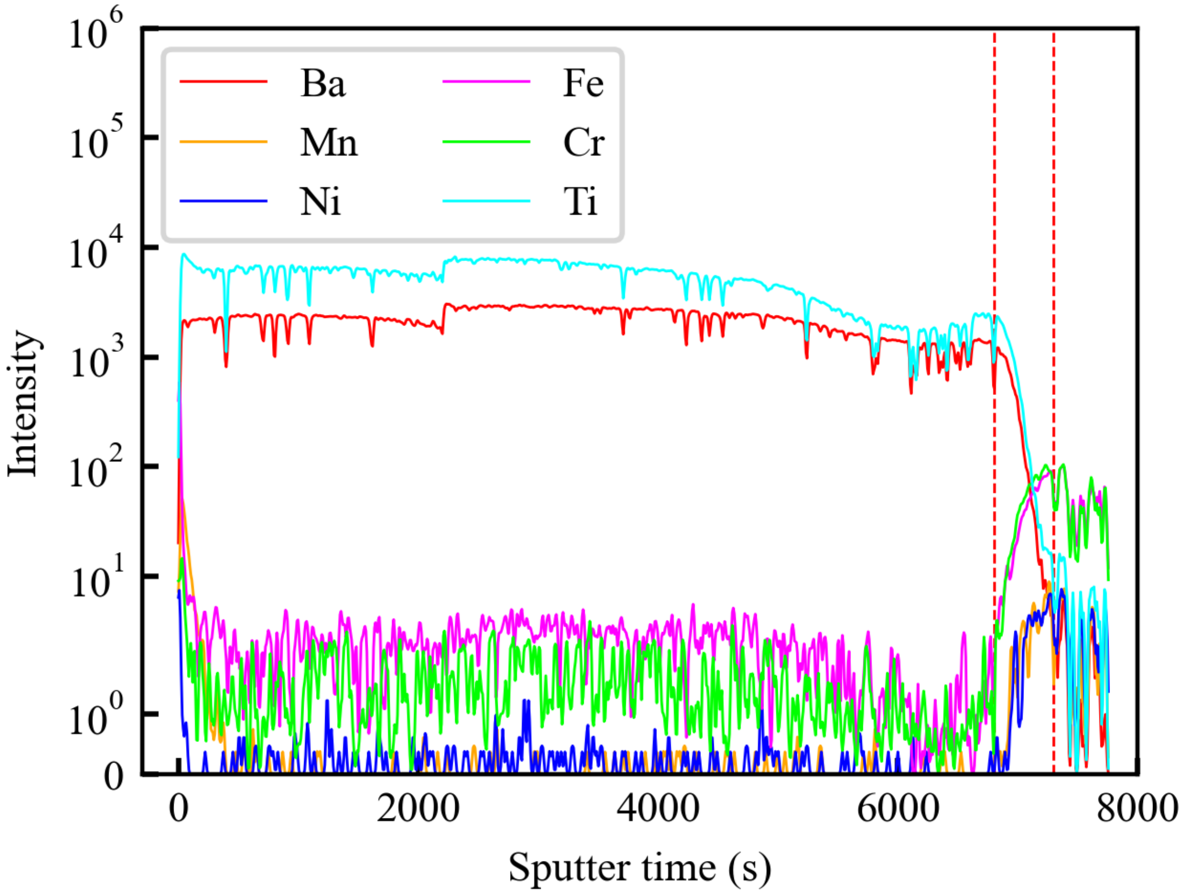

Figure 4.12: ToF-SIMS depth profile carried out on an as-sprayed BTSS sample.

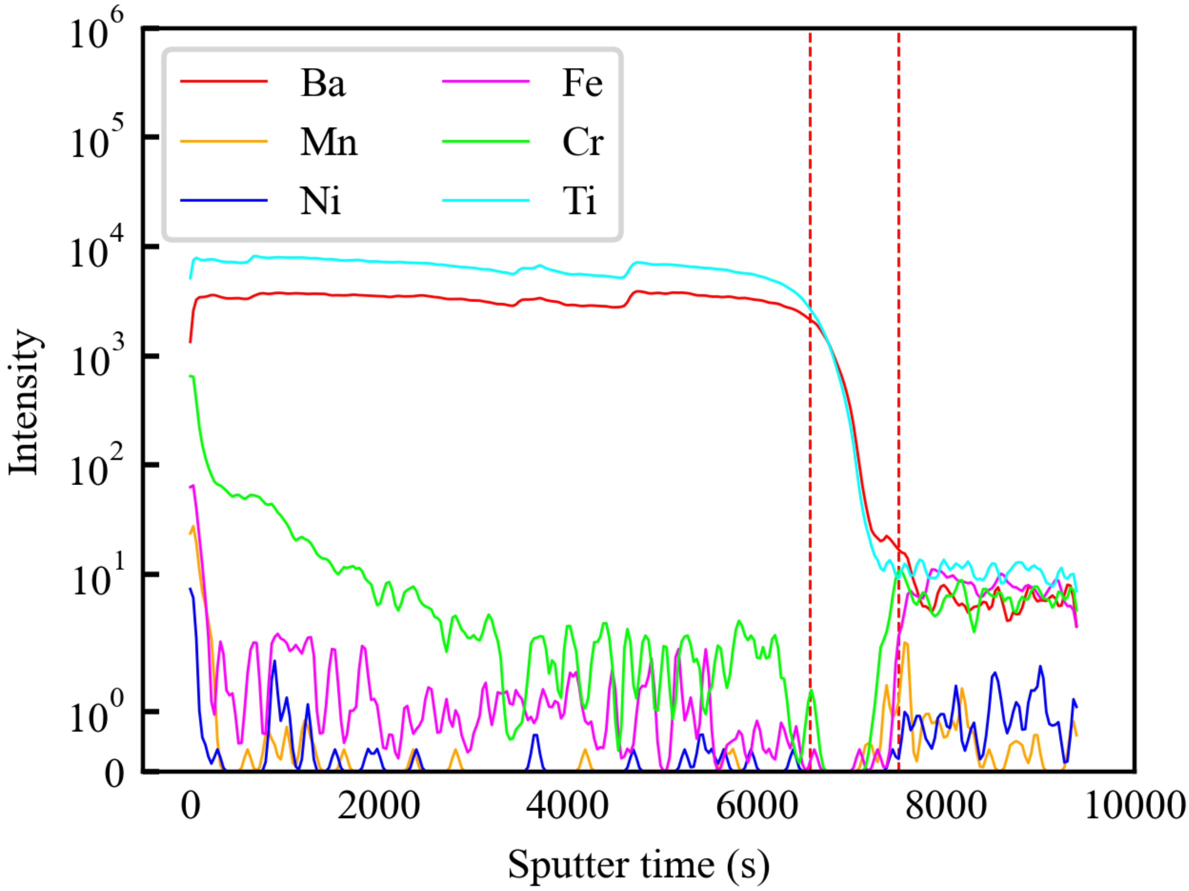

Figure 4.13: ToF-SIMS depth profile carried out on an 750 °C BTSS sample.

Heat-treatment at 750 °C had a clear effect on the depth profile. Fig. 4.13 follows the same convention as Fig. 4.12 in terms of assigning regions to the coating, interface and substrate, marked by the two vertical dashed lines. The substrate region appears largely similar to the as-sprayed sample, but the signal is not as variable. The interface region shows a clear drop in all the alloy elements (iron, chromium, nickel, manganese) down to a value of zero, before increasing again once one crosses into the coating region. The barium and titanium signals in the 750 °C are similar to the as-sprayed sample in their magnitudes and relation to eachother. However, the frequent dips in the intensity are no longer present after heat-treatment. The chromium signal shows a gradual increase in intensity towards the coating surface, with a surface value close to that of barium and titanium. This trend was also shown in SIMS surface measurements which show a relatively high intensity of chromium at the surface (Fig. 4.14). The other alloying elements retain low intensity signals throughout most of the coating.

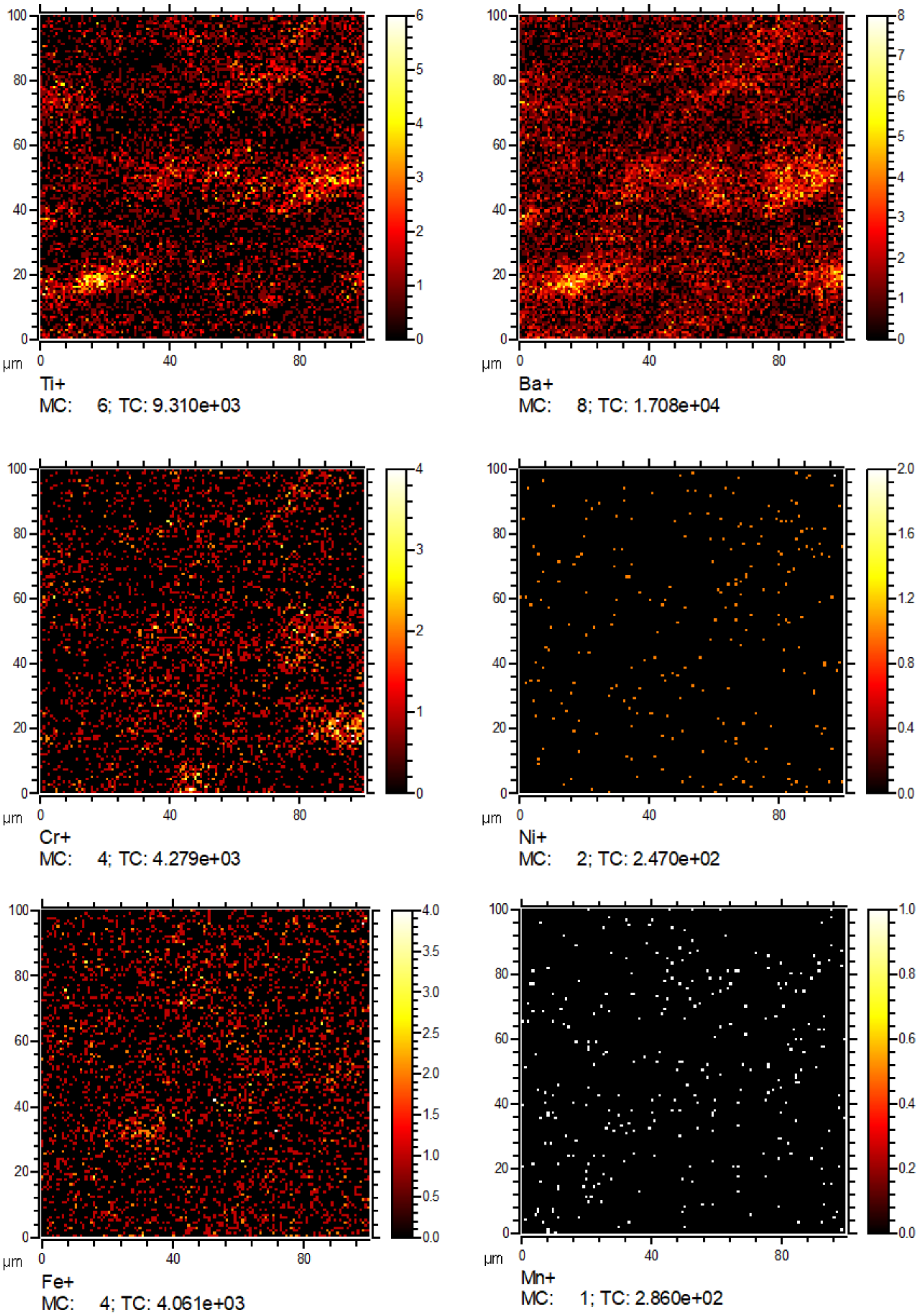

Figure 4.14: ToF-SIMS surface measurement carried out on an 750 °C BTSS sample.

4.1.3 Changes to crystal structure of coating main phase

Changes to the major phases of the coatings were calculated from the FS-XRD measurements in Figures 4.2, 4.6 and 4.8 using DIFFRAC.TOPAS version 5. The numbers reported include lattice parameters, crystallite sizes (LVol-IB) and unit cell volumes. The specific values of these measurements can be found in the Appendix (Table 7.1, 7.2, 7.3).

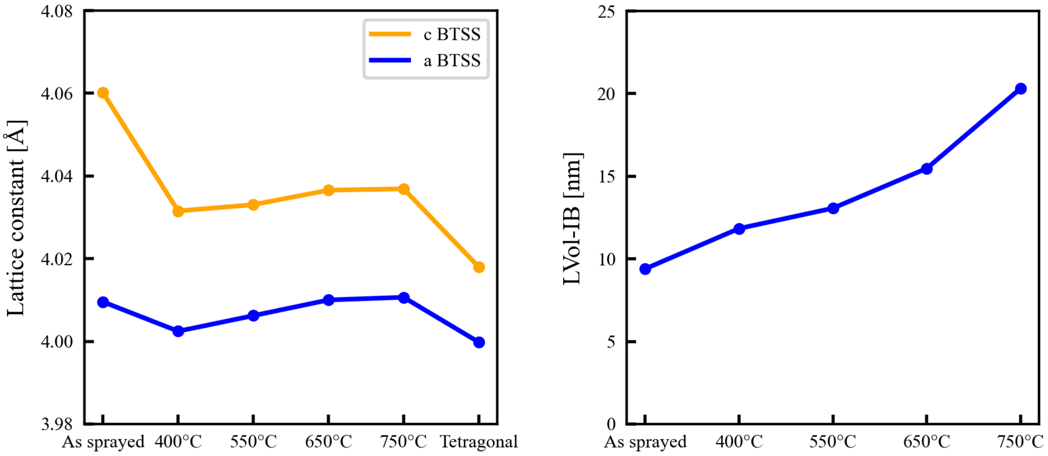

(a) Lattice parameters BTSS

(b) Crystallite size BTSS

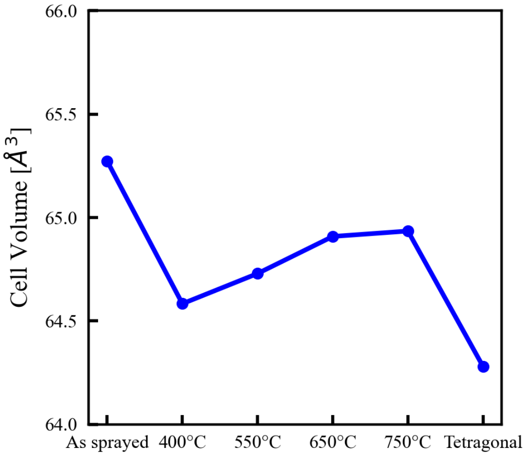

(c) Cell Volume BTSS

Figure 4.15: Structural changes in the BTSS major phase as a function of increasing heat-treatment temperature. Lattice parameters and cell volumes are compared to tetragonal $BaTiO_3$ (PDF 04-010-4893)

The BTSS samples show a large initial reduction in the length of lattice constants a and c before experiencing a gradual increase again (Fig. 4.15a). This coincides with the changes seen in the cell volume of the barium titanate major phase as the volume is a product of the a and c lattice constants (Fig. 4.15c). Both the a and c lattice constants behave in the same manner after a slightly different initial decrease. Furthermore, the a and c values increasingly diverge in the positive direction from the tetragonal reference values listed in PDF 04-010-4893 as temperature increases. Crystallite size continually increased with increasing heat-treatment temperature (Fig. 4.15b).

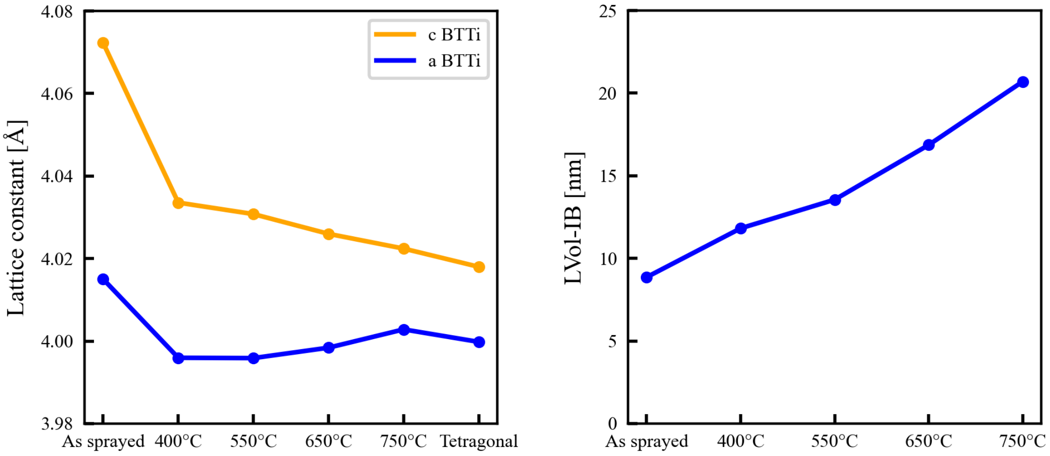

(a) Lattice parameters BTTi

(b) Crystallite size BTTi

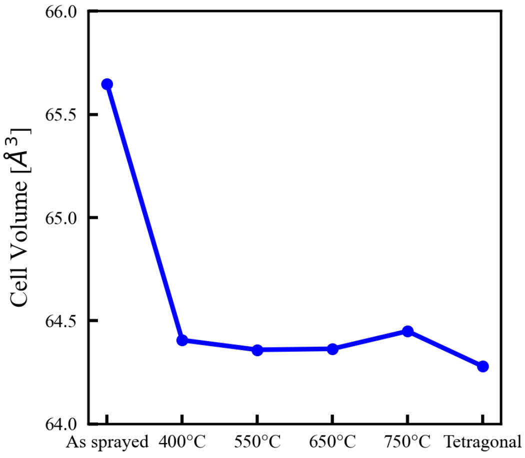

(c) Cell Volume BTTi

Figure 4.16: Structural changes in the BTTi major phase as a function of increasing heat-treatment temperature. Lattice parameters and cell volumes are compared to tetragonal $BaTiO_3$ (PDF 04-010-4893)

The BTTi coatings' crystal structures behave in a similar manner to the BTSS ones when exposed to elevated temperatures. Changes in crystallite size follows the same trend between the two material systems with similar values (Fig. 4.16b). Despite this, after a large initial decrease in lattice constants a and c, continued heating shows the lattice constants converging linearly towards the reference values with the exception of a slight divergence in lattice constant a at 750 °C (Fig. 4.16a). It is important to note, that the 750 °C condition does not measure an intact sample, but rather the delaminated coating of a BTTi sample which fell off after heating. This coating was collected, crushed into a powder, suspended in ethanol and spread onto a flat silicon surface before collecting the FS-XRD diffractogram.

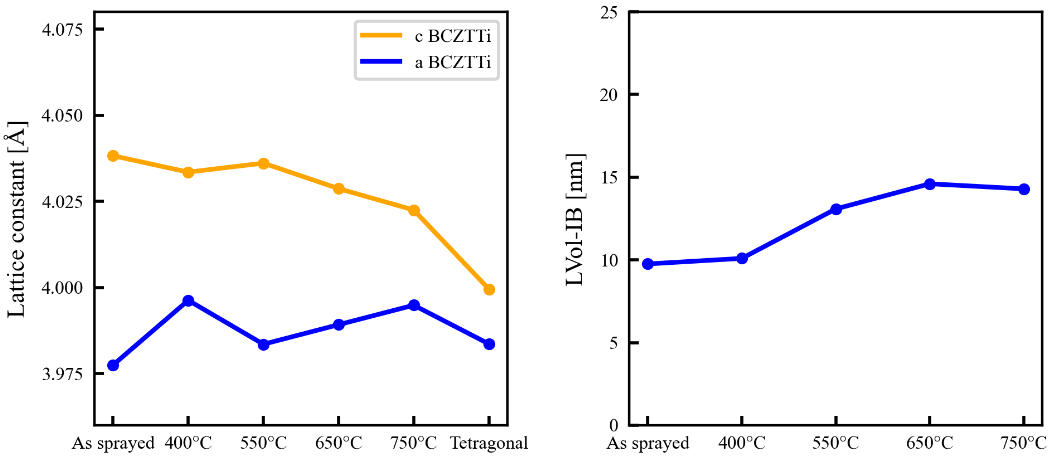

(a) Lattice parameters BCZTTi

(b) Crystallite size BCZTTi

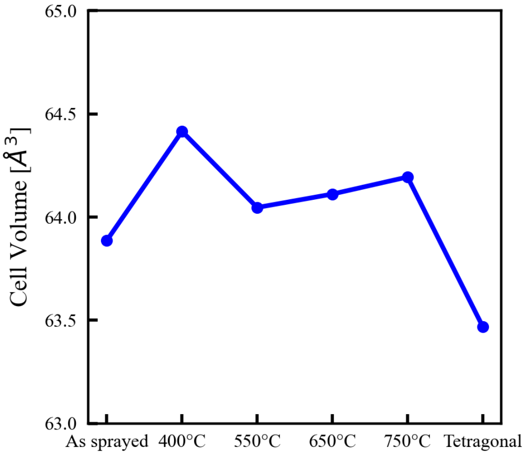

(c) Cell Volume BCZTTi

Figure 4.17: Structural changes in the BCZTTi major phase as a function of increasing heat-treatment temperature. Lattice parameters and cell volumes are compared to tetragonal BCZT (PDF 01-086-8334)

Lastly, the BCZTTi material system shows a mixture of trends. The crystallite size in the tetragonal BCZT phase does increase as a function of temperature (Fig. 4.17b) as in the other two material systems, but remains largely constant for heat-treatments over 650 °C. The BCZT coating does not experience the large initial shrinkage in cell volume observed in BTSS and BTTi, rather it sees a sharp increase in cell volume (Fig. 4.17c). After this initial difference, the BCZTTi system behaves similarly to the BTTi system in that the lattice constants converge (Fig. 4.17a).

4.2 Microstructural changes from heat-treatment

Microstructure is one of the key parameters governing the electrical behavior of piezoelectric ceramics. Therefore, microstructural changes brought on by the various heat-treatments was of special interest. The morphology of the coatings were assessed through SEM imaging and is presented sequentially by material system in the following order: BTSS, BTTi , BCZTTi.

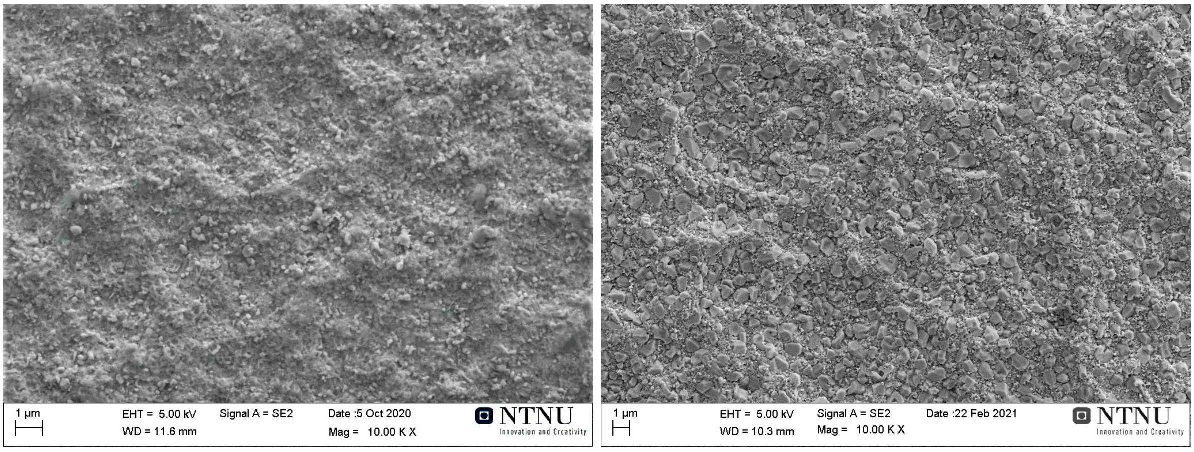

(a) BTSS 3.1 as-sprayed

(b) BTSS 2.3 750 °C

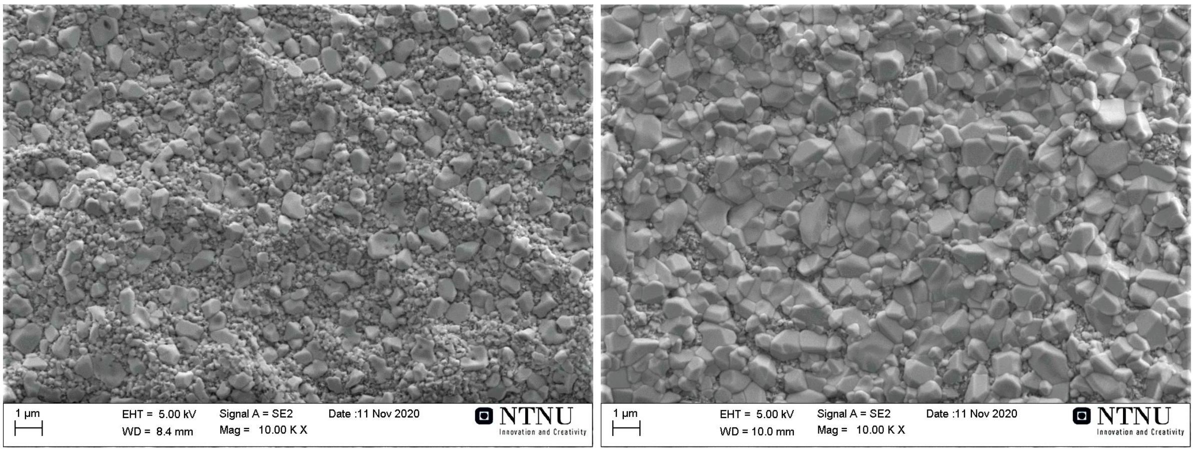

(c) BTSS 2.1 650 °C

(d) BTSS 2.2 750 °C

Figure 4.18: Microstructural comparison of BTSS samples, including the two outlier samples.

Microstructure did not vary significantly in most temperature conditions, with the only clear change occurring in samples treated at 750 °C (with the exception of BTSS 2.1-2 samples). In the BTSS samples there is a definitive initiation of grain growth on the surface, as seen in BTSS sample 2.3 (Fig. 4.18b). The sample still retained its characteristic ridges and craters from the aerosol deposition, but it seems that the fractured particles scattered around the surface has served as growth sites. The enlarged grains have an approximate diameter of 1 µm and the effect proved reproducible in subsequent samples.

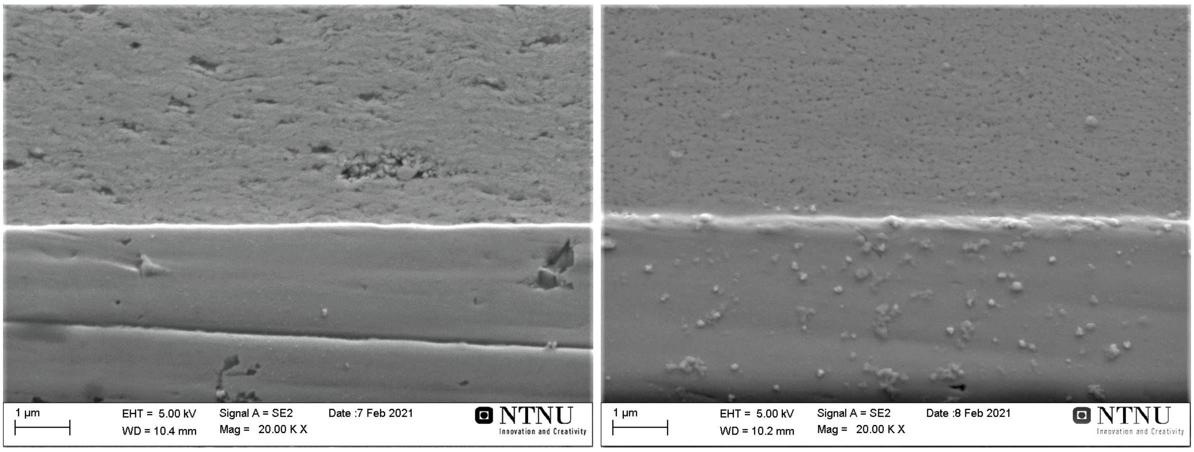

(a) BTSS 3.1 as-sprayed

(b) BTSS 2.3 750 °C

Figure 4.19: BTSS samples interface region

However, the grain growth did not extend past a very thin upper layer on the coating surface, and further down the coating did not have any identifiable grains with clear boundaries (Fig. 4.19). Rather, the coating lost its laminar structure and had an amorphous appearance with evenly dispersed porosity. The coating/substrate remained intact with close contact throughout the sample. This trend was also observed from the top-view during the soaking study once the coating started to crack and fall off, revealing the different layers as seen in Fig. 4.20.

All BTSS samples treated at 750 °C showed long transverse cracks (Fig. 4.21) extending through the coating. BTSS samples 2.1-2.2 differed from the other BTSS samples in that their grain growth initiated at lower temperatures (650 °C, Fig. 4.18c) and it propagated further at 750 °C, resulting in a more complete coverage of the surface with enlarged grains.

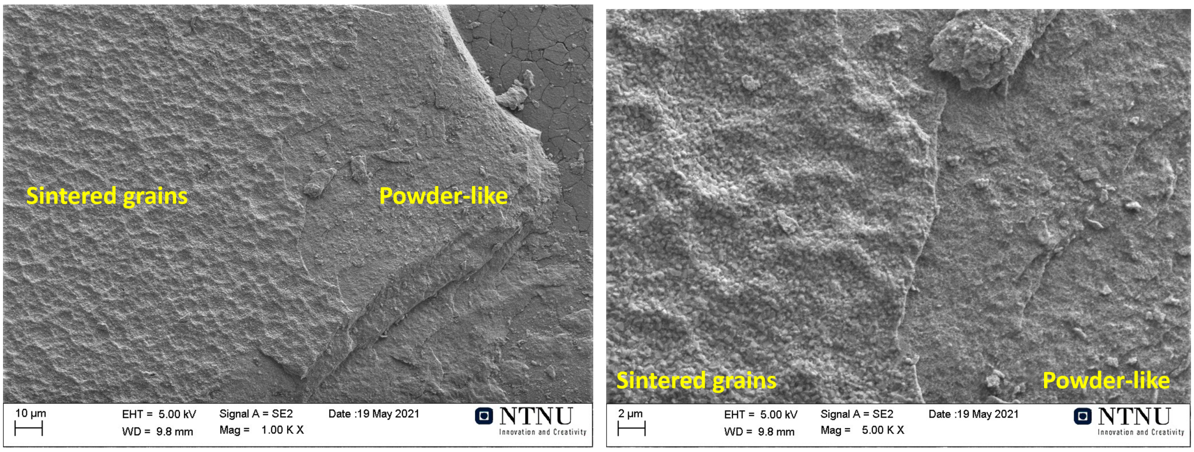

(a) BTSS 6.1 1k magnification after soaking in SBF

(b) BTSS 6.1 5k magnification after soaking in SBF

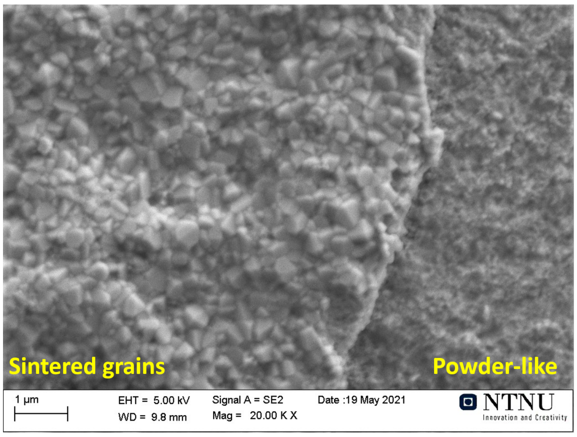

(c) BTSS 6.1 20k magnification after soaking in SBF

Figure 4.20: Different observed layers in BTSS 6.1 (750 °C after soaking in simulated body fluid (SBF), stainless steel substrate is visible in the top right corner of image a).

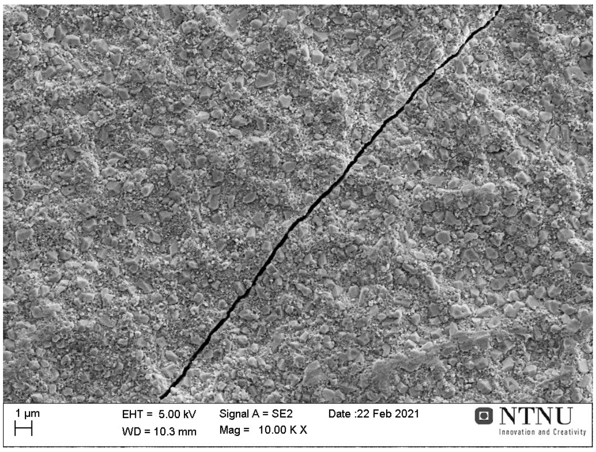

Figure 4.21: BTSS 2.3 750 °C transverse crack

BTTi samples did not form larger clearly defined grains at 750 °C, but the elevated ridges appeared to fuse into flat plateaus (Fig. 4.22a-b). It was not possible to accurately image the coating/substrate interface in the BTTi samples treated at 750 °C, as the coating would delaminate upon sanding/grinding or ultrasonic cleaning. As a consequence, the substrate was imaged after delamination and compared to an as-sprayed substrate (Fig. 4.22c-d). As suggested by FS-XRD (Fig. 4.7), the substrate shows signs of oxidation, and apparent loss of material based on the large amount of porosity compared to the as-sprayed substrate.

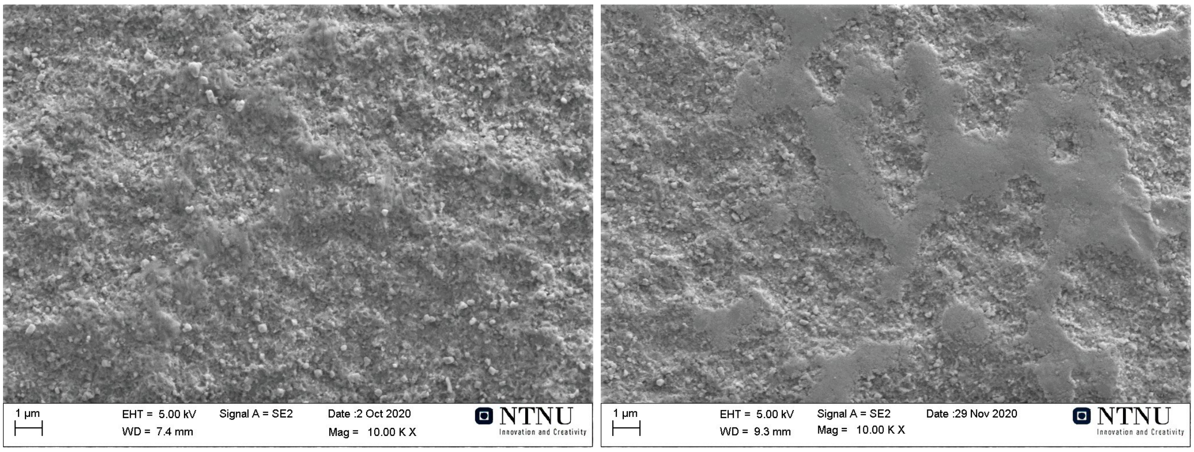

(a) BTTi 2.1 as-sprayed

(b) BTTi 1.4 750 °C

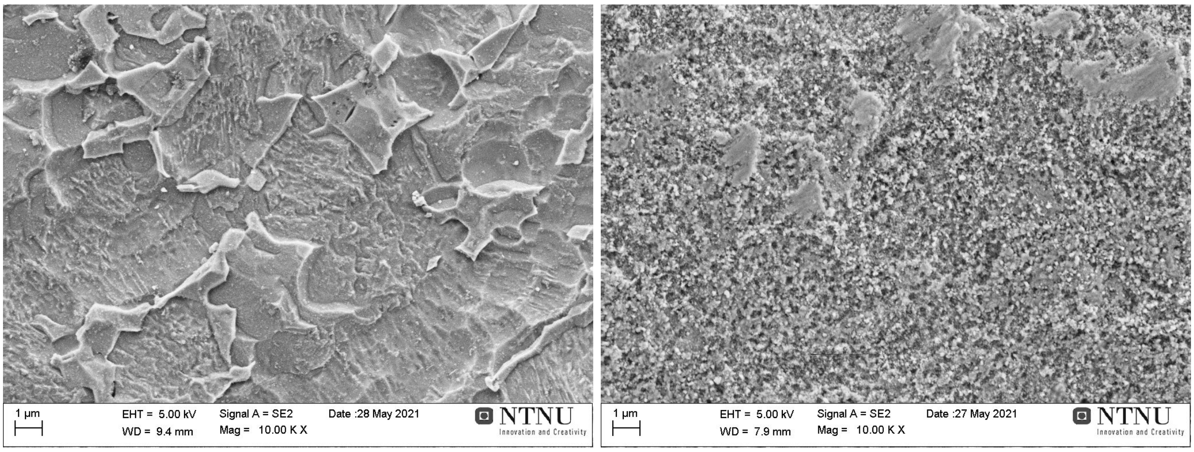

(c) BTTi 2.1 as-sprayed substrate

(d) BTTi 1.4 750 °C underlying substrate

Figure 4.22: Microstructural comparison of BTTi samples

BCZTTi samples stood apart from the BTSS and BTTi ones in that they did not show the same degree of cratering and ridges in their as-sprayed form. This was elaborated upon by Dr. Neamul Khansur in Erlangen, who pointed out that the cratering only occurs when the coatings exceed 7 µm in thickness. There is no apparent change to the actual grains or surface topography as a function of temperature (Fig. 4.23a-b). The surface is made up of flat platelets which appear to be deformed impacted particles which did not change significantly in size or shape through heat-treatment at 750 °C. The same applies to all the lower temperature conditions.

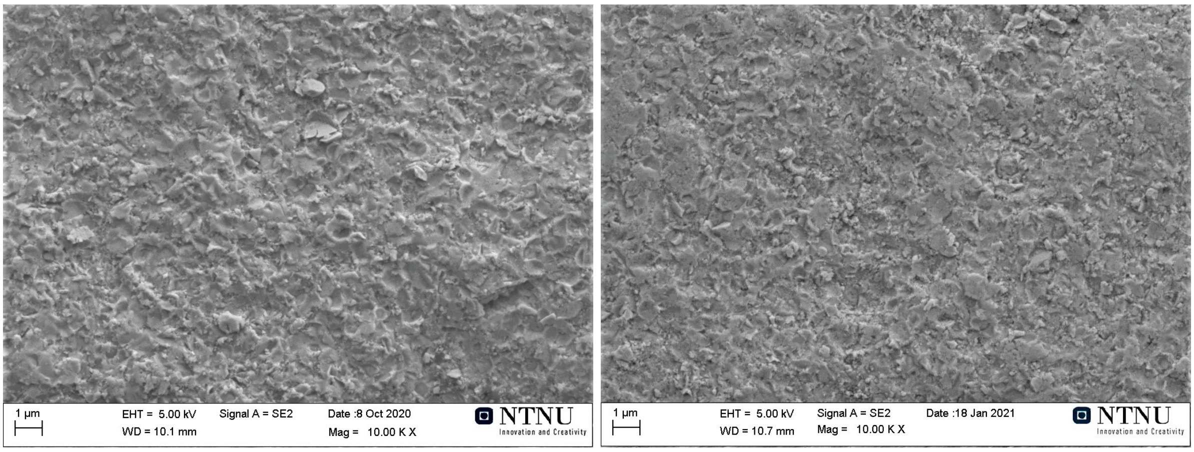

(a) BCZTTi 2.1 as-sprayed (pre-cut)

(b) BCZTTi 1.4 750 °C

Figure 4.23: Microstructural comparison of BCZTTi samples

The structural integrity of the BCZTTi samples was markedly reduced by heat-treatment. Large flakes of coating peeled off after heating the sample to 750 °C and cleaning them in an ultrasonic bath with ethanol (Fig. 4.24a). A closer look at the delaminated regions reveal that the coating has cracked in different layers as the crack propagated towards the surface of the substrate (Fig. 4.24b). Lastly, small radiating cracks can be found throughout the surface (Fig. 4.24c), but no large transverse cracks (as seen in BTSS and BTTi) could be found.

Interface images taken of the BCZTTi samples revealed a large amount of cracking at the coating/substrate interface after heat-treatment (Fig. 4.25b). However, the fact that the interface survived the sanding/grinding needed to get a good interface image implied that the BCZTTi samples were more mechanically robust than the BTTi samples. Damage to the BCZT-Ti6Al4V interface occurred in two separate regions, above and below the interface. Brittle fracture of the ceramic coating occurred above the interface, seen as the upper-most horizontal crack in Fig. 4.25b. Below the interface, ductile fracture can be seen in the substrate by elongated "strings" of metal in the lower left corner (Fig. 4.25b) and the appearance of cracks/porosity.

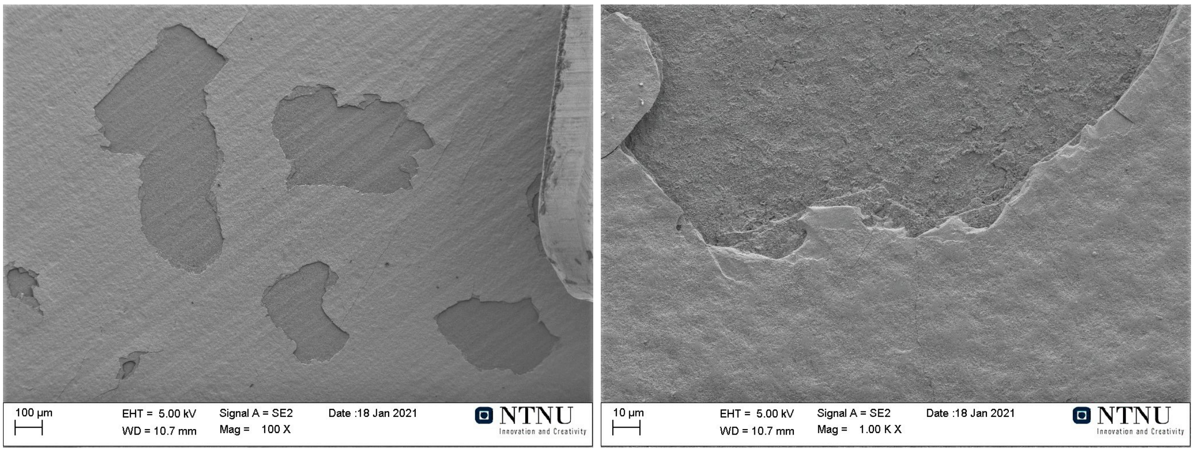

(a) BCZTTi 1.4 750 °C

(b) BCZTTi 1.4 750 °C

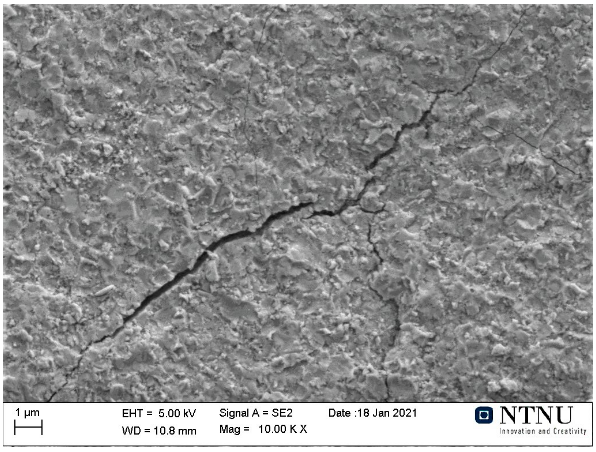

(c) BCZTTi 1.4 750 °C

Figure 4.24: BCZTTi sample damage

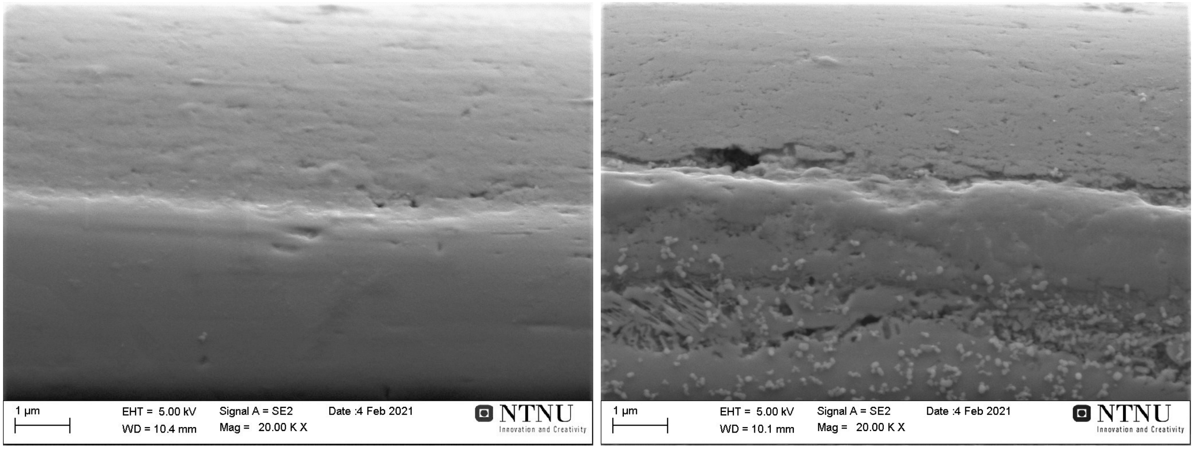

(a) BCZTTi 2.1 as-sprayed

(b) BCZTTi 1.4 750 °C

Figure 4.25: BCZTTi samples interface region

4.3 Changes in mechanical properties after heat-treatment

In order to see how the temperature dependent changes in microstructure affected the mechanical properties of the coating, nano-indentation (NI) was performed on representative samples from each temperature condition. Hardness and reduced modulus values were calculated from force - displacement curves taken from numerous spots on each sample. In this section, a simplified representation of the change in the shape of the force - displacement curves is presented along with figures showing the average hardness (H) and reduced modulus (E_r) values. The full measured force - displacement curves and corresponding calculated values for each curve can be found in appendix. 7.4 and 7.6

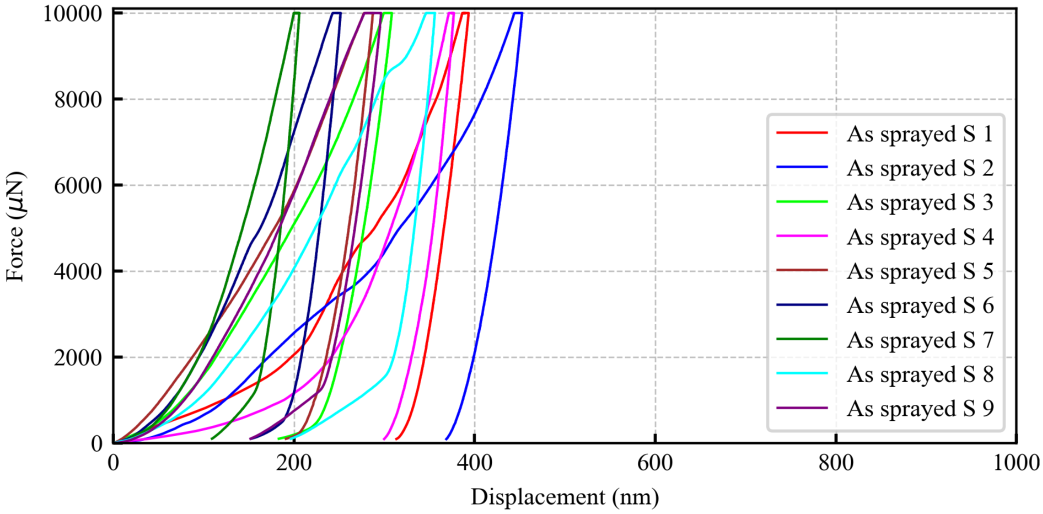

Figure 4.26: Force - displacement curve BCZTTi 2.1 As sprayed. "S" is short for "spot"

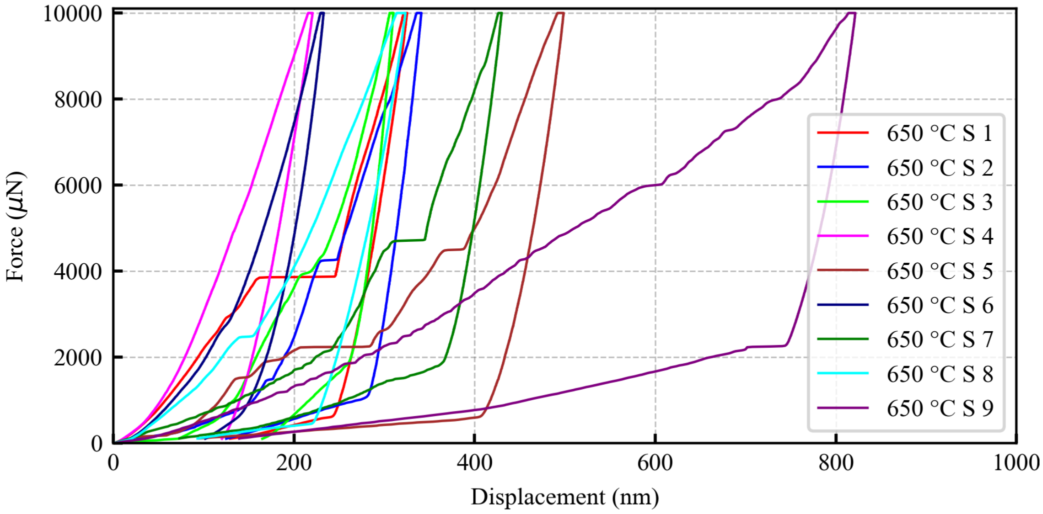

Figure 4.27: Force - displacement curve BCZTTi 1.3 650°C. "S" is short for "spot"

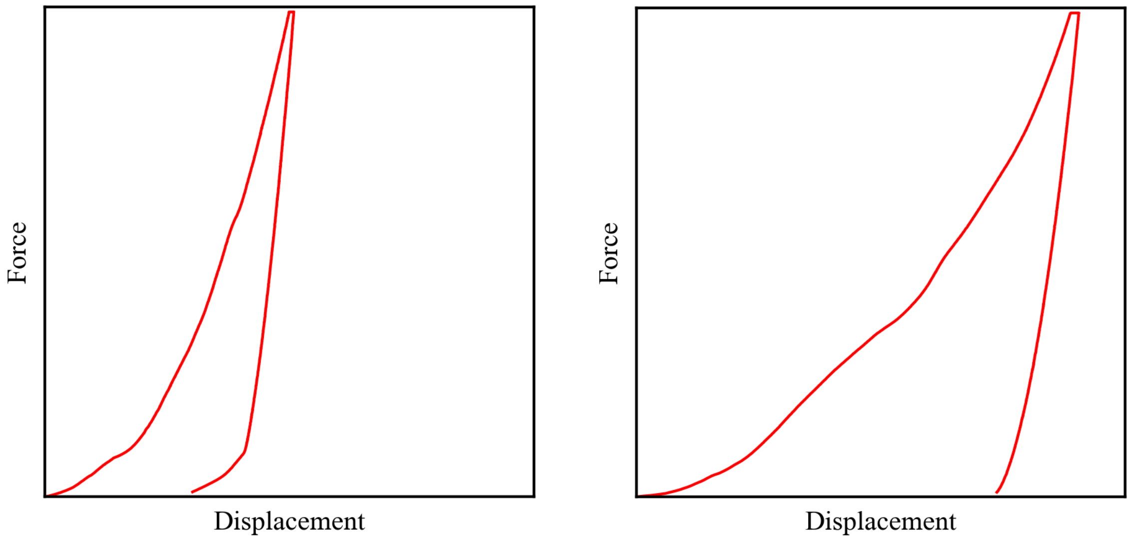

(a) "Normal" force - displacement curve (as-sprayed)

(b) Force - displacement curve containing agglomerated particles (as-sprayed)

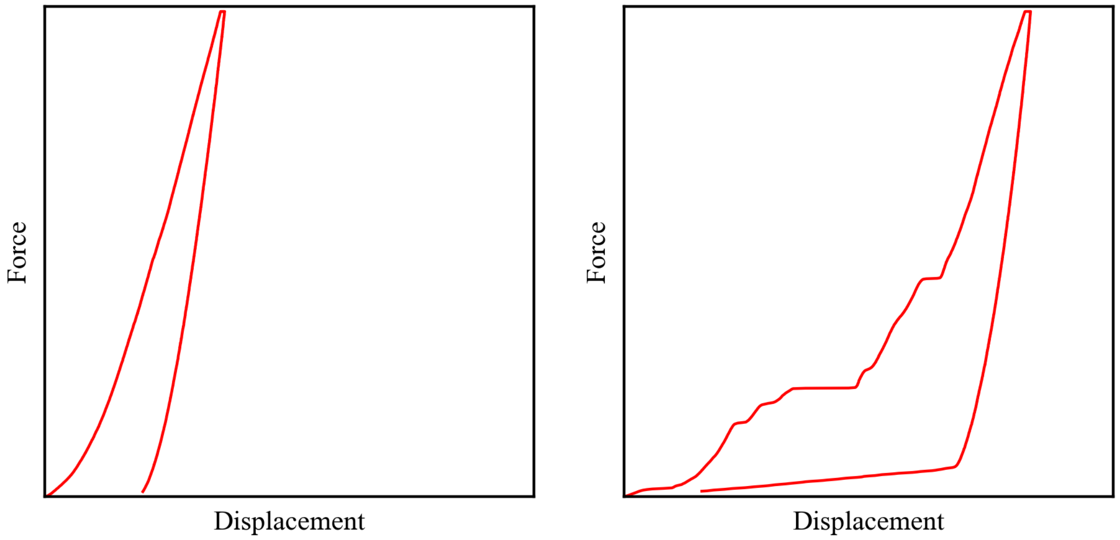

(c) "Normal" force - displacement curve (650 °C)

(d) Defect containing force - displacement curve (650 °C)

Figure 4.28: Comparison between a) "normal" force - displacement curve for BTSS with homogeneous coating characteristics, b) loosely packed coating c) defect containing BTSS coating.

The shape and spacing of the measured force - displacement curves changed markedly for all material systems after heat-treatment as represented by the curves collected from BCZTTi 2.1 (as-sprayed) and BCZTTi 1.3 (650 °C) (Figures 4.26 and 4.27). Fig. 4.28 shows individual force - displacement curves taken from BCZTTi 2.1 (as-sprayed 4.28a-b)) and BCZTTi 1.3 (650 °C 4.28c-d)). Fig. 4.28a represents a "normal" force - displacement curve for an aerosol deposited coating, with an initial slope of 1 between applied force and observed displacement followed by a large increase in applied force vs a small increase in displacement. Fig. 4.28b shows a force - displacement curve of a loosely packed region of coating, characterized by a continued slope of 1 between applied force and observed displacement for the entire measurement. As heat-treatment temperature was increased, an increasing number of force - displacement curves appeared as the BCZTTi curves imaged in Fig. 4.28c-d. Curve 4.28c shows a sharper, narrower curve compared to that in the as-sprayed condition while curve 4.28d showed an overall increased amount of displacement per unit of applied force, mainly from sudden large increases in displacement at constant applied force.

BTSS samples on average exhibited a small increase in hardness and reduced modulus between heat-treatments up to $T \leq 550\,°C$ (Fig. 4.29a-b). Samples treated at 650 °C and 750 °C both had decreased hardness and reduced modulus compared to as-sprayed samples. The variability in the measurements increased significantly for samples treated at $T \geq 650\,°C$

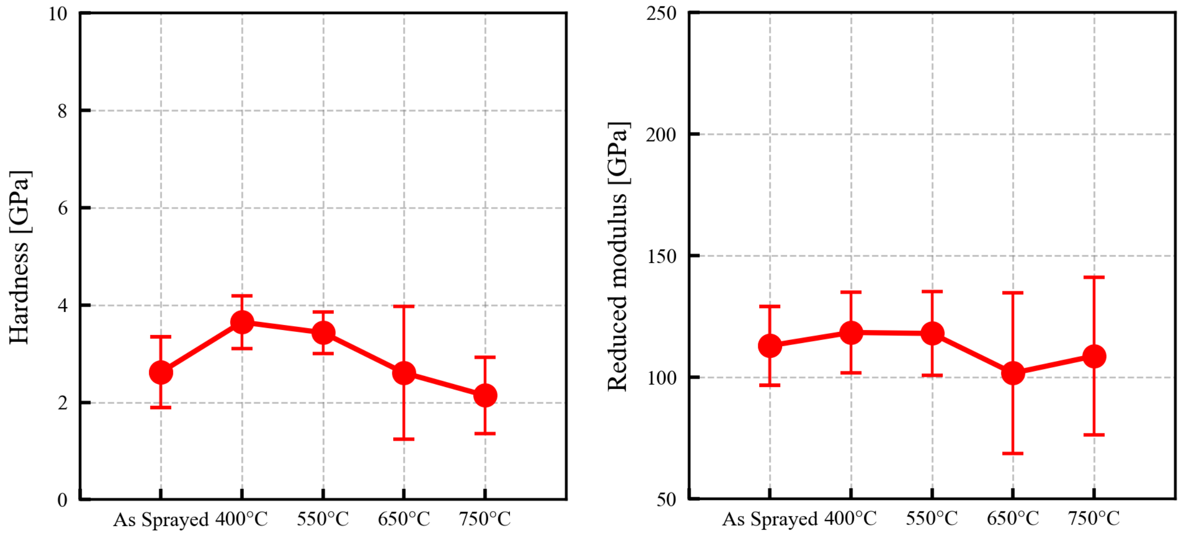

(a) BTSS average hardness

(b) BTSS average reduced modulus

Figure 4.29: Nano-indentation data for BTSS samples as a function of heat-treatment

BTTi samples showed comparable harness values to the BTSS samples but displayed higher values for the reduced modulus as seen in Fig. 4.30a-b. Heat-treatments up to and including 550 °C resulted in a steady increase in both hardness and reduced modulus, but as in BTSS samples, a noticeable decrease occurs at 650 °C. Variability was highest in the as-sprayed and 400 °C conditions and decreased in the $T \geq 550\,°C$ samples. As in other measurements, the BTTi 750 °C temperature condition is not represented in the NI measurements due to the mechanical breakdown of these coatings.

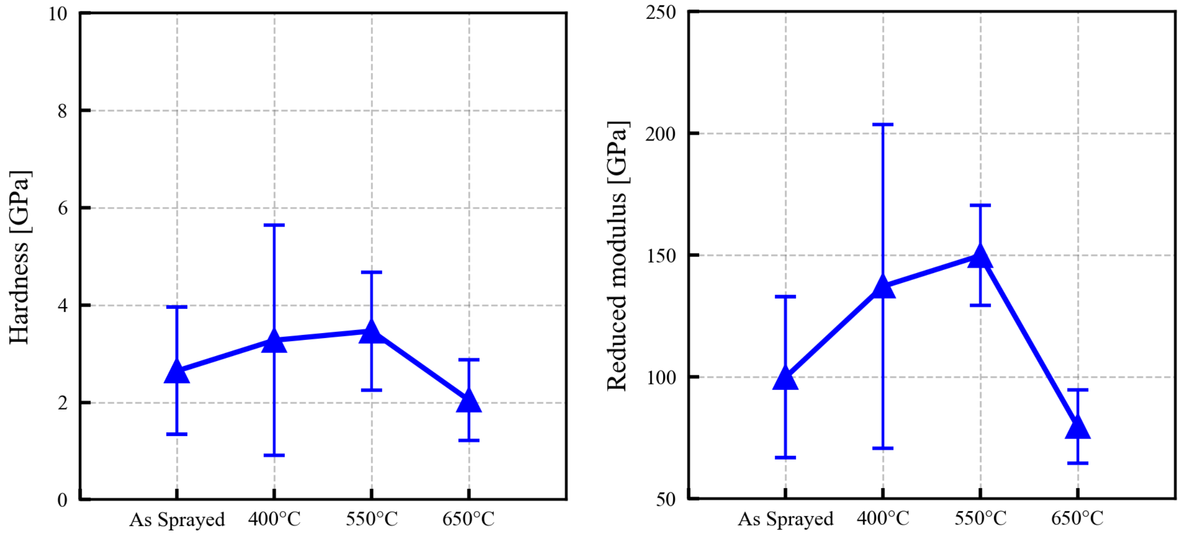

(a) BTTi average hardness

(b) BTTi average reduced modulus

Figure 4.30: Nano-indentation data for BTTi samples as a function of heat-treatment

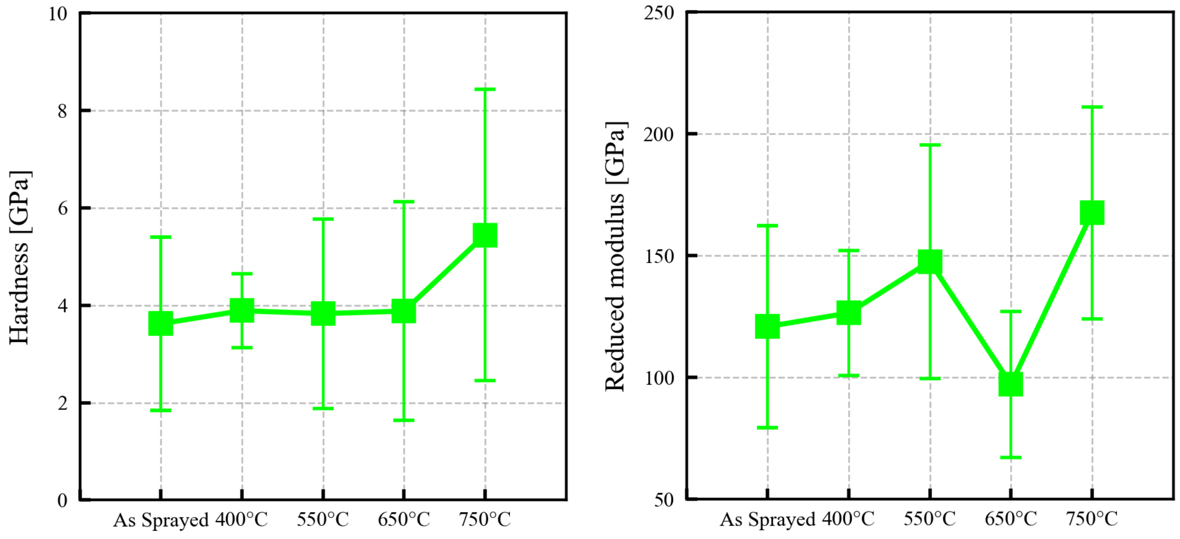

(a) BCZTTi average hardness

(b) BCZTTi average reduced modulus

Figure 4.31: Nano-indentation data for BCZTTi samples as a function of heat-treatment

BCZTTi samples displayed higher average hardness and reduced modulus values compared to the BTTi and BTSS material systems (Fig. 4.31). Hardness values remained nearly constant for all samples heat-treated at $T \leq 650\,°C$, while the BCZTTi sample heat-treated at 750 °C had the highest measured average hardness value of any sample regardless of material system. The average reduced modulus increased with increasing heat-treatment temperatures for all samples except the sample heat-treated at 650 °C which had a significantly decreased average reduced modulus compared to the as-sprayed sample. Variability decreased in the BCZTTi sample heat-treated at 400 °C compared to the as-sprayed sample while samples treated at $T \geq 550$ °C showed increasing variability with increasing heat-treatment temperature.

4.4 Piezoelectric and dielectric properties

In the context of bone replacement materials, a piezoelectric coating's main function would be to facilitate the generation of surface charge in order to attract specific ions from body fluids and initiate the first steps of bone mineralization. Considering this, the ability of the aerosol deposited $BaTiO_3$/BCZT samples to generate and retain surface charge was thoroughly tested. The results in this section are presented in the following order: polarization and strain measurements done with an aixACCT piezo-testing setup, direct piezo-response data measured by the Berlincourtmeter.

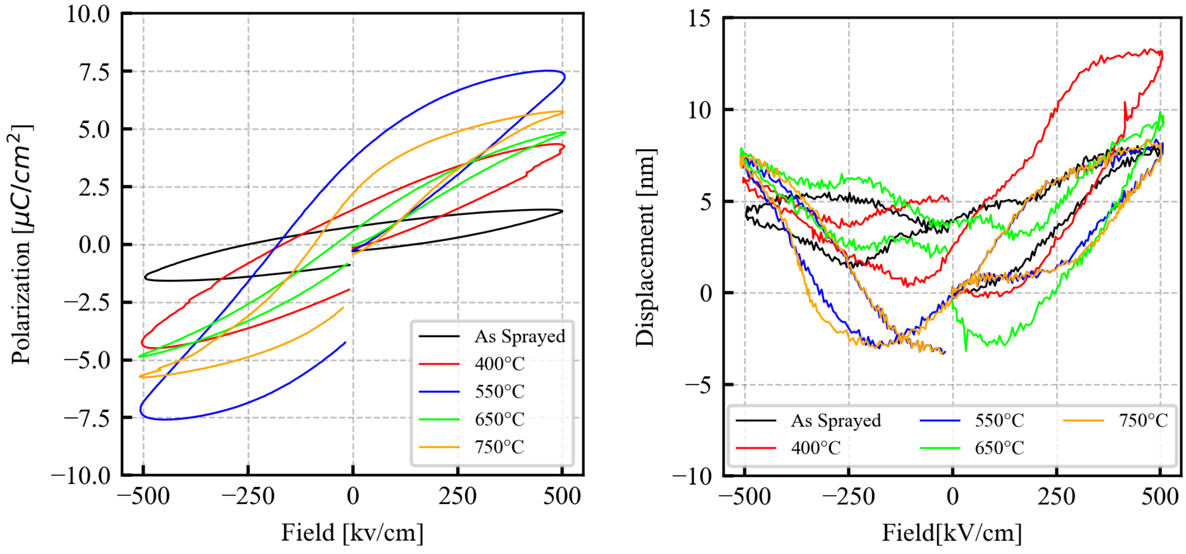

(a) Polarization curve BTSS

(b) Displacement curve BTSS

Figure 4.32: Polarization and displacement measurements for BTSS 3.1 as-sprayed, BTSS 1.3 400 °C, BTSS 1.4 550 °C, BTSS 3.2 650 °C, BTSS 2.3 750 °C.

Polarization measurements for BTSS samples are presented in Fig. 4.32a and show a steady improvement in the polarization behavior with increasing heat-treatment temperature. BTSS samples treated at $T \leq 550$ °C mainly show dielectric behavior with almost symmetrical polarization loops and some leakage current. Yet, as heat-treatments increased in temperature the polarization loops adopted a clear hysteresis character, indicating a transition from dielectric to ferroelectric occurring between 550 °C and 650 °C. This coincides with the appearance of enlarged grains on the surface of the BTSS and the release of strain mentioned earlier. Additionally, the samples treated at $T \geq 650$ °C proved more able to retain their remnant polarization than samples treated at $T \leq 650\,°C$. Lastly, the measured displacement of the coating under an applied electric field is shown in Fig. 4.32b. The measurements proved largely inconclusive as no clear trend was observed, the different loops showed little change between temperature conditions and the obtained displacement values were quite low.

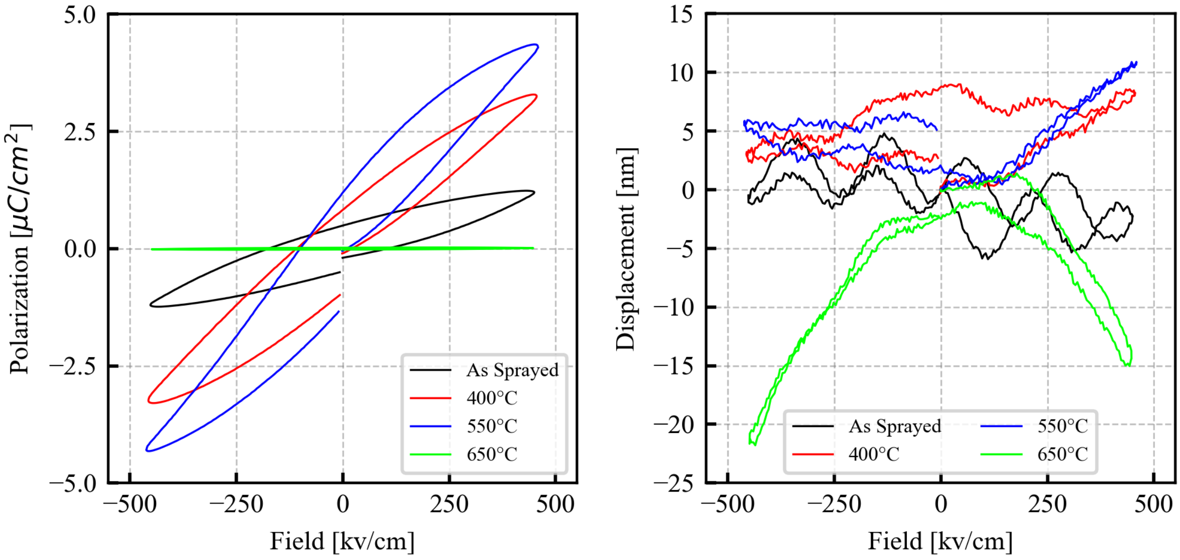

(a) Polarization curve BTTi

(b) Displacement curve BTTi

Figure 4.33: Polarization and displacement measurements for BTTi 2.2 as-sprayed, BTTi 1.1 400 °C, BTTi 1.2 550 °C, BTTi 1.3 650 °C.

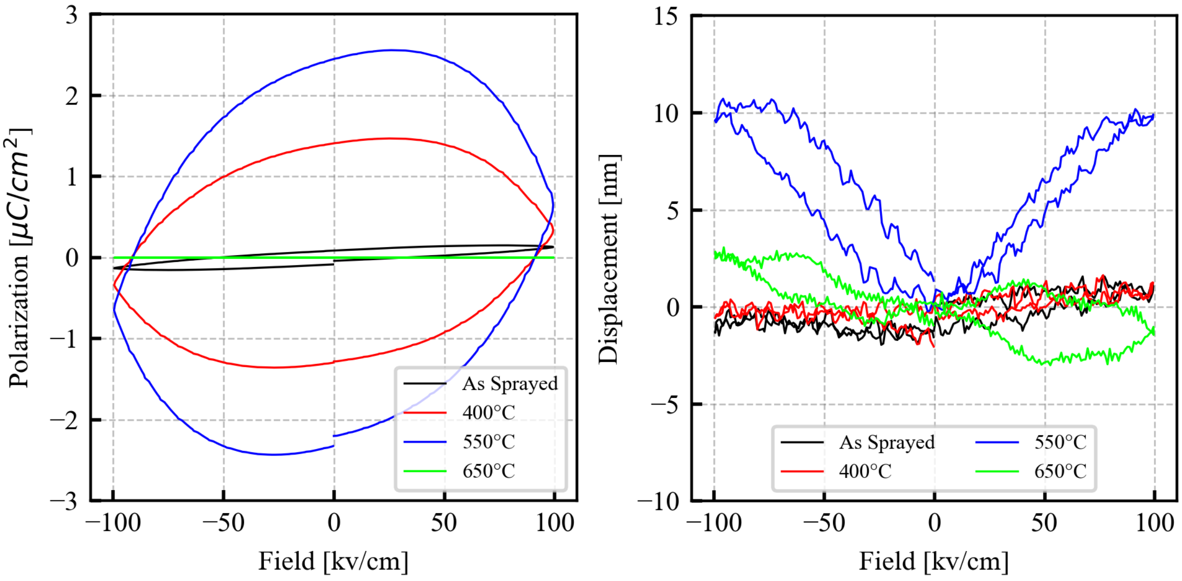

(a) Polarization curve BCZTTi

(b) Displacement curve BCZTTi

Figure 4.34: Polarization and displacement measurements for BCZTTi 3.2 as-sprayed, BCZTTi 1.1 400 °C, BCZTTi 1.2 550 °C and BCZTTi 3.1 650 °C

BTTi samples show a similar trend to BTSS for heat-treatments lower than 550 °C in that the maximum polarization steadily increases with increasing heat-treatment temperature (Fig. 4.33a). The BTTi samples show dielectric behavior with no clear hysteresis character. Polarization for the BTTi sample heat-treated at 650 °C was two orders of magnitude lower than samples treated at $T \leq 550\,°\mathrm{C}$ ($-0.02\,\mu\mathrm{C/cm^2}$ to $0.02\,\mu\mathrm{C/cm^2}$). The displacement curves for BTTi samples seen in Fig. 4.33b are largely inconclusive, but contains a large negative displacement for the 650 °C BTTi sample.

The BCZTTi material system showed substantially higher leakage current compared to the BTSS and BTTi samples based on the polarization loops' almost symmetrical, rounded shape (Fig. 4.34a). Fig. 4.34a shows the BCZTTi polarization curves and one can clearly see the rounded minima and maxima associated with heavy leakage current. As with the BTTi samples, the structural integrity of the samples were reduced by the heat-treatment, and the partially flaked off 750 °C sample was not appropriate for piezo-testing in the aixACCT setup. The displacement curves for BCZTTi (Fig. 4.34b) mainly show values close to zero for all samples the one heat-treated at 550 °C which showed a clear positive symmetric displacement curve.

Direct piezoelectric response measurements for all samples were collected using a Berlincourtmeter and are presented in Fig. 4.35. It is important to note that the measurements only include values taken from the top of the coatings. This was later remedied to include values measured for both the coating facing up and down between the vibrating tips preceding the soaking study. Those measurements are presented in Fig. 4.36.

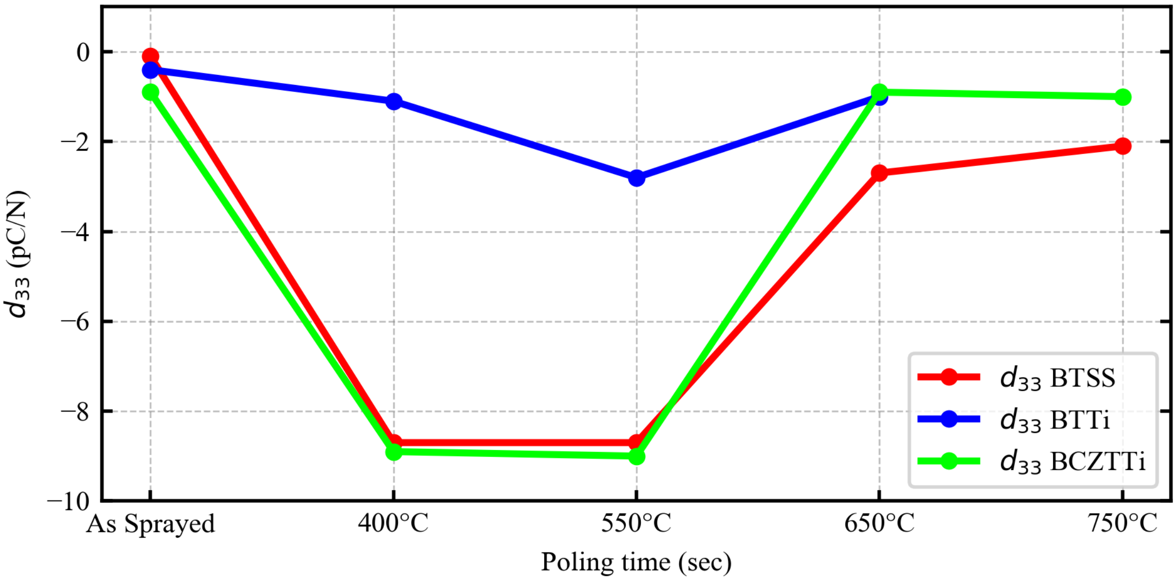

Figure 4.35: Berlincourtmeter d_{33} measurements obtained from the coating facing up in all sample systems.

Berlincourtmeter results varied widely with the highest piezoelectric response being measured in samples treated at 400 °C and 550 °C (Fig. 4.35, specific values are listed in appendix. 7.5). However, these values fluctuated and would decrease over the course of the measurement, i.e. the sample could exhibit an initial value of $-8.7\,\mathrm{pC/N}$ but after 10min in the Berlincourtmeter the samples would show values close to the ones measured in as-sprayed samples. Samples heat-treated at $T \geq 650\,°\mathrm{C}$ did not exhibit this behavior and the values remained constant. No attempt at measuring BTTi 750 °C samples was made due to the demonstrated fragility of the coating.

Based on these preliminary measurements, further attention was given to BTSS samples heat-treated at 750 °C. It was decided that due to their high mechanical stability and hysteresis behavior that they would be subjected to poling by corona discharge and be measured again. These Berlincourtmeter measurements can be seen in Fig. 4.36 and they showed a partially linear increase in piezoelectric response with increasing poling times up to a maximum saturation value after which longer poling times did not seem to significantly affect the measured d_{33} values. Turning the samples so that the coating pointed down resulted in positive d_{33} values which were consistently lower than the negative ones obtained from when the coating was facing up. The variability of the measurements increased markedly for poling times over 420s. The specific for these d_{33} measurements are listed in appendix. 7.2.

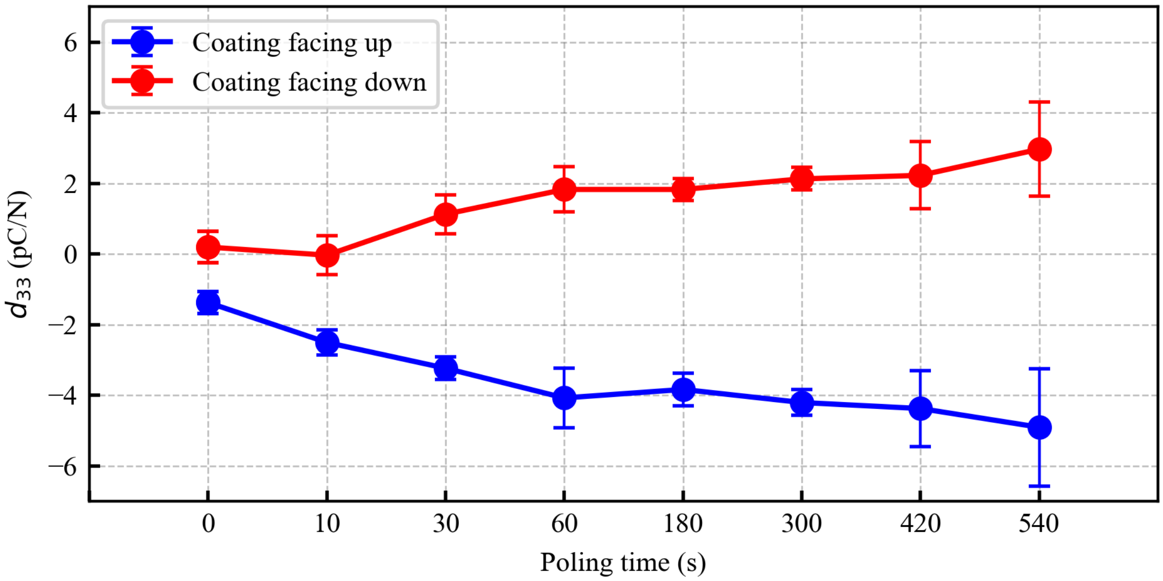

Figure 4.36: d_{33} measurements performed on randomly assigned BTSS samples 8.3-9.4 in preparation for corona discharge poling of BTSS samples 4.1-6.4 for use in soaking study

4.5 Soaking Study

In order to assess the functionality of the aerosol deposited coatings as biomaterials, a soaking study in simulated body fluid (SBF) was conducted to simulate how the material system would behave in the human body. BTSS samples heat-treated at 750 °C were therefore submerged in SBF for 1, 3 and 7 days after being poled for 0, 10, 30 and 300 seconds. After the samples had been soaked for the designated amount of time they were carefully withdrawn from the SBF and prepared for SEM imaging. It was clear before measuring the samples in the SEM that all coatings had suffered substantial damage. One could see with the naked eye that large portions of the coating had flaked off, or disappeared entirely. No debris or visible flakes was observed in the surrounding solution, which was completely clear and colorless.

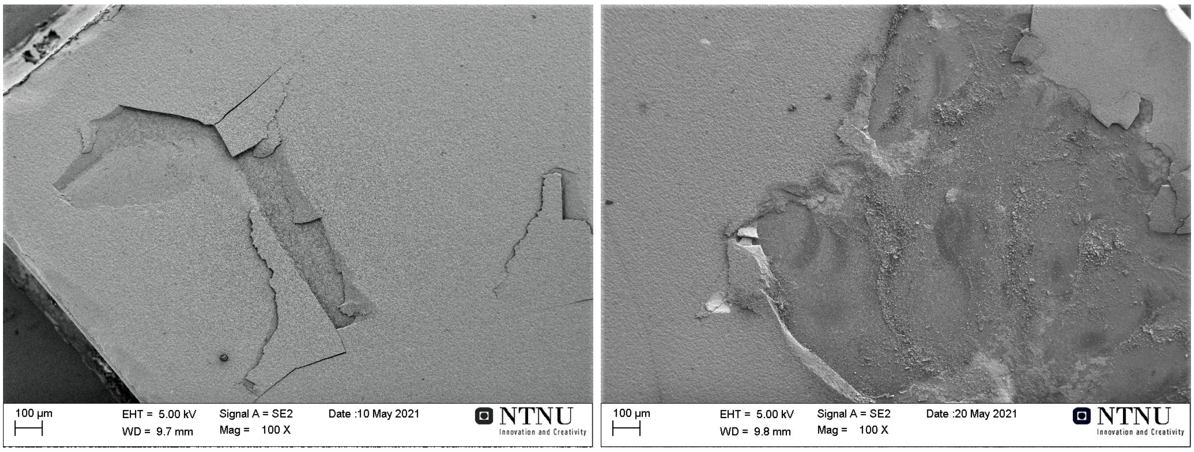

(a) BTSS 4.4

(b) BTSS 5.4

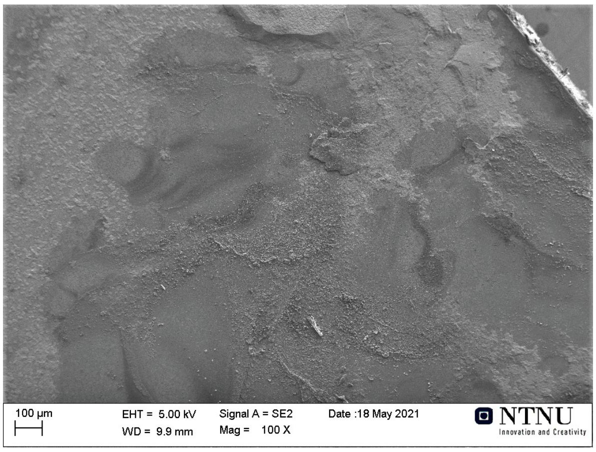

(c) BTSS 6.4

Figure 4.37: BTSS samples after a) 1 day b) 3 days and c) 7 days of soaking in SBF. All samples were poled for 5min using corona discharge.

SEM imaging revealed that the solution dissolved the coating all the way down to the substrate, and that damage increased with longer soaking times. Fig. 4.37 shows BTSS samples 4.4, 5.4 and 6.4 which were submerged in SBF for 1, 3 and 7 days respectively. BTSS sample 4.4 shows the least amount of damage, while BTSS 6.4 has nearly all of its $BaTiO_3$ coating. Delamination and loss of coating appears to initiate at cracks already present in the coating from the preceding heat-treatment.

Surface charge applied to the samples by corona discharge poling also seemed to have a significant effect. Fig. 4.38 shows the percent weight change of every sample as a function of soaking time and poling condition. A clear trend emerged, which was corroborated by SEM imaging that as the poling time and consequently remnant surface charge increased, so did the loss of mass to solution.

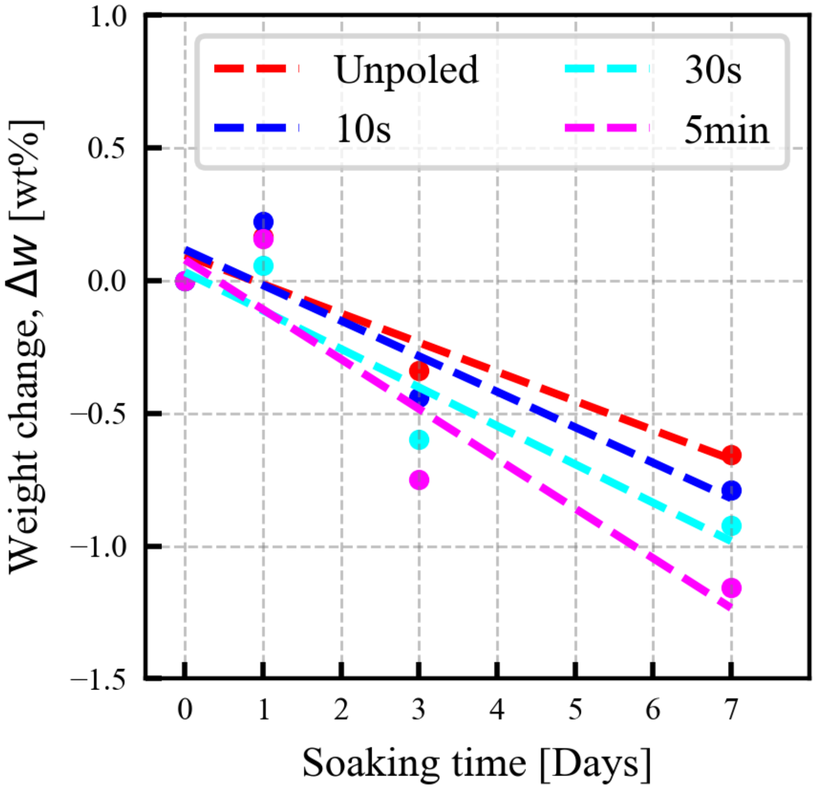

Figure 4.38: Percentage weight change of soaked samples as a function of soaking time and poling condition

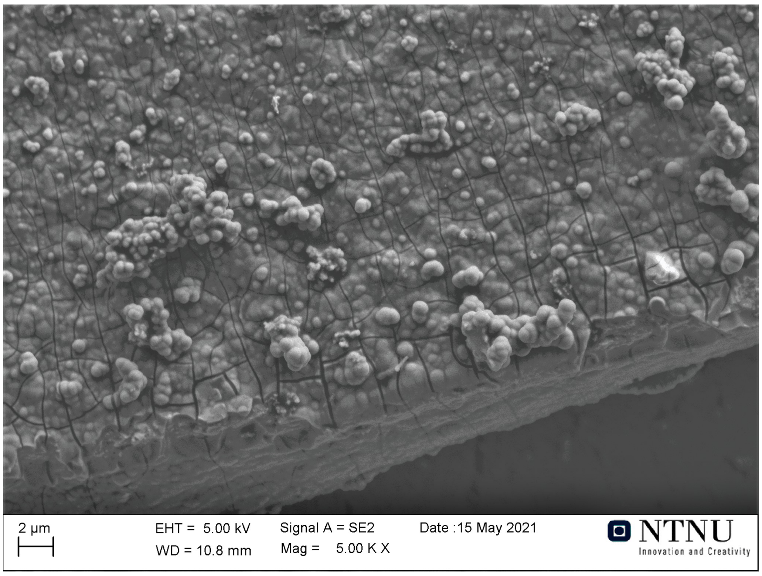

Figure 4.39: Piece of barium titanate coating in the process of delaminating from BTSS 4.4, calcium phosphate globular particles can be seen on top

Calcium phosphate was found in several samples, but it was almost exclusively found on the exposed substrate, not the coating. There was some evidence that calcium phosphate did nucleate on the coating but was lost when that part of the coating delaminated and dissolved. One such loose piece of coating in the process of delaminating can be seen in Fig. 4.39. This effect was only seen in the BTSS 4.4 sample but it is important to note that the other samples either had a lower surface charge, or they had been submerged in SBF long enough for most of the coating to disappear. No clear trend was found between soaking time, poling and calcium phosphate nucleation.

Three types of precipitates were observed on the substrate surface and identified as either calcium phosphate or one of two types of likely barium sulphate morphologies. These three species can be seen in Fig. 4.40a-c with a) being globular calcium phosphate particles on top of a cracked calcium phosphate film, b) shows possible cube-like barium sulphate crystals while c) has large collections of likely barium sulphate rods. EDS maps of a region containing all three types of precipitates can be seen in Fig. 4.41a on top of some residual $BaTiO_3$ coating and steel substrate. Residual $BaTiO_3$ or Ba^{2+} depleted TiO_2 coating can be seen in Fig. 4.41b in the form of barium or titanium (due to overlapping EDS energies) on the substrate surface and underlying the phosphorous rich calcium phosphate film (Fig. 4.41c). Cubic and rod-like sulfur containing crystals can be seen in the middle (cubic), lower center (cubic) and left (rods) parts of the sulfur EDS map (Fig. 4.41d).

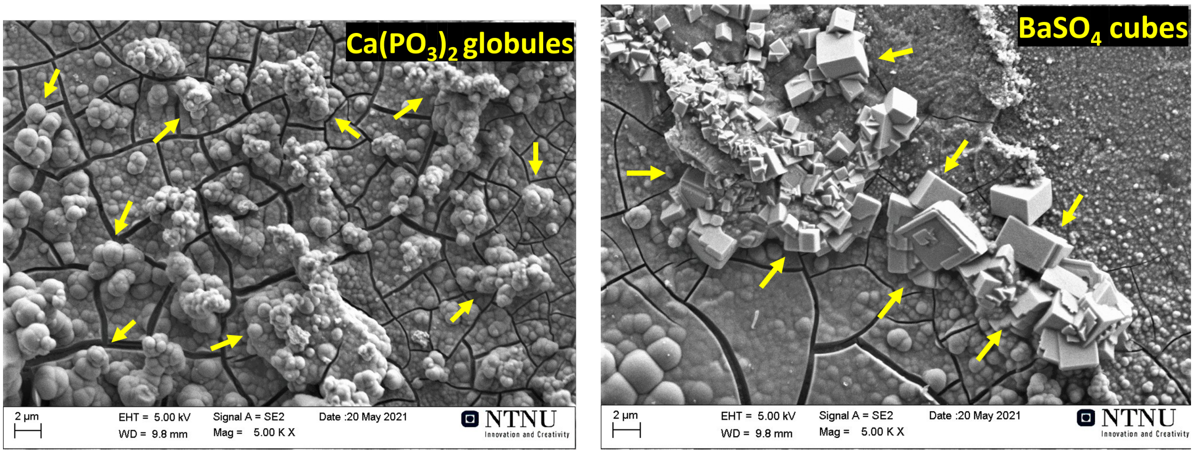

(a) Calcium phosphate globules

(b) Barium sulphate cubic crystals

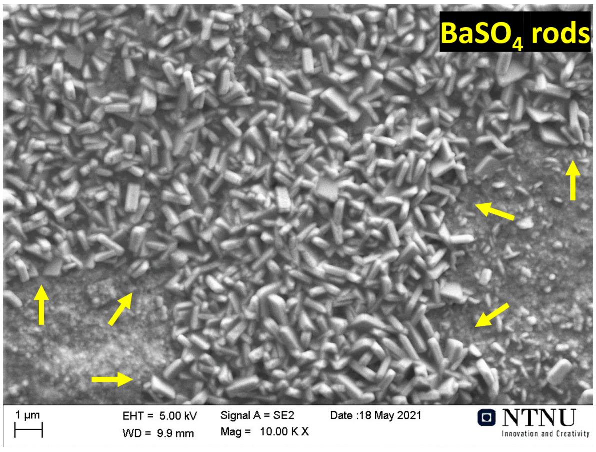

(c) Barium sulphate rods

Figure 4.40: The three different precipitate types seen in samples soaked in SBF.

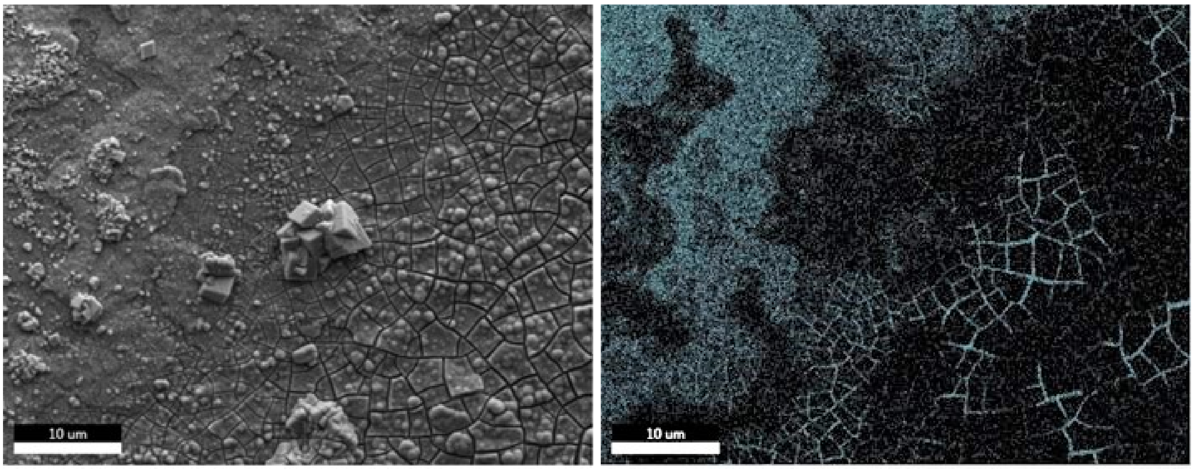

(a) BTSS 6.4 SEM 750 °C

(b) BTSS 6.4 Barium 750 °C

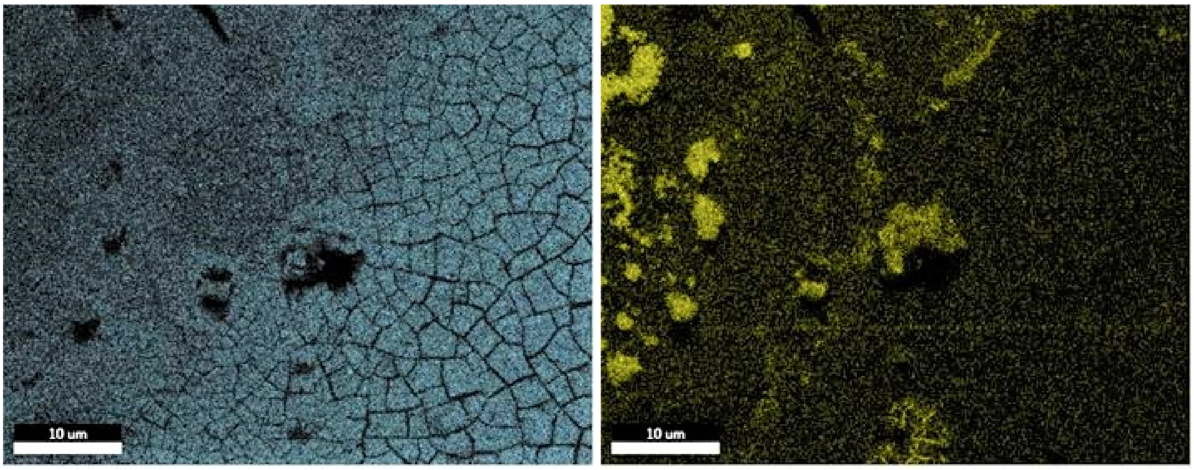

(c) BTSS 6.4 Phosphorous 750 °C

(d) BTSS 6.4 Sulfur 750 °C

Figure 4.41: EDS map of BTSS 6.4 after 7 days of soaking in SBF.

The last measurement conducted was FS-XRD which corroborated the observed presence (by SEM/EDS) of calcium phosphate on certain samples with the appearance of a new peak at 32.4°(Fig. 4.42) which was matched to a calcium phosphate PDF (PDF 00-050-0584). The full stacked diffractograms for all SBF soaked samples before and after soaking in SBF can be found in appendix. 7.3.

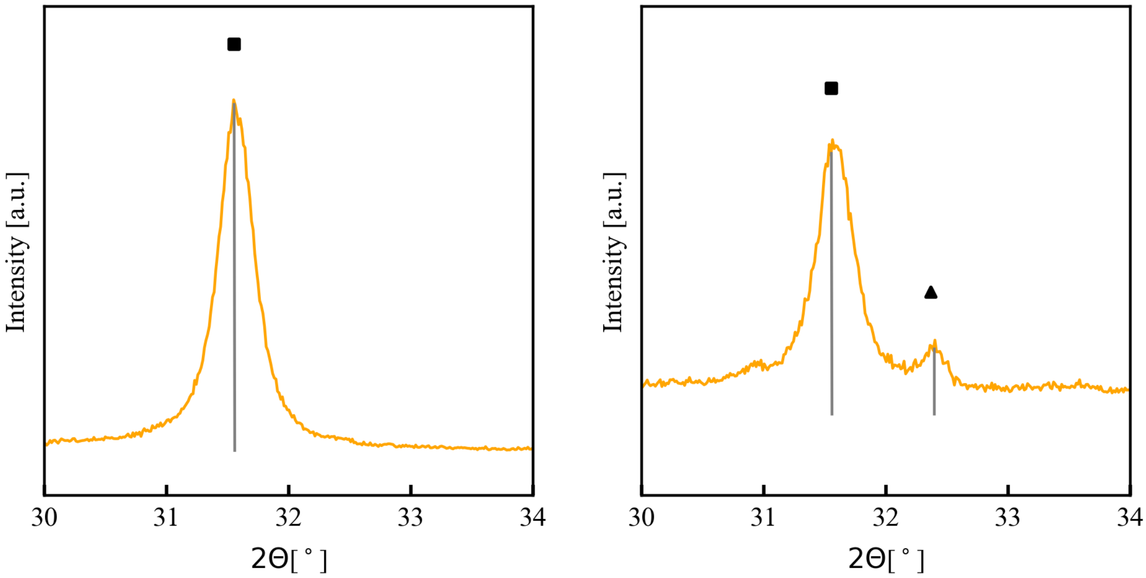

(a) Pre-soaking

(b) Post-soaking

Figure 4.42: FS-XRD diffractogram showing appearance of characteristic peak corresponding to calcium phosphate (PDF 00-050-0584)(◆) next to tetragonal BaTiO$_3$ (PDF 04-010-4893) (■)

5 Discussion

5.1 Effects of heat-treatment

5.1.1 Composition

Crystal structure

A characteristic feature of aerosol deposited ceramics is that they exhibit large residual stresses and nanosized grains and crystallites [67, 86–90], this was observed in all aerosol deposited samples delivered to NTNU from Erlangen. A good indicator of this residual stress can be seen as the initial mismatch between calculated lattice parameters a and c in as-sprayed samples compared to the relevant PDF files (PDF 04-010-4893 $BaTiO_3$ and PDF 01-086-8334 BCZT)(Fig. 4.15a, 4.16a and 4.17a). This mismatch arises from compressive stress-induced lattice distortions at the coating-substrate interface imparted by particle impact during deposition [76].

As a heat-treatment of 400 °C was applied, all samples exhibited a clear reduction in lattice parameter lengths, regardless of the type of substrate (Fig. 4.15a, 4.16a, 4.17a). This initial reduction brought the lattice parameters of all samples closer to the values listed in the relevant PDF standards, indicating a release of residual stress. This effect is supported by the work done by Khansur et al. [76] who reported a maximum biaxial compressive residual stress of -800 MPa in as-sprayed $BaTiO_3$ on 304SUS stainless steel, mainly at the coating-substrate interface. This stress was reduced to -271 MPa after heat treatment in air at 500 °C, and the effect was attributed to the different thermal expansion behavior of the coating and the substrate.

However, the different material systems started behaving differently with subsequent treatments at temperatures higher than 400 °C. BTSS samples displayed a gradual increase in lattice parameters with increasing heat-treatment temperatures, diverging from the PDF standard. Lattice parameters in BTTi and BCZTTi samples on the other hand converged towards their PDF standards.

This effect is likely due to the different substrates in the three material systems, 304SUS stainless steel and Ti6Al4V alloy. Reported thermal expansion coefficients for $BaTiO_3$ and 304SUS stainless steel is given in Table. 5.1 and one can see that the $BaTiO_3$ posesses a slightly smaller coefficient than the steel. As such, when the BTSS samples are heated the coating will be under developing tensile stress at the interface from the substrate, which counters the residual compressive stress from the deposition process. However, upon cooling this stress will change to compressive again. It is therefore possible that the BTSS sample coating is initially relaxed by heat-treatment, but once the temperature is increased, the difference in expansion between the coating and steel becomes more pronounced. This could mean that the heat-treatment reintroduces more compressive stress than it alleviates at temperatures higher than 400 °C for

BTSS samples. This could be why a gradual return to the as-sprayed lattice parameters is observed with increasing heat-treatment temperature for the BTSS samples.

Conversely, the BTTi and BCZTTi sample coatings become more similar to their respective PDF values after the initial relaxation. This is possibly due to the thermal expansion coefficient mismatch being so large between $BaTiO_3$ and Ti6Al4V (Table. 5.1) that after the first heat-treatment the coating is not in proper contact with the substrate. This is supported by the delamination observed in BTTi and BCZTTi samples seen in section 4.2. As such, the resulting semi- or fully free-standing film would not experience stress from the substrate anymore, and therefore behave more similarly to the unconstrained PDF. This is supported by the literature, as seen in Hoshina et al. [91] who reported considerably lowered residual stress in free-standing films compared to films connected to a substrate.

The clear reduction in crystallite size from the starting powders to the aerosol deposited coatings is explained by the kinetic fracture of the sprayed particles. When a particle strikes the surface of the substrate, its kinetic energy is dissipated by breaking up the particle. This in turns leads to a reduction in crystallite size as the resulting fragments will have crystallites which are a fraction of the original crystallite size of the starting particle [68, 83]. This reduction in crystallite size is clearly seen in Fig. 4.1 by the substantial peak broadening in the XRD-diffractogram for the aerosol deposited samples compared to the starting powders along with the loss of peak-splitting which is consistent with nano-sized $BaTiO_3$ crystallites [91–93]. This effect is explained by the Scherrer equation which relates sub-micron crystallite sizes (D) in a solid to diffraction peak broadening [94, 95]:

$$D = \frac{K\lambda}{\beta cos\Theta} \tag{5.1}$$

Where K is the shape factor, λ us the wavelength of the X-rays, Θ is the Bragg angle and β is the corrected full width at half maximum (FWHM). Crystallite sizes increased with increasing heat-treatment temperature (Figures. 4.15b, 4.16b, and 4.17b) from the fusing of particles in the coating to form a more bulk-like structure (further explained in section. 5.1.2). This was further supported by a slight narrowing of the diffraction peaks for all samples with increasing heat-treatment temperature (Figures. 4.2, 4.6, and 4.8).

Chemical composition

The most prevalent chemical transformations observed in the aerosol deposited coatings after heat-treatment were the formation of barium chromate in the BTSS samples treated at 750 °C and the oxidation of the Ti6Al4V substrate in the BTTi samples.

The oxidation of the Ti6Al4V substrate was mainly seen in the BTTi samples heat-treated at 750 °C, specifically as a porous TiO_2 coating underlying the delaminated $BaTiO_3$ (Fig. 4.22d). The presence of TiO_2 in the SEM measurements was corroborated by FS-XRD which had a number of small peaks corresponding to rutile TiO_2 (PDF 04-003-0648). Similar results were reported by Poon [1] who identified a similar oxidised interlayer between a Ti6Al4V substrate and a $CaTiO_3$ coating at temperatures as low as 500 °C. This effect has also been observed at the interface between stainless steel and Ti6Al4V [96], as well as in core-shell nanostructures at the metal-oxide interface [97].

It is likely that the oxidation of the Ti6Al4V substrate at the coating-substrate interface contributed to the degradation and subsequent delamination of the $BaTiO_3$ coating through void-induced loss of contact between the substrate and the coating. The porous structure observed in the Ti6Al4V substrate can possibly be explained by the Kirkendall effect where voids are created at the interface between two materials as a consequence of the materials having different ion diffusion rates. If accurate, this is also possibly what occurs at the BCZT-Ti6Al4V interface in BCZTTi samples treated at 750 °C (Fig. 4.11a) which show diffusion of aluminium into the BCZT coating as well as the clear formation of voids below the coating-substrate interface.

The formation of barium chromate in the BTSS samples was highly reproducible, as it was seen in all samples heat-treated at 750 °C except BTSS 2.2 (Fig. 7.1, 4.2 and 4.3). The presence of chromates which is normally used to manufacture leather products, paints, cement, mortar and anti-corrosives, is highly undesirable in a biomaterial. Chromates are known allergens and have been reported to cause allergic reactions in workers such as dermatitis and irritant dermatitis resulting in skin ulcers [98–100]. Naturally, these are not compounds one would wish to have in an implant material, where they might cause complications in tissues surrounding the implant site. The barium chromate likely formed as a result of temperature dependent chromium diffusion from the substrate into the coating based on the lack of barium chromate peaks in temperature conditions lower than 750 °C. Diffusion of chromium into the $BaTiO_3$ was further supported by EDS and SIMS measurements.

When evaluating the EDS maps, it is important to choose the correct elements to measure, which for BTSS samples in this thesis were barium, titanium, iron, oxygen and chromium. These elements were chosen to form the basis of what was considered the coating and substrate in the EDS measurements (in addition to morphological/microstructural inspection) on the basis that they were the most abundant elements in each respective phase. It should be noted that barium and titanium did not show any significant diffusion at the coating-substrate interface and it was difficult to distinguish whether a signal originated from barium or titanium due to their overlapping energies in EDS (Table 3.1). As such, special attention was given to chromium and oxygen.

The EDS chromium map (Fig. 4.9c) shows dark spots at the substrate-coating interface in the otherwise homogeneous green Cr phase indicating that there is a depletion of the chromium content at the interface due to diffusion into the coating. This is well supported by the literature which has shown that intergranular chromium precipitation occurs in austenite at 500 °C to 800 °C, resulting in a depletion of chromium at the grain bounderies [101].

This effect was suggested by Thorvaldsson [102] to be due to the low diffusion coefficient of chromium in 304SUS stainless steel at 600 °C - 700 °C which he calculated to be about $10^{-21} m^2/s$ leading to the creation of depletion regions as the steel is not able to fill the voids by diffusion from the bulk. This depletion region was also observed in the ToF-SIMS depth profile for the BTSS sample heat-treated at 750 °C. In Fig. 4.13 one can see that the signal for chromium is reduced to zero between the two vertical dashed lines denoting the coating-substrate interface before gradually increasing through the coating to the coating surface (Fig. 4.14).

The wide distribution of chromium throughout the $BaTiO_3$ coating is possibly due to chromium being able to fill the B-sites of perovskites [46], allowing it to diffuse through the octahedral holes. The driving force for this diffusion could be chromium's high affinity for oxygen driving it towards the surface-gas interface along a steep concentration gradient. This diffusion to the surface is normally what gives stainless steel its resistance to corrosion as chromium will diffuse from the bulk steel to the surface in order to form a chromium oxide passivation layer which protects the steel from further oxidation [42, 43].

In addition to its affinity for oxygen, chromium also has a strong affinity for carbon, which has the opposite effect of the chromium oxygen passivation layer. Chromium will upon contact with carbon form different chromium carbides at the expense of the surrounding chromium concentration in the stainless steel, leading to depassivation of the steel in small areas [16]. This becomes interesting when considering the BTSS 2.2 sample which had a dense interlayer of carbon at the coating-substrate interface (Fig. 4.4), and no barium chromate diffraction peaks (Fig. 4.3). It is possible that the lack of barium chromate in this sample and the presence of carbon at the interface is correlated in that carbon serves as a diffusion barrier and traps the chromium found at the coating-substrate interface by forming chromium carbides.

It is however, unclear what the specific identity of the carbon is as the BTSS 2.1 and 2.2 samples showed clear diffraction peaks for graphite, but graphite does not generally form at temperatures below 1000 °C [103] and shows significant oxidation in atmospheric conditions at temperatures over 200 °C [104, 105].

It was suggested by Dr. Khansur who had handled the BTSS samples before they underwent aerosol deposition that a potential source of carbon at the coating-substrate interface could be a carbon based adhesive which had been used to protect the mirror-polish of the stainless steel substrates when they were delivered by INOX-COLOR GmbH & Co KG. It is unknown what the exact composition of the adhesive was, but one could assume that is was a standard polymer adhesive such as polyurethane. Polyurethane and other similar adhesives will generally combust in the presence of oxygen at temperatures surpassing 400 °C [106] which is why one would not expect there to be such a substantial amount of carbon in a BTSS sample heat-treated at 750 °C. Because the carbon is clearly not combusted, one can assume that the coating-substrate interface is devoid of oxygen gas during heat-treatment.

5.1.2 Temperature effect on stress development and microstructure

Stress development

Temperature programs were prepared based on thick film thermal stress calculations meant to predict the temperature at which samples would crack from thermally induced stress. This was done as the mechanical integrity of the coating was hypothesized to be the limiting factor when trying to improve the electrical properties. The thermal stress calculations utilized part of a linear model (equation 5.2) put forward by Desu et al. [107] and modified by Han et al. [108].

$$\sigma_{th} = \frac{E_f}{1 - \upsilon_f}(\alpha_f - \alpha_S)(T_d - T) \tag{5.2}$$

Where E_f is the elastic modulus of the film, υ_f is Poisson's ratio, α_f is the thermal expansion coefficient of the film, α_S is the thermal expansion coefficient of the substrate, while T_d and T is the heating and working temperature respectively. Working temperature refers so the temperature at which subsequent testing was done, which in this thesis is room temperature. Table 5.1 includes all the values used to predict the thermal stress.

Table 5.1: Values used to predict thermal stress in the aerosol deposited samples during heat-treatment.

Parameter	Value	Ref.
Elastic Modulus	115 GPa	[39]
Poisson's ratio	0.35	[109]
Thermal Expansion Coefficient $BaTiO_3$	$17.5 \cdot 10^{-6}/K$	[1]
Thermal Expansion Coefficient 304SUS	$18 \cdot 10^{-6}/K$	[110]
Thermal Expansion Coefficient Ti6Al4V	$8 - 10 \cdot 10^{-6}/K$	[111]
Bending Strength $BaTiO_3$	35-79 MPa	[112]

As the bending strength was reported for bulk ceramics, the lower end of the reported range was used as a likely critical stress value for when cracking would occur within the coating as temperature increased (critical stress and temperature shown as solid and dotted red lines respectively in Fig. 5.1). The maximum temperature of two heating programs were therefore assigned to values slightly larger and smaller than the temperature corresponding to the critical bending strength. These two heating programs corresponded to the 550 °C and 650 °C conditions, with the 750 °C condition being added in order to have three sample conditions with a 100 °C-step gradient.

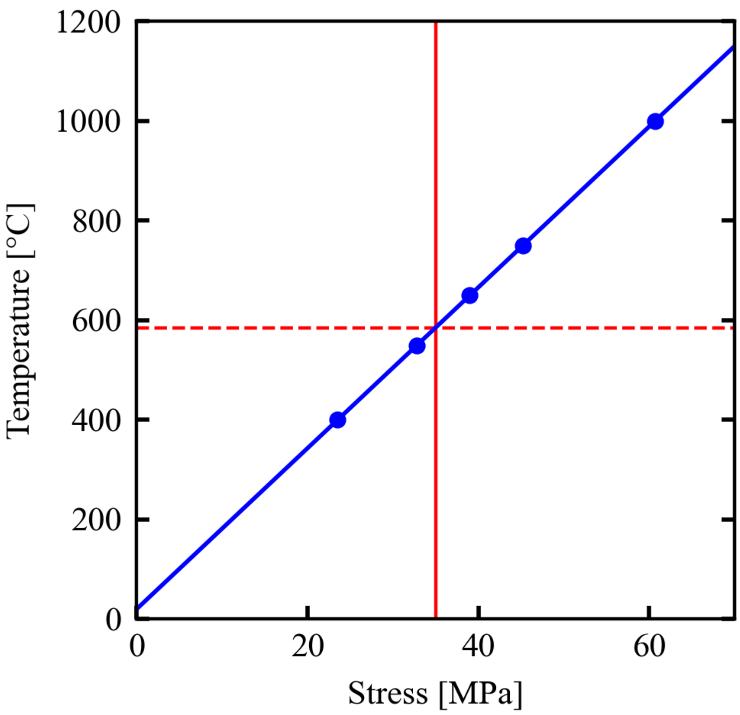

Figure 5.1: Thermal stress prediction for $BaTiO_3$ on 304SUS stainless steel

The lowest temperature condition 400 °C was chosen based on previous work done by the collaborators in Erlangen, Germany [76]. It was included in order to see whether the samples behaved similarly in the current study compared to what the collaborators had already measured. Lastly the 1000 °C condition was chosen based on an expression modelling the optimal annealing temperature (Equation. 5.3, T_{mp} is the melting point of the material) put forward by Exner et al. [113]. However, the 1000 °C temperature condition was discontinued after only one treatment as the coatings treated at this temperature completely delaminated and scattered across the crucible.

$$T_{annealing} = \frac{1}{6}T_{mp} + 730K \tag{5.3}$$

In order to compare the different material combinations, BTTi and BCZT samples were also put through the same heat programs. However, the thermal stress predicted by the Desu/Han model for $BaTiO_3$/BCZT samples on Ti6Al4V is much higher than what is likely occurring during heat-treatment as it predicts cracking just 30 °C above room temperature as seen in Fig. 5.2.

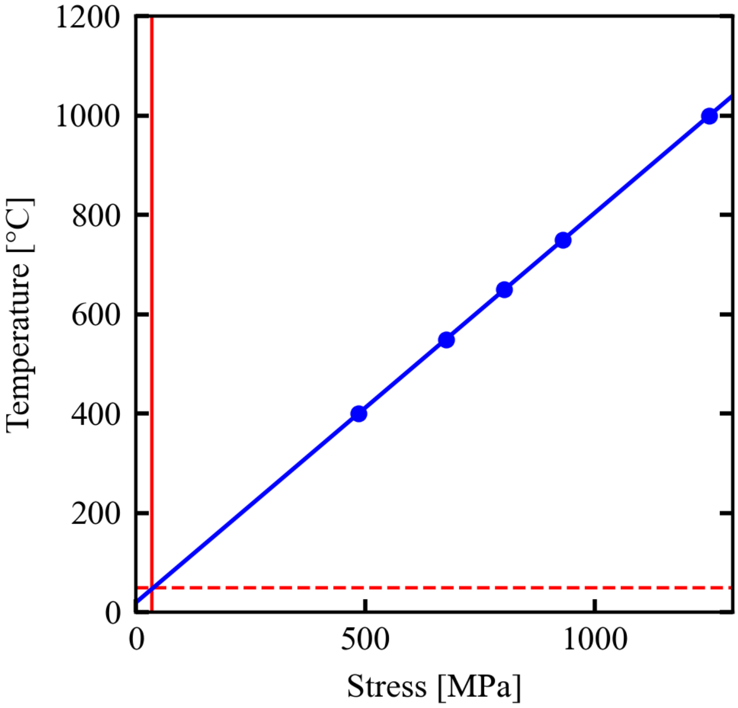

Figure 5.2: Thermal stress prediction for $BaTiO_3$ on Ti6Al4V alloy

Furthermore, complete breakdown of the BTSS sample coatings and delamination was first observed at 1000 °C which corresponds to a thermal stress of roughly 60 MPa. If the Desu/Han model accurately depicted the thermal stress in the BTTi and BCZTTi samples, this effect should have occurred below 100 °C. It can therefore be inferred that the Desu model becomes unreliable when the thermal expansion coefficient difference between the coating and substrate becomes too large. However the model accurately predicted the formation of cracks in the BTSS material system where cracking was first observed in samples treated at 650 °C and further propagated as temperature was increased to 750 °C.

Although the Desu model does not accurately predict the critical temperature at which BTTi and BCZTTi coatings will crack, it is still likely that the damage observed in these two material systems is derived from the thermal expansion coefficient mismatch between the coating and the substrate.

This is supported by Hosina et al. [91] who actually turned this effect into a part of the experimental procedure in order to make free-standing aerosol deposited $BaTiO_3$ films by annealing them at high enough temperatures for them to detach from the substrate. This behavior can be explained by the high residual stress seen in aerosol deposited coatings as a result of the impacts of high kinetic energy particles [68, 88–90]. Specifically, this internal stress increases with coating thickness as a function of successive impacts (hammering-effect) and increased particle-particle interactions. Because of this, thicker films are more susceptible to delamination from external stresses due to the increased internal stress contribution from the deposition process [114]. As such, when the sum of the internal stress and the external stress become larger than the adhesion strength of the coating, it will delaminate. This is possibly the reason why the 10 µm thick BTTi coatings delaminated at 750 °C while the BCZTTi coatings remained attached (section. 4.2), as the sum of the stresses were higher for the BTTi samples due to the difference in internal stress contribution.

Microstructure

SEM images of as-sprayed BTSS, BTTi and BCZTTi samples all showed a dense microstructure without any apparent porosity. The main difference between the two types of coatings is the presence of what seems to be plastic deformation of impacted particles in the BCZT coating as opposed to particle fractures in the BT. Furthermore, largely absent from the BCZT coating is the characteristic craters and ridges often seen in aerosol deposited coatings. These meso-structures have a relatively constant depth and thickness, which is suggested to stem from a "sandblasting" effect as well as the impact/penetration of subsequent powder particles onto previously deposited particles [115]. This is suggested by other works to be determined by the thickness of the coating and the velocity with which the particles impact/penetrate, showing that as the AD coating thickness increases so does the roughness [76]. Since the BCZTTi coatings have a thickness of 4 µm as opposed to the BT samples' 11 µm, this penetration effect seems to be the likely reason for the different morphologies.

Microstructurally, there was very little change in the coatings as a function of temperature for most of the samples. However, this can be explained using a simplified mechanism of solid-state sintering. The driving force behind solid-state sintering is a difference in free energy between the surfaces of adjacent particles and at the point of contact between them. Mass transport between two particles by lattice diffusion from the point of contact to a forming neck region is expressed generally through the following equation [37]:

$$\frac{\Delta L}{L_0} = (\frac{K\gamma a^3 D^* t}{kTd^n})^m \tag{5.4}$$

Where $\frac{\Delta L}{L_0}$ is the linear shrinkage (reduction in distance between the centres of two contacting particles which is equivalent to the sintering rate). K is a geometry dependent constant, γ is the surface energy of the particles, a^3 is the atomic volume of a diffusing vacancy within the particles, D^* is the self diffusion constant for the material, t is time, k is Boltzmann's constant, and T is temperature. The n and m exponents are typically known values close to 3 and in the range of 0.3-0.5 respectively. Lastly d is the diameter of the particles involved which in this model is assumed to be equal. This assumption was made due to the aerosol deposited samples having a narrow particle size distribution as it is important to avoid agglomeration in the fluidized bed before deposition [80].

Conventionally, the sintering rate of a material increases with increasing temperature, although this is not quite obvious from Eq. 5.4. This is because the diffusion coefficient of a material is exponentially linked to the temperature, and is generally well approximated by the Arrhenius equation [37]:

$$D = D_0 \cdot e^{(-\frac{E_a}{RT})} \tag{5.5}$$

Where D is the diffusion coefficient (in $m2/s$), D_0 is the maximal diffusion coefficient (at infinite temperature; in m^2/s), E_a is the activation energy for diffusion (in J/mol), T is the absolute temperature (in K), and R is the universal gas constant, $8.31446 J/(mol \cdot K)$. The following plot (Fig. 5.3a) uses experimental values for the volume diffusion of $BaTiO_3$ taken from Itoh et al. [116]. The resulting diffusion constants can then be plugged into Eq. 5.4 and plotted (Fig. 5.3b) to illustrate how the temperature programs used on BTSS, BTTi and BCZTTi samples are far from optimal based on Siddiqui et.al. [117] who reported that temperatures up to 1350 °C were needed to achieve 96.34% density for $BaTiO_3$ pellets.

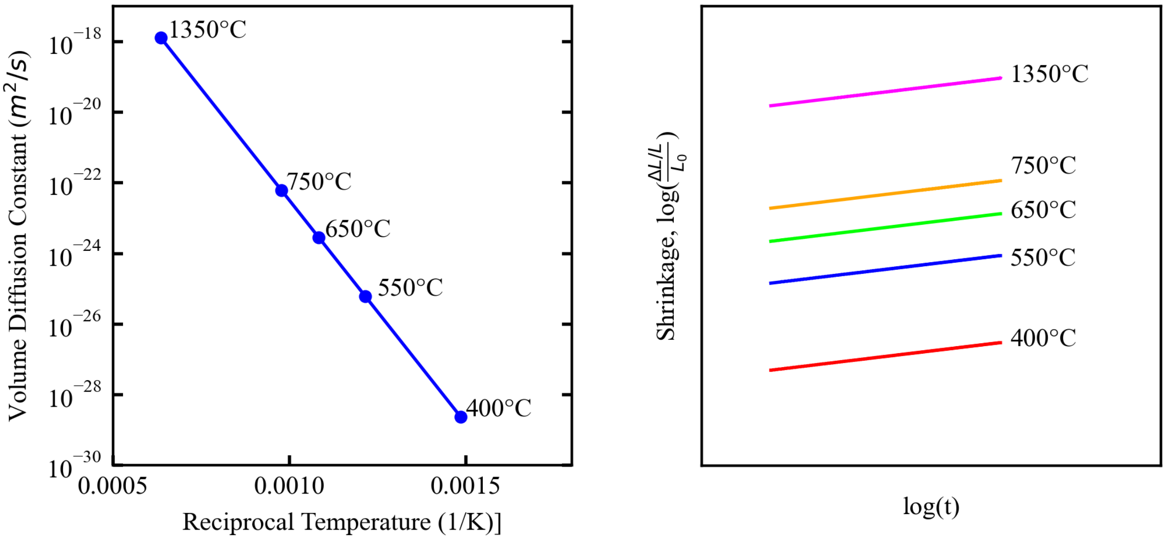

(a) Diffusion coefficient Arrhenius plot

(b) Log-scale sintering rate over time

Figure 5.3: a) Arrhenius plot showing the exponential relation between diffusion coefficient and temperature. b) Theoretical sintering rate as a function of temperature

Considering this, the reproducible grain growth initiated in BTSS samples heat-treated at 750 °C (Fig.4.18b) indicates that there is another contribution to the sintering behavior of the coatings apart from temperature, possibly surface energy. A similar conclusion was reached by Yao et al. who argued that a reduction in the high surface energy of nanosized aerosol deposited particles acted as the driving force for an observed transition from a powder-like $BaTiO_3$ coating made up of individual particles to a bulk-like material [118]. Yao's findings are supported by this thesis in numerous observed effects.

The first is the obvious grain growth in the BTSS samples, which did not extend into the inner coating as seen in Fig. 4.20, as there is a surface energy gradient between particles on the exposed surface and particles within the compacted coating. The second surface effect can be seen on the surface of the BTTi coatings (Fig. 4.22) where higher energy particles on the elevated convex ridges have fused together into flat areas while the concave craters remain largely unchanged. Additionally, the BCZTTi samples which are flatter with little to no cratering displays no observable change in surface morphology (Fig. 4.23). Lastly, the BTSS interface clearly shows individual particles arranged in a lamellar structure in the as-sprayed samples (Fig. 4.19a), but these appear to fuse into a dense bulk-like structure with no discernible grains at 750 °C (Fig. 4.19b).

ToF-SIMS depth profile measurements also seemed to support this as the as-sprayed sample showed clear "dips" in barium and titanium levels at regular intervals throughout the coating (Fig. 4.12). Based on the high resolution of the depth profile, it could be that these dips correspond to small voids in between the lamellar structure or regions of less densely packed particles as seen in Fig. 4.19a. The fact that depth profile for the BTSS sample heat-treated at 750 °C shows no dips further implies the fusing of the voids and lamellar structures into on homogeneous structure (Fig. 4.13 and 4.19b). With all this taken into consideration it seems that there is not enough of a driving force to induce clear grain growth in the bulk coating as seen on the surface, there does seem to be a large enough surface energy contribution between particles for mass transport and fusing to occur.

5.1.3 Mechanical properties

The four representative shapes of the force - displacement curves shown in section 4.3 can be related to four separate microstructural morphologies which will be explained here.

The first curve seen in Fig. 4.28a represents a normal force - displacement curve for an aerosol deposited coating. The curve suggests a dense, compact coating, with few to no defects. This can be explained by the exponential increase in force relative to the increase in displacement. The start of the force-displacement curve roughly has a slope of 1, this is due to an initial compaction of the coating by the indenter. Once the coating is fully compacted, it starts resisting further displacement which gives rise to the steep slope of the curve. This morphology arises from proper fracture of single aerosol deposited particles upon impact with the substrate [68, 119] as a single particle will dissipate its kinetic energy by breaking up its intraparticle bonds (Fig. 5.4a).

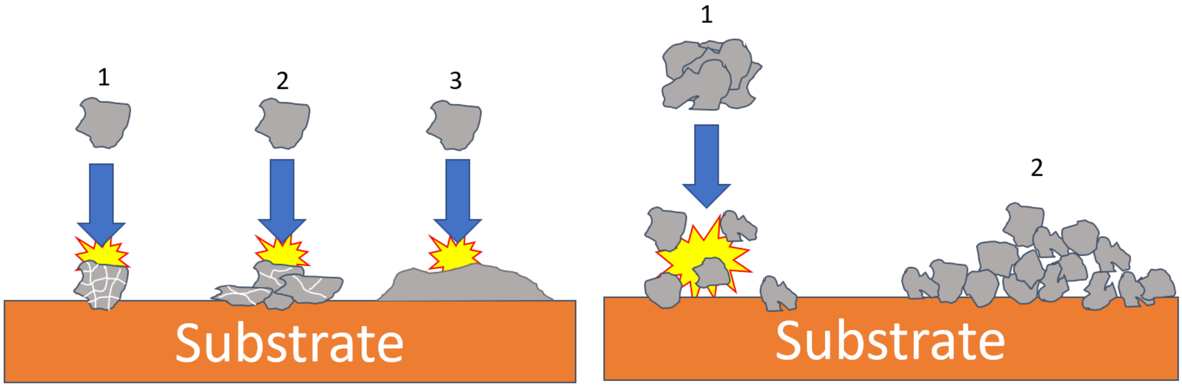

(a) Fracture of single particles

(b) Breaking of agglomerate

Figure 5.4: Diagram showing the fracture behavior of a) single particles and b) agglomerates during aerosol deposition.

Conversely, the curve seen in Fig. 4.28b stems from improper fracture of aerosol deposited particles upon impact [119]. The main reason for this is due to agglomeration of the powders before they are deposited. Specifically, the momentum carried by an agglomeration of particles is dissipated by breaking up the agglomeration rather than fracturing it [68] (Fig. 5.4b) and densifying the coating. This leaves regions of coating which are not properly densified, resulting in a marked effect on the quality of the coatings [80]. Because of this, a considerable effort has been made in order to prevent agglomeration, for instance by using commercial vibrating aerosol generators to created the fluidized bed [120] or separating the carrier and lifting gas inlets [121]. However, due to the high Brownian diffusion of such small particles as the ones used in aerosol deposition, re-agglomeration remains an issue [81].

Once the nano-indenter hits a region containing agglomerates, a low force (relative to a compact region) is required to break it apart. Because of this, the indenter will penetrate deep into this loosely packed region, with less resistance compared to a properly densified coating, resulting in a wide curve with a gentle slope (Fig. 4.28b). Fig. 5.5a shows a diagram of the two first morphologies corresponding to force displacement curves 4.28a and 4.28b.

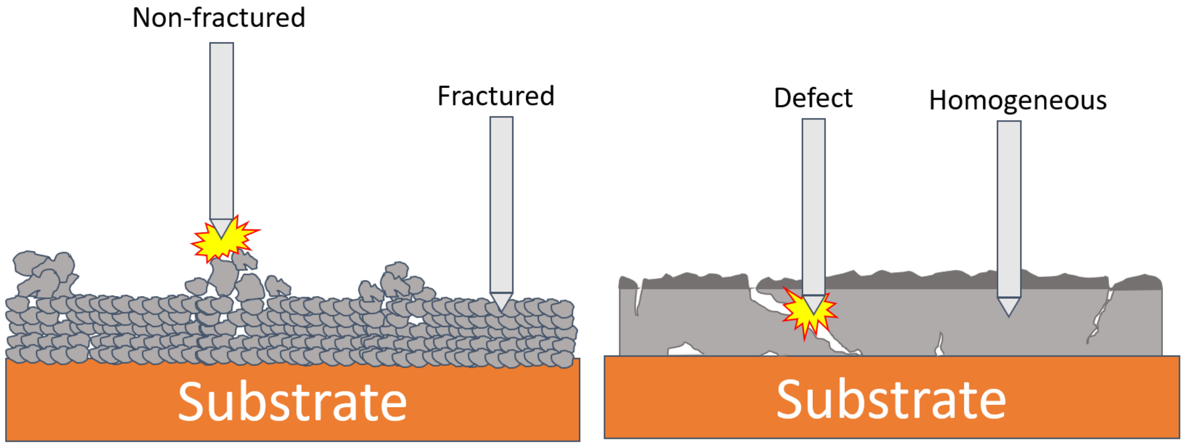

(a) Nano-indentation as-sprayed sample

(b) Nano-indentation heat-treated sample

Figure 5.5: Diagram showing the aerosol deposited coating morphology and how it contributes to variability in nano-indentation measurements: a) poor fracture of agglomerated particles vs single particles, b) large displacements from defects vs small displacements in dense coating.

Heat-treatment, especially for $T \geq 650\,^{\circ}\mathrm{C}$ clearly changed the shape of the force - displacement curves, once again revealing two different trends which can be explained by analysing the microstructural changes. One can clearly see that Fig. 4.28c is very similar to Fig. 4.28a, but it is narrower, has a steeper slope, and does not include an initial slope of 1. This type of curve indicates a successful densification process of the powder-like coating to a bulk-like one. The lack of the initial proportional force - displacement change indicates that the coating can not be further compacted by the indenter, and so the curve rises sharply along the y-axis. The straightness of the curve also indicates that the region being measured is largely homogeneous with little to no differences in the density of the coating in that area.

In contrast, Fig. 4.28d clearly indicates the presence of defects such as cracks and fractures. This can be seen as characteristic "jumps" in displacement relative to the amount of force applied, which physically means that the indenter hits a defect such as a crack or cavity in the material. Once the indenter comes in contact with such a structurally weak region, the indenter might punch through the coating, the coating might collapse in on itself or existing cracks might propagate further, resulting in a large increase in displacement. This effect is illustrated in Fig. 5.5b.

Overall, the measured force - displacement curves align well with the observed microstructural changes in the aerosol deposited coatings. The initial samples have certain powder characteristics but are generally dense and homogeneous with the exception of some areas of improperly compacted coating, likely from agglomerated particles during deposition. The heat-treatment resulted in two main effects: First, the heat treatment introduced more defects into the coatings. These were likely in the form of microcracks from the thermal expansion coefficient mismatch between the substrate and coating as indicated by the SEM measurements in section 4.2. Secondly, the coatings were generally further densified by the heat-treatment as seen in the narrower "normal" curves and corroborated by the various SEM images taken of the interface (Fig. 4.19).

These two temperature dependent changes are also observed in the calculated hardness and reduced modulus values of the samples. Hardness and reduced modulus generally increases with increasing temperature up to 650 °C, indicating that the curves are getting narrower and the coating is densifying. However the values decrease for most samples once they are heat-treated at $T \geq 650\,°\mathrm{C}$.

This indicates that the loss of structural integrity from the introduction of cracks starts outweighing the hardness/reduced modulus contribution from increased density. Furthermore, the variability in the measurement increases dramatically once the samples have been heat-treated, either from the introduction of cracks, or because different regions have varying levels of densification. This can be seen in the different types of curves, and the spacing of curves in the appendix 7.6. Considering optimizing the post-processing parameters, it would seem that mechanical properties are improved for the coatings as long as they are not heated past the point of cracking which can be predicted, as seen in the stress calculations for the BTSS samples in section 5.1.2.

5.1.4 Electrical properties

BTSS samples showed a significant improvement in their electrical properties with increasingly high heat treatments. Before any electrical tests were performed, the change in conductivity between the highly conductive as-sprayed coatings and insulating heat-treated coatings became apparent during SEM measurements. As-sprayed coatings required no additional sputtered carbon on their surfaces in order to not be electrically charged by the SEM electron beam, while the heat-treated samples required increasing amounts of sputtered carbon with increasing heat-treatment temperatures.

Ferroelectric materials such as $BaTiO_3$ exhibit a size effect where the dielectric permittivity of the material is dependent on the grain, particle and crystallite sizes. Several studies have been published reporting such size dependent changes in permittivity for $BaTiO_3$ [122, 123] with the observed effect being that permittivity in $BaTiO_3$ ceramics increases with decreasing grain sizes if the grains are larger than 1 µm, while they increase with increasing grain size if the grain is smaller than 1 µm.

The gradual increase in insulating behavior and polarization seen in the different material systems in this thesis therefore seems to be consistent with the literature. Hatono et al. observed an increase in crystallite size when subjecting aerosol deposited $BaTiO_3$ on 304SUS stainless steel to heat-treatments in the range of 200 °C to 800 °C [124] which was nearly identical to Fig. 4.15b. Hatono reported that crystallite sizes increasing from $\sim$ 10 nm to $\sim$ 20 nm corresponded to a six-fold increase in the measured dielectric constant of the films.

The exact reason why this occurs remains unclear but there are two proposed mechanisms presented by Hosina et al. [91, 122]. The first mechanism suggests that $BaTiO_3$ nanoparticles form a layered structure consisting of a tetragonal ferroelectric core encapsulated by a paraelectric cubic shell with a gradient lattice strain layer between them. Thickness measurements of this cubic shell was consistently reported as 10-15nm regardless of particle size from 20nm to 1000nm [122]. As such, when particle size increases the volume fraction of ferroelectric tetragonal $BaTiO_3$ increasingly outstrips the contribution from the paraelectric cubic shell. Hosina's argument was therefore that the loss of ferroelectric character should occur in $BaTiO_3$ particles below a particle size of 20-30nm because the tetragonal inner phase would disappear. The existence of such a critical size range has been pointed out in older studies as well, observed as a large decrease in the Curie temperature of $BaTiO_3$ below a critical size [125, 126]. As aerosol deposited coatings are similar to a compacted powder in their as-sprayed state, this mechanism could possibly explain the observed change from dielectric to ferroelectric seen in the BTSS samples.

The second mechanism proposed by Hosina was based on freestanding aerosol deposited $BaTiO_3$ films with grain sizes varying from 24 to 170 nm and relative permittivities of 670 and 2800 respectively. This effect was suggested to be due to changes in 90° domain wall densities [91].

For grain sizes over 1 µm, permittivity in $BaTiO_3$ increases with decreasing grain size. It is believed that this is due to contributions from 90° domain walls as decreasing grain size reduces the width of these domains, leading to a higher domain wall density which reportedly enhances dipole and ionic polerizability [127]. However, once particles become smaller than 1 µm one starts losing domains, possibly leading to a transition from a multi-domain structure to a mono-domain one. This potential loss of domain could explain the dielectric behavior seen in the polarization loops in Fig. 4.32.

It is problematic to apply this reasoning to the BTTi and BCZTTi samples, as no ferroelectric hysteresis was observed in either material system. However it should be noted that the limiting factor for these samples during heat-treatment was mechanical stability, which certainly impacted the electric properties. First of all, hysteresis behavior was mainly observed for BTSS samples heat-treated at 750 °C, however no BTTi or BCZTTi samples were suitable for piezotesting after being heated to such a high temperature due to either partial or total delamination of the coating which prevented the measurement of any potential hysteresis behavior which might have developed.

One issue which affected all the material systems was the variability in the maximum electrical field they could withstand without suffering dielectric breakdown, i.e. the dielectric strength. BTSS samples were the most reliable, while the BTTi and BCZTTi systems were much more susceptible to sudden dielectric breakdown. One possible reason for this could be the higher incidence of cracking observed in BTTi and BCZTTi samples compared to BTSS ones. Although insulating silicone oil was used in the piezo-testing, the wetting and penetration of this oil into cracks and defects within the coatings introduced by the heat-treatment might be limited. As such, these defects might contain air which has a dielectric strength of 15-30 kV/cm [128], considerably lower than the observed dielectric strength of the aerosol deposited samples which ranged from 100-500 kV/cm. An increasing number of cracks could therefore offer more alternative paths for current to flow during sufficiently high electrical fields.

High leakage current likely also contributed to this effect, especially in the BCZTTi samples which showed the lowest dielectric strength and the highest amount of leakage. The literature suggests that this might be an effect of the differences in the thickness of the aerosol deposited coatings (10 µm, 11 µm and 4 µm for BTTi, BTSS and BCZTTi respectively) and the hardness of the substrate.

Oh et al. reported that the density of macroscopic defects such as pores, craters and not fully crushed particles decreased with increasing coating thickness over 1 µm [129] and coincided with a reduction in leakage current. This effects was attributed to the hammering-effect mentioned in section 2.5.2. Similarly, it has been reported by Kim et al. [130] that the hardness of the substrate contributes in reducing such defects as harder substrates result in a more complete fracture of the aerosol deposited particles on impact, increasing particle to particle bonding and reducing leakage current. Lastly, it has been suggested that the intrinsic mechanism for high leakage currents in aerosol deposited $BaTiO_3$ is caused by the presence of oxygen vacancies which act as detrimental charge carriers under sufficiently high electric fields [131].

The exact reason for the anisotropic behavior observed in the Berlincourtmeter measurements (Fig. 4.36) i.e. that the magnitude of the response was lower when the coating was facing down is not entirely clear. However, likely reasons include that the electrodes on either side of the sample (steel substrate and thin layer of painted-on silver) are quite different, both in thickness and coverage. The steel substrate covers the entire area of the coating, while the silver electrode only encompasses a small "dot" in the middle of the coating. Furthermore as seen in the nanoindentation measurements (section 4.3) the heat-treatment introduced inhomogeneities in the coating, which could have affected the measurement.

5.2 Soaking

The initial goal of the soaking study was to ascertain the stability, and ability of aerosol deposited $BaTiO_3$ to induce calcium phosphate nucleation on its surface in SBF. This is generally accepted as a good indicator of a biomaterial's efficacy in hard-tissue applications such as bone replacement materials [29].

The general mechanism for how piezoelectric biomaterials enhance the initial mineralization steps of bone, is well understood and outlined in section 2.3. However, even though a considerable amount of work has been done to establish the enhancement of bone mineralization on poled versus unpoled piezoelectric material surfaces [132, 133], the critical/threshold surface charge value needed to induce this effect has not been as extensively researched.

It was therefore unclear whether a large or small amount of surface charge was needed to achieve the desired efficacy, which could have large implications for the choice of material used in applications where bone mineralization is the desired outcome. For instance, it could open up the possibility of using a wider range of materials with different electrical properties. BTSS samples heat-treated at 750 °C were therefore chosen as the test samples for the SBF study, as they displayed a roughly linear increase in d_{33} with increasing poling times which indicates a linear increase in the surface charge development with poling time.

This gradient would in theory help identify a potential poling threshold value for enhanced calcium phosphate nucleation on the surface which would be measured as the percentage mass gain for each sample depending on poling and soaking time. Additionally, the 750 °C BTSS samples were the only samples to show clear ferroelectric hysteresis loops and the least amount of leakage current (Fig. 4.32), indicating that they would be able to retain their remnant polarization for longer than any other heat-treated sample. This was naturally vital as the SBF study was conducted over the course of 7 days.

Counter to the initial assumptions before soaking, the BTSS samples were not stable in SBF as outlined in section 4.5. Due to issues with relevant instruments such as ICP-MS on campus, it was not possible to quantitatively test important parameters such as SBF ion concentrations before and after soaking. Because of this, the soaking study was highly qualitative and it is therefore difficult to describe what is occurring during soaking without falling into speculation, as there are so many unknown factors involved. Therefore, this section presents a possible explanation for the observed behavior of heat-treated, poled aerosol deposited BTSS samples in SBF, but note that further testing is needed to fully understand the true mechanism of the coating breakdown.

There are four identified parameters in the soaking study which appears to have an effect on the breakdown of the BTSS samples and calcium phosphate nucleation. These are: soaking time, degree of poling/poling time, structural damage before soaking and coating morphology.

5.2.1 Damage and dissolution of the coating

The parameters can be related back to the dissolution behavior of $BaTiO_3$. Perovskites are in general not thermodynamically stable in aqueous solutions [38, 134] and especially not in acidic conditions. This difference was made clear by the fact that an upoled BTSS sample heat-treated at 750 °C remained remained largely undamaged after soaking in water for 7 days at 36.5 °C. In the case of $BaTiO_3$ the increased dissolution can be explained by substantial leaching of Ba^{2+} ions into solution with decreasing pH. In fact, it has been reported that barium can leach so substantially from $BaTiO_3$ in aqueous solutions that a TiO_2 surface layer can be formed instead [38, 135]. This dissolution mechanism is explained by the following pH dependent reaction equations in acidic solution [136]:

$$\mathrm{BaTiO_3(s) + 2\,H^+(aq) \rightleftharpoons Ba^{2+}(aq) + TiO_2(s) + H_2O(aq)} \tag{5.6}$$

$$k_1[BaTiO_3][H^+]^2 = k_{-1}[Ba^{2+}][TiO_2][H_2O] \tag{5.7}$$

Where k_1 and k_{-1} denotes the rate constants of the forward and reverse reactions respectively and the species in brackets are concentrations of said species. This reaction is self-limiting according to the literature, as the dissolved Ba^{2+} combines with CO_2 present in the solution and redeposits $BaCO_3$ onto the surface which hinders further leaching of Ba^{2+} [136] (equation 5.8 and 5.9). The CO_2 content of the solution likely stems from two main sources. First, CO_2 is naturally present in the solution due to the partial pressure of CO_2 in the air which leads to an equilibrium of dissolved CO_2. The second source stems from all $BaTiO_3$ powders made by conventional solid-state reactions having some unreacted $BaCO_3$ precursor in them, especially if the calcination of the precursors is not complete [135, 137–139].

$$Ba^{2+} + CO_2 + H_2O \rightleftharpoons BaCO_3 + 2\,H^+ \tag{5.8}$$

$$2\,H^+ + CO_3{}^{2-} + BaTiO_3 \rightleftharpoons BaCO_3 + TiO_2 + H_2O \tag{5.9}$$

Due to the seemingly complete dissolution of the coating one can assume that in the case of the BTSS aerosol deposited samples, the $BaCO_3$ side-reaction does not contribute substantially to the stability of the coating. However, the reaction helps explain why other studies have not observed such a thorough dissolution of the $BaTiO_3$ as in the current soaking study. Combined with the apparent absence of the inhibiting $BaCO_3$ reaction, and the fact that the coating was completely dissolved in some samples, one can assume that the forward reaction is far more favored than the reverse reaction ($k_1 >>> k_{-1}$). In addition, there are other observed reactions which promote the dissolution of $BaTiO_3$, i.e. the precipitation of $BaSO_4$ (Fig. 4.40) which removes Ba^{2+} from the solution, and further skews the equilibrium towards the formation of products as stipulated by Le Chatelier's principle. Because of this, one can make a rate expression based only on the forward reaction. This results in equation. 5.10 which shows that the reaction is largely dependent on the concentrations of $[BaTiO_3]$ and $[H^+]$. Furthermore, the dissolution of $BaTiO_3$ has to be a surface reaction, as the diffusion of $BaTiO_3$ from the bulk coating towards the surface is exceedingly slow at 36.5 °C [140]. This means that local reactant concentrations at the solid-liquid interface determine the rate, not the total concentrations within the system.

$$r = k_1[BaTiO_3][H^+]^2 \tag{5.10}$$

The $BaTiO_3$ available to the reaction is directly linked to the coating microstructure. Specifically, the $BaTiO_3$ surface area available to the solution determines the concentration of $BaTiO_3$ in the rate expression, increasing the driving force of the reaction. It is a well established fact that nano-sized structures have a relative surface area which is up to seven orders of magnitude higher than their bulk counterparts [14]. As such the grain and crystallite size of the coating likely has an impact on the dissolution behavior. Chiang and Jean [141] observed enhanced Ba^{2+} leaching in particles smaller than 1.5 µm and it has been reported that thermodynamical parameters for particle dissolution change as well. Li et al. [142] reported that as the size of copper nano-particles decreased, the standard molar dissolution Gibbs energy, the standard molar dissolution enthalpy and the standard molar dissolution entropy decreased as well while the dissolution constant increased. As such, it would seem that the small crystallite sizes calculated for the aerosol deposited coatings (Fig. 4.15b) enhanced their subsequent dissolution in the SBF. The presence of cracking and defects in the coatings also seems to support this as it would also expose larger areas of the coating to the solution.

The proton concentration on the other hand is likely determined by the electrical properties of the coating in the form of the surface charge magnitude and the formation an electrical double layer [26]. As previously mentioned in section 2.3, the mechanism for enhanced bone mineraliztion by piezoelectrics involve the attraction of positive Ca^{2+} ions to the negatively charged surface. However, there is far less Ca^{2+} than H^+ in the prepared SBF (based on the amounts of HCl added) and the literature states that the electric double layer surrounding a negative surface charge leads to the attraction of cations to the interface relative to their concentration in the bulk solution [143]. This can be explained by the Boltzmann equation [144].

$$c_i(x) = c_{b,i} exp\left[-\frac{w_i(x)}{RT}\right] \tag{5.11}$$

Where $c_i(x)$ is the concentration of a given ionic species at distance x from the charged surface. $c_{b,i}$ is the concentration of that species in the bulk solution i.e. the total concentration. ϕ_x is the potential as distance x from the charged surface (with respect to the bulk which has a potential of zero), this potential increases with increasing net surface charge magnitude. $z_i F \phi_x$ and RT are the electrostatic and thermal energy contributions respectively, with z_i being the charge of the ion, F is Faraday's constant, is the ideal gas constant and T is absolute temperature.

One can therefore see that as the poling time increases and subsequently the surface charge magnitude, the BTSS sample will have an increased affect on the diffusion of positive ions to its surface. As the concentration of H^+ is much higher than that of Ca^{2+}, it is likely that the solid-liquid interface is largely populated by hydronium ions and not calcium. This means that the local pH at the interface is potentially lower than that of the buffered bulk which increases the rate of the surface dissolution reaction. This could explain why the BTSS coating damage and dissolution increases with increasing poling time (Fig. 4.38, 4.37). Lastly, one should note that the damage increased with soaking time, which is likely an effect of the aforementioned reactions having longer time to propagate and dissolve the coating.

5.2.2 Calcium phosphate nucleation

Based on the proposed mechanism for the dissolution of the coating seen in section 5.2.1, it explains why calcium phosphate was mainly found on the surface of the substrate, as the coating is not stable. Furthermore, the small amount of calcium phosphate nucleation can be explained by the lack of any electrical interaction enhancing the nucleation, as the substrate does not process a surface charge. It is therefore likely that the substrate follows a classical heterogeneous nucleation mechanism. The general equation for the formation of of calcium phosphate in SBF is as follows [145]:

$$\mathrm{Ca^{2+} + HPO_4{}^{2-} \rightleftharpoons CaHPO_4} \tag{5.12}$$

Where the equilibrium constant of the reaction has a reported value of $6.81x10^2$ [146] and is defined as:

$$\frac{[\mathrm{CaHPO_4}]}{[\mathrm{Ca^{2+}}][\mathrm{HPO_4{}^{2-}}]} = \mathrm{K} \tag{5.13}$$

The thermodynamic driving force for this precipitation reaction is based on the free energy change equation for a supersaturated solution [147]:

$$\Delta G = -\frac{RT}{n} ln(S) = -\frac{RT}{n} ln(A_p/K_{sp}) \tag{5.14}$$

Where ΔG is the Gibbs energy per mole for the calcium phosphate forming ions, R is the ideal gas constant, T is the absolute temperature, n is the number of ions making up a calcium phosphate molecule and S is the supersaturation as defined by the activity and solubility of the product, given as A_p and K_{sp} respectively.

From these equations one can estimate the kinetics i.e. the rate (J) for the formation of the spherical calcium phosphate particles observed in this soaking study [14]:

$$J = Kexp\left(-\frac{\Delta G}{kT}\right) = Kexp\left(-\frac{16\pi v^2\gamma^3 f(\Theta)}{3k^3T^3(ln\ S)^2}\right) \tag{5.15}$$

Where k is Boltzmann's constant, $16\pi/3$ is the geometric factor for a spherical particle, υ is the volume of said particle, $f(\Theta)$ is the contact angle function and γ is the surface energy. One can see that the rate of calcium phosphate is proportional to the equilibrium constant (K) of the reaction and exponentially dependent on the activation energy associated with precipitation (ΔG). The equilibrium constant has already been defined as being dependent on the concentrations of the various ions in the SBF, however the activation energy for nucleation on the substrate is largely determined by the surface energy as the contact angle can be estimated as being 90° [145] based on the appearance of the calcium phosphate globules on the substrate surface (Fig. 4.39). The stainless steel substrates used in this thesis have been extensively polished before the aerosol deposition. In other words they have a low surface roughness and a reduced, flat surface area. As a result, the surface energy of the substrate can be assumed to be low, meaning that it is not a very favorable surface for the calcium phosphate to nucleate on, reducing the rate. This is likely the reason why only small amounts of calcium phosphate was observed.

5.2.3 Other precipitates

Precipitation of other species such as the observed barium sulfate crystals (Fig. 4.40b-c) follows the same thermodynamic principles as the precipitation of calcium phosphate given by equation 5.15 albeit with a different equilibrium constant. This constant has been reported in the literature as 0.36977229 in aqueous systems [148]. One would therefore not expect to find many barium sulfate crystals on the sample surface relative to calcium phosphate globules which has a much higher equilibrium constant and concentration of its composite ions than barium sulfate.

As such, one would only get substantial amounts of barium sulfate on the sample surfaces if the concentration of Ba^{2+} in solution is high enough to favor enhanced formation of barium sulfate from leached Ba^{2+} and $SO_4{}^{2-}$ in the SBF. One should note that the presence of precipitates other than calcium phosphate was actively counteracted by the experimental procedure. In order to accurately measure mass gain from calcium phosphate nucleation, other precipitates had to be removed. Samples were therefore rinsed using DI water in order to wash away common surface precipitates such as NaCl which would have skewed the measurement. This likely washed away most of the potential barium sulfate as well as it, like NaCl mainly exist as loosely adhered crystals on the sample surface. Calcium phosphates on the other hand formed films on the substrate which have been suggested to be able to chemically bond with the chromium oxide passivation layer [149], improving adhesion and allowing them to remain attached. As such, it is difficult to describe the parameters leading to barium sulfate precipitation as apart from the likely high concentration of Ba^{2+}, not much is known.

6 Conclusion

In this work, nano-grained aerosol deposited $BaTiO_3$ coatings were successfully heat-treated over a wide temperature range and characterized. The thesis showed that it was possible to change the microstructure of aerosol deposited samples and improve mechanical and electrical properties as a result.

It can be concluded that 750 °C is the optimal heat-treatment temperature for $BaTiO_3$ coatings deposited onto 304SUS stainless steel based on the emergence of ferroelectric properties as a result of induced microstructural changes, conservation of adhesion and mechanical integrity. It is recommended that the samples are not heat-treated at temperatures above or below this range, as lower temperatures do not markedly change the sample properties and higher temperatures lead to sample destruction. Furthermore, it has been found that the combination of coating and substrate materials determines the optimal heat-treatment temperature range. Samples comprised of $BaTiO_3$ and calcium/zirconium doped $BaTiO_3$ on Ti6Al4V alloy showed that thermal expansion mismatch between the coating and the substrate lead to the degradation of coatings' mechanical integrity after being heat-treated past a maximum temperature of 650 °C.

Investigation into the appearance of new chemical phases within the coatings revealed that the heat-treatment range utilized in this thesis was not high enough to induce clear chemical change in most samples, with the exception of some minor products in coatings deposited on stainless steel. This is based on the absence of new XRD diffraction peaks after heat-treatment as well as the lack of changes in EDS maps and ToF-SIMS depth profiles. The minor products which do form are hypothesized to stem from the diffusion of certain alloying elements from the substrate into the coatings or from the oxidation of the substrates and from contaminants present on the substrates before deposition was carried out.

Microstrucural measurements by SEM showed a clear correlation between the heat-treatment temperature and the loss of mechanical integrity in the samples as a result of cracking and delamination. This has been attributed to thermally induced stress at the coating-substrate interface by thermal expansion mismatch between the materials. SEM imaging also confirmed the presence of mass-transport during heat-treatment with the degree of mass transport being determined by the heat-treatment temperature. This was supported by diffraction peak analysis which a steady increase in crystallite size with increasing temperature. As the electrical properties of the coating materials is heavily dependent on crystallite size, it is possible to tune the electrical properties of aerosol deposited coatings using temperature. Diffraction peak analysis also showed a reduction of residual stress within the coating after heat-treatment.

Mechanical testing showed an increase in the hardness and the reduced modulus of heat-treated samples due to the initiation of mass transport and subsequent densification, this changed the coating from a powder-like compact to more of a bulk ceramic. However, it also revealed a decrease in coating mechanical integrity due to the introduction of defects and inhomogeneities.

Electrical properties saw a clear improvement after heat-treatment, with enhanced dielectric properties observed in all samples after heat-treatment. This was attributed to the growth of coating crystallites, however the electric properties starts degrading with the introduction of enough defects from the heat-treatment.

Finally, the soaking study showed that aerosol deposited $BaTiO_3$ is likely not suitable for biomedical hard-tissue applications. This was due to the rapid dissolution and destruction of the coating in SBF and the apparent lack of calcium phosphate nucleation on its surface with increasing coating surface charge. It is hypothesized that the dissolution behavior is enhanced by the high surface area of the nano-grained coating as well as electrostatic attraction of acidic ions to the coating surface. As such, the $BaTiO_3$ coating was bioactive but did not offer any constructive functionalization to the metal implant material. An argument could be made for aerosol deposited $BaTiO_3$ potentially having efficacy as a bioresorbable (i.e. biodegradable) material due to it being so soluble in SBF. However, bioresorbable ceramics such as bioglass are not simply removed from the implant surface by dissolution like the $BaTiO_3$ was but rather exchanges its material with the surrounding medium as it dissolves. Specifically, bioglass follows an ion exchange mechanism where it exchanges Na^+ and Ca^{2+} for H^+ from surrounding solution. This forms functional Si-OH groups and a Na^+ and Ca^{2+} depleted surface layer which allows for the formation of a covalently bonded calcium phosphate layer [150, 151]. As the dissolution of $BaTiO_3$ largely left a clean substrate with only a few spots of calcium phosphate directly on the metal, one can assume that the $BaTiO_3$ does not possess beneficial bioresorbable properties. However, it was found that aerosol deposited $BaTiO_3$ was comparatively stable in water based on the lack of dissolution after seven days in a control sample. This could mean that aerosol deposited $BaTiO_3$ could be suitable for other non-biomedical applications which involve the presence of moisture.

In total, the aerosol deposition method does not appear to be a suitable way of producing bioactive implant coatings. The deposition process creates nano-sized crystallites which reduce the electrical properties which are desired for in-vivo functionality and the heat-treatments required to improve electrical properties degrade structural integrity which is needed to survive in-vivo. However, more work needs to be done before a clear conclusion can be drawn as several parameters involved in the soaking study remains unexplored.

7 Further work

As the coating-substrate thermal expansion coefficient mismatch is believed to be the dominant contributor to stress development during heat-treatment, this effect should be further investigated quantitatively. An example could be develop a more accurate predictive stress model based on heat-treating additional material combinations with higher or lower thermal expansion mismatches than the ones seen in this thesis. This could potentially help explain the stress contribution from thermal expansion mismatch and identify optimal coating-substrate material combinations. In turn this would help ensure the mechanical integrity of heat-treated samples in the future and potentially explore whether or not stress is reintroduced into the samples after heat-treatments at sufficiently high temperatures, as hypothesized in this thesis.

The effect of holding time was not explored in this thesis as all heat-treatments utilized a holding time of two hours. Therefore, future studies could evaluate the effect of increased/decreased holding times of the observed mass transport within the coatings. Furthermore, all samples were heat-treated in air and as a clear oxidation layer was found on the Ti6Al4V substrate after the delimination of $BaTiO_3$. It is uncertain to which degree this reaction affects sample integrity, and as such subsequent work could be focused on heat-treating the different samples in other atmospheres such as pure N_2 gas.

Due to issues with the instrument it was not possible to quantitatively measure the changing ion concentrations of the SBF during the soaking study. As such the kinetics behind the dissolution of the $BaTiO_3$ coating remains unexplored. This has important implications when determining the root cause behind the enhanced dissolution behavior and for predicting the stability and lifetime of aerosol deposited coatings in vivo. Therefore, future studies should include observations on how the SBF concentrations change during the soaking study and a kinetic model should be produced in order to help predict this behavior. In addition it is not clear how important each of hypothesized factors which increased dissolution are in relation to eachother. Simulations such as Density-functional theory (DFT) could therefore be a valuable tool in future studies in order to better understand the contribution of different surface properties to the dissolution behavior.

References

[1] Kara Kamen Poon. *Doctoral thesis Development of Piezoelectric BCZT Ceramics as Electroactive Bone Implant Materials Kara Kamen Poon Development of Piezoelectric BCZT Ceramics as Electroactive Bone Implant Thesis for the Degree of Philosophiae Doctor*, volume 9. 2020.

[2] Ti 950 triboindenter user manual. Technical report, 2014.

[3] Yang Peng, Jiang Chu, and Jun Dong. Compressive behavior and constitutive model of austenitic stainless steel s30403 in high strain range. *Materials*, 11:1023, 06 2018.

[4] D. Hanft, J. Exner, M. Schubert, T. Stöcker, P. Fuierer, and R. Moos. An overview of the aerosol deposition method: Process fundamentals and new trends in materials applications. *Journal of Ceramic Science and Technology*, 6:147–181, 9 2015.

[5] D.R. Steinberg and M.E. Steinberg. The early history of arthroplasty in the united states. *Clinical Orthopaedics and Related Research*, (374):55–89, 2000.

[6] John Charnley. Anthroplasty of the hip: A new operation. *The Lancet*, 277(7187):1129–1132, 1961. Originally published as Volume 1, Issue 7187.

[7] J. Charnley, A. Kamangar, and M.D. Longfield. The optimum size of prosthetic heads in relation to the wear of plastic sockets in total replacement of the hip. *Medical Biological Engineering*, 7(1):31–39, 1969.

[8] J.A. Vetalice. Orthopaedic industry annual report-focus on joint replacement. *Ortho-Know*, (JUNE):1–8, 2012.

[9] Monika Saini. Implant biomaterials: A comprehensive review. *World Journal of Clinical Cases*, 3(1):52, 2015.

[10] B.J. McEntire, B.S. Bal, M.N. Rahaman, J. Chevalier, and G. Pezzotti. Ceramics and ceramic coatings in orthopaedics. *Journal of the European Ceramic Society*, 35(16):4327–4369, 2015.

[11] Bongio Matilde, Jeroen van den Beucken, Sander Leeuwenburgh, and John Jansen. Development of bone substitute materials: From 'biocompatible' to 'instructive'. *J. Mater. Chem.*, 20:8747–8759, 10 2010.

[12] Dietmar Werner Hutmacher, Jan Thorsten Schantz, Christopher Xu Fu Lam, Kim Cheng Tan, and Thiam Chye Lim. State of the art and future directions of scaffold-based bone engineering from a biomaterials perspective. *Journal of Tissue Engineering and Regenerative Medicine*, 1(4):245–260, 2007.

[13] E. Sukur, Y. Akman, Y. Ozturkmen, and F. Kucukdurmaz. Particle disease: A current review of the biological mechanisms in periprosthetic osteolysis after hip arthroplasty. *The Open Orthopaedics Journal*, 10:241 – 251, 2016.

[14] Guozhong Cao and Ying Wang. *Nanostructures and Nanomaterials*. WORLD SCIENTIFIC, 2nd edition, 2011.

[15] I. Simsek and D. Ozyurek. Investigation of the electrochemical corrosion properties of high-energy milled ti6al4v alloy in simulated body fluid environment. *Powder Metallurgy*, 62(3):169–175, 2019.

[16] Qizhi Chen and George A. Thouas. Metallic implant biomaterials. *Materials Science and Engineering: R: Reports*, 87:1 – 57, 2015.

[17] F. R. Baxter, C. R. Bowen, I. G. Turner, and A. C.E. Dent. Electrically active bioceramics: A review of interfacial responses. *Annals of Biomedical Engineering*, 38(6):2079–2092, 2010.

[18] J. M. Herbert A. J. Moulson. *Elementary Solid State Science*, chapter 2, pages 5–93. John Wiley Sons, Ltd, 2003.

[19] Dragan Damjanovic. Ferroelectric, dielectric and piezoelectric properties of ferroelectric thin films and ceramics - abstract - reports on progress in physics. *Reports on Progress in Physics*, 61(dc):1267, 1998.

[20] R. J. D. Tilley. *Understanding solids : the science of materials*. Wiley, John Wiley Sons Inc., Chichester, West Sussex, United Kingdom, 2nd edition. edition, 2013.

[21] Kefeng Wang, Changchun Zhou, Youliang Hong, and Xingdong Zhang. A review of protein adsorption on bioceramics. *Interface Focus*, 2(3):259–277, 2012.

[22] Eiichi Fukada and Iwao Yasuda. On the piezoelectric effect of bone. *Journal of the Physical Society of Japan*, 12(10):1158–1162, 1957.

[23] Laurent Maïmoun and Charles Sultan. Effects of physical activity on bone remodeling. *Metabolism*, 60(3):373–388, 2011.

[24] Eduardo Cadore, Michel Brentano, and Luiz Kruel. Effects of the physical activity on the bone mineral density and bone remodelation. *Revista Brasileira de Medicina do Esporte*, 11:373–379, 12 2005.

[25] J. Joana and J. Silva. The effect of high- and low-impact physical activity on bone mineral density: A literature review. *Annals of Physical and Rehabilitation Medicine*, 61:e401,

2018. 12th World Congress of the International Society of Physical and Rehabilitation Medicine. Paris. 8-12 July 2018.

[26] Syed A.M. Tofail and Joanna Bauer. Electrically Polarized Biomaterials. *Advanced Materials*, 28(27):5470–5484, 2016.

[27] P. Vaněk, Z. Kolská, T. Luxbacher, J. A.L. García, M. Lehocký, M. Vandrovcová, L. Bačáková, and J. Petzelt. Electrical activity of ferroelectric biomaterials and its effects on the adhesion, growth and enzymatic activity of human osteoblast-like cells. *Journal of Physics D: Applied Physics*, 49(17), 2016.

[28] Tadashi Kokubo and Hiroaki Takadama. How useful is SBF in predicting in vivo bone bioactivity? *Biomaterials*, 27(15):2907–2915, 2006.

[29] Francesco Baino and Seiji Yamaguchi. The use of simulated body fluid (SBF) for assessing materials bioactivity in the context of tissue engineering: Review and challenges. *Biomimetics*, 5(4):1–19, 2020.

[30] Hans Thurnauer and James Deaderick. Insulating materials, Oct 1947.

[31] A. von Hippel. Ferroelectricity, domain structure, and phase transitions of barium titanate. *Rev. Mod. Phys.*, 22:221–237, Jul 1950.

[32] M. Acosta, N. Novak, V. Rojas, S. Patel, R. Vaish, J. Koruza, G. A. Rossetti, and J. Rödel. BaTiO3-based piezoelectrics: Fundamentals, current status, and perspectives, dec 2017.

[33] Wook Jo, Klaus T P Seifert, Eva-maria Anton, and Torsten Granzow. Perspective on the Development of Lead-free Piezoceramics. 1177:1153–1177, 2009.

[34] Yeong-Joon Park, Kyu-Seog Hwang, Jong-Eun Song, Joo L Ong, and H [Ralph Rawls]. Growth of calcium phosphate on poling treated ferroelectric batio3 ceramics. *Biomaterials*, 23(18):3859 – 3864, 2002.

[35] Kyu-Seog Hwang, J Song, J Jo, H Yang, Yeong-Joon Park, Joo Ong, and Henry Rawls. Effect of poling conditions on growth of calcium phosphate crystal in ferroelectric batio3 ceramics. *Journal of materials science. Materials in medicine*, 13:133–8, 02 2002.

[36] Nurul Huda Yusoff, Rozana Aina Maulat Osman, Mohd Sobri Idris, Ku Noor Dhaniah Ku Muhsen, and Nurul Izza Mohd Nor. Dielectric and structural analysis of hexagonal and tetragonal phase batio3. *AIP Conference Proceedings*, 2203(1):020038, 2020.

[37] David W. Richerson and William E. Lee. *Modern ceramic engineering: properties, processing, and use in design*. CRC Press, 2018.

[38] H. Wayne Nesbitt, G. Michael Bancroft, William S. Fyfe, Suresh N. Karkhanis, Akio

Nishijima, and Shigemitsu Shin. Thermodynamic stability and kinetics of perovskite dissolution. *Nature*, 289(5796):358–362, 1981.

[39] Tomasz Trzepiecinski and Magdalena Gromada. Characterization of mechanical properties of barium titanate ceramics with different grain sizes. *Materials Science- Poland*, 36(1):151–156, 2018.

[40] J. R. Davis. *Handbook of materials for medical devices*. ASM International, 2006.

[41] Properties: Stainless steel - grade 304 (uns s30400), Jun 2021.

[42] Jorge Alvarado, Ricardo Maldonado, Jorge Marxuach, and Rubén Otero. Biomechanics of hip and knee prostheses. 2006.

[43] M Navarro, A Michiardi, O Castaño, and J.A Planell. Biomaterials in orthopaedics. *Journal of The Royal Society Interface*, 5(27):1137–1158, 2008.

[44] E. Rudolf. A review of findings on chromium toxicity [prehled poznatků o toxicite chromu.]. *Acta medica (Hradec Králové). Supplementum Universitas Carolina, Facultas Medica Hradec Králové*, 41(1):55–65, 1998.

[45] D.G. Barceloux. Chromium. *Journal of Toxicology - Clinical Toxicology*, 37(2):173–194, 1999.

[46] Bethany R. McBride, Jonathon Lieschke, Adam Berlie, David L. Cortie, Helen Y. Playford, Teng Lu, Narendirakumar Narayanan, Ray L. Withers, Dehong Yu, and Yun Liu. Study of the b-site ion behaviour in the multiferroic perovskite bismuth iron chromium oxide. *Journal of Applied Physics*, 123(15):154104, 2018.

[47] Alexandra Muñoz and Max Costa. Elucidating the mechanisms of nickel compound uptake: A review of particulate and nano-nickel endocytosis and toxicity. *Toxicology and Applied Pharmacology*, 260(1):1–16, 2012.

[48] Jinshun Zhao, Xianglin Shi, Vincent Castranova, and Min Ding. Occupational toxicology of nickel and nickel compounds. *Journal of Environmental Pathology, Toxicology and Oncology*, 28(3):177–208, 2009.

[49] M. Bergman, B. Bergman, and R. Söremark. Tissue accumulation of nickel released due to electrochemical corrosion of non-precious dental casting alloys. *Journal of Oral Rehabilitation*, 7(4):325–330, 1980.

[50] Maria P. Abbracchio, J. Simmons-Hansen, and Max Costa. Cytoplasmic dissolution of phagocytized crystalline nickel sulfide particles: A prerequisite for nuclear uptake of

nickel. *Journal of Toxicology and Environmental Health*, 9(4):663–676, 1982. PMID: 7108981.

[51] M.P. Abbracchio, R.M. Evans, J.D. Heck, O. Cantoni, and M. Costa. The regulation of ionic nickel uptake and cytotoxicity by specific amino acids and serum components. *Biological Trace Element Research*, 4(4):289–301, 1982.

[52] Karthika Prasad, Olha Bazaka, Ming Chua, Madison Rochford, Liam Fedrick, Jordan Spoor, Richard Symes, Marcus Tieppo, Cameron Collins, Alex Cao, David Markwell, Kostya Ostrikov, and Kateryna Bazaka. Metallic biomaterials: Current challenges and opportunities. *Materials*, 10:884, 07 2017.

[53] Mitsuo Niinomi. Recent metallic materials for biomedical applications. *Metallurgical and Materials Transactions A*, 33:477–486, 03 2002.

[54] M. Niinomi. Biologically and mechanically biocompatible titanium alloys. *Materials Transactions*, 49(10):2170–2178, 2008.

[55] N. Moritz, E. Vedel, H. Ylänen, M. Jokinen, M. Hupa, and A. Yli-Urpo. Characterisation of bioactive glass coatings on titanium substrates produced using a co 2 laser. *Journal of Materials Science: Materials in Medicine*, 15(7):787–794, 2004.

[56] CS Chien, CW Liu, TY Kuo, CC Wu, and TF Hong. Bioactivity of fluorapatite/alumina composite coatings deposited on ti6al4v substrates by laser cladding. *Applied Physics A*, 122(4):303, 2016.

[57] Erfan Zalnezhad, S. Baradaran, Abdul Razak Bushroa, and Ahmed Sarhan. Mechanical property enhancement of ti-6al-4v by multilayer thin solid film ti/tio2 nanotubular array coating for biomedical application. *Metallurgical and Materials Transactions A*, 45A, 01 2014.

[58] B.P. Bannon and E.E. Mild. Titanium alloys for biomaterial application: An overview. pages 7–15, 1983.

[59] Abhijit Chandra, Jae Joong Ryu, P Karra, Pranav Shrotriya, Viggo Tvergaard, M Gaisser, and T Weik. Life expectancy of modular ti6al4v hip implants: Influence of stress and environment. *Journal of the mechanical behavior of biomedical materials*, 4:1990–2001, 11 2011.

[60] Xiang Li, Chengtao Wang, Wenguang Zhang, and Yuanchao Li. Fabrication and characterization of porous ti6al4v parts for biomedical applications using electron beam melting process. *Materials Letters*, 63(3):403–405, 2009.

[61] Q.Z Chen, C.T Wong, W.W Lu, K.M.C Cheung, J.C.Y Leong, and K.D.K Luk. Strength-

ening mechanisms of bone bonding to crystalline hydroxyapatite in vivo. *Biomaterials*, 25(18):4243 – 4254, 2004.

[62] L. L. Hench, R. J. Splinter, W. C. Allen, and T. K. Greenlee. Bonding mechanisms at the interface of ceramic prosthetic materials. *Journal of Biomedical Materials Research*, 5(6):117–141, 1971.

[63] L. L. Hench and H. A. Paschall. Direct chemical bond of bioactive glass-ceramic materials to bone and muscle. *Journal of Biomedical Materials Research*, 7(3):25–42, 1973.

[64] Properties: Titanium alloys - ti6al4v grade 5, Jun 2021.

[65] Carlos Oldani and Alejandro Dominguez. Titanium as a biomaterial for implants. In Samo K. Fokter, editor, *Recent Advances in Arthroplasty*, chapter 9. IntechOpen, Rijeka, 2012.

[66] Jun Akedo, Noriaki Minami, Kouji Fukuda, Masaaki Ichiki, and Ryutaro Maeda. Electrical properties of direct deposited piezoelectric thick film formed by gas deposition method annealing effect of the deposited films. *Ferroelectrics*, 231(1):285–292, 1999.

[67] Jun Akedo and Maxim Lebedev. Microstructure and electrical properties of lead zirconate titanate (pb(zr52/ti48)o3) thick films deposited by aerosol deposition method. *Japanese Journal of Applied Physics*, 38(Part 1, No. 9B):5397–5401, sep 1999.

[68] Jun Akedo. Aerosol deposition of ceramic thick films at room temperature: Densification mechanism of ceramic layers. *Journal of the American Ceramic Society*, 89(6):1834–1839, 2006.

[69] Maria Rita Cicconi, Neamul H. Khansur, Udo R. Eckstein, Ferdinand Werr, Kyle G. Webber, and Dominique de Ligny. Determining the local pressure during aerosol deposition using glass memory. *Journal of the American Ceramic Society*, 103:2443–2452, 2020.

[70] Jong-Jin Choi, Kyung-Su Cho, Joon-Hwan Choi, Jungho Ryu, Byung-Dong Hahn, Woon-Ha Yoon, Jong-Woo Kim, Cheol-Woo Ahn, Jondo Yun, and Dong-Soo Park. Low temperature preparation and characterization of lsgmc based it-sofc cell by aerosol deposition. *Journal of the European Ceramic Society*, 32(1):115 – 121, 2012.

[71] Jong-Jin Choi, Joon-Hwan Choi, Jungho Ryu, Byung-Dong Hahn, Jong-Woo Kim, Cheol-Woo Ahn, Woon-Ha Yoon, and Dong-Soo Park. Microstructural evolution of ysz electrolyte aerosol-deposited on porous nio-ysz. *Journal of the European Ceramic Society*, 32(12):3249 – 3254, 2012.

[72] Jae-Hyun Jung, Byung-Dong Hahn, Woon-Ha Yoon, Dong-Soo Park, Jong-Jin Choi,

Jungho Ryu, Jong-Woo Kim, Cheolwoo Ahn, and Kie-Moon Song. Halogen plasma erosion resistance of rare earth oxide films deposited on plasma sprayed alumina coating by aerosol deposition. *Journal of the European Ceramic Society*, 32(10):2451 – 2457, 2012.

[73] Malgorzata Anna Piechowiak, Joseph Henon, Olivier Durand-Panteix, Grégory Etchegoyen, Valérie Coudert, Pascal Marchet, and Fabrice Rossignol. Growth of dense ti3sic2 max phase films elaborated at room temperature by aerosol deposition method. *Journal of the European Ceramic Society*, 34(5):1063 – 1072, 2014.

[74] So Baba, Hiroshi Sato, Lan Huang, Akiko Uritani, Ryoji Funahashi, and Jun Akedo. Formation and characterization of polyethylene terephthalate-based (bi0.15sb0.85)2te3 thermoelectric modules with cosb3 adhesion layer by aerosol deposition. *Journal of Alloys and Compounds*, 589:56 – 60, 2014.

[75] M.W. Lee, J.J. Park, D.Y. Kim, S.S. Yoon, H.Y. Kim, D.H. Kim, S.C. James, S. Chandra, Thomas Coyle, J.H. Ryu, W.H. Yoon, and D.S. Park. Optimization of supersonic nozzle flow for titanium dioxide thin-film coating by aerosol deposition. *Journal of Aerosol Science*, 42(11):771 – 780, 2011.

[76] Neamul H. Khansur, Udo Eckstein, Lisa Benker, Ulrike Deisinger, Benoit Merle, and Kyle G. Webber. Room temperature deposition of functional ceramic films on low-cost metal substrate. *Ceramics International*, 44(14):16295 – 16301, 2018.

[77] Hyungkwon Park, Jinyoung Kim, and Changhee Lee. Dynamic fragmentation process and fragment microstructure evolution of alumina particles in a vacuum kinetic spraying system. *Scripta Materialia*, 108:72 – 75, 2015.

[78] Chang-Wan Kim, Joo-Hyun Choi, Hyung-Jun Kim, Dong-Won Lee, Chang-Yong Hyun, and Song-Min Nam. Effects of interlayer roughness on deposition rate and morphology of aerosol-deposited al2o3 thick films. *Ceramics International*, 38(7):5621 – 5627, 2012.

[79] Yoshihiko Imanaka, Nobuyuki Hayashi, Masatoshi Takenouchi, and Jun Akedo. Aerosol deposition for post-ltcc. *Journal of the European Ceramic Society*, 27(8):2789 – 2795, 2007. Papers Presented at the Fourth International Conference on Microwave Materials and their Applications - MMA2006, Oulu, Finland.

[80] Song-Min Nam, Naoko Mori, Hirofumi Kakemoto, Satoshi Wada, Jun Akedo, and T. Tsurumi. Alumina thick films as integral substrates using aerosol deposition method. *Japanese Journal of Applied Physics*, 43:5414–5418, 08 2004.

[81] W. Hinds. Aerosol technology properties , behavior , and measurement of airborne particles second edition. 2012.

[82] Dong-Won Lee, Hyung-Jun Kim, Yoon-Hyun Kim, Young-Hoon Yun, and Song-Min Nam. Growth process of -al2o3 ceramic films on metal substrates fabricated at room temperature by aerosol deposition. *Journal of the American Ceramic Society*, 94(9):3131–3138, 2011.

[83] J. Akedo. Room temperature impact consolidation (rtic) of fine ceramic powder by aerosol deposition method and applications to microdevices. *Journal of Thermal Spray Technology*, 17:181–198, 2008.

[84] Joseph Henon, Malgorzata Anna Piechowiak, Olivier Durand-Panteix, Gregory Etchegoyen, Olivier Masson, Christelle Dublanche-Tixier, Pascal Marchet, Bruno Lucas, and Fabrice Rossignol. Dense and highly textured coatings obtained by aerosol deposition method from ti3sic2 powder: Comparison to a dense material sintered by spark plasma sintering. *Journal of the European Ceramic Society*, 35(4):1179 – 1189, 2015.

[85] Dong-Won Lee and S.-M Nam. Factors affecting surface roughness of al2o3 films deposited on cu substrates by an aerosol deposition method. *Journal of Ceramic Processing Research*, 11:100–106, 02 2010.

[86] Michael Schubert, Jörg Exner, and Ralf Moos. Influence of carrier gas composition on the stress of al2o3 coatings prepared by the aerosol deposition method. *Materials*, 7(8):5633–5642, 2014.

[87] So Baba and Jun Akedo. Thickness dependence of aerosol-deposited pb(zr,ti)o3 films on stainless-steel sheet annealed by co2 laser radiation. *Journal of Crystal Growth*, 275(1):e1247–e1252, 2005. Proceedings of the 14th International Conference on Crystal Growth and the 12th International Conference on Vapor Growth and Epitaxy.

[88] Jungho Ryu, Jong-Jin Choi, Byung-Dong Hahn, Dong-Soo Park, Woon-Ha Yoon, and Ki-Hoon Kim. Fabrication and ferroelectric properties of highly dense lead-free piezoelectric (k0.5na0.5)nbo3 thick films by aerosol deposition. *Applied Physics Letters*, 90(15):152901, 2007.

[89] Jong-Jin Choi, Joo-Hee Jang, Byung-Dong Hahn, Dong-Soo Park, Woon-Ha Yoon, Jungho Ryu, and Chan Park. Preparation of highly dense pzn–pzt thick films by the aerosol deposition method using excess-pbo powder. *Journal of the American Ceramic Society*, 90(11):3389–3394, 2007.

[90] Byung-Dong Hahn, Ki-Hun Kim, Dong-Soo Park, Jong-Jin Choi, Jungho Ryu, Woon-Ha Yoon, Chan Park, and Doh-Yeon Kim. Fabrication of lead zirconate titanate thick films using a powder containing organic residue. *Japanese Journal of Applied Physics*, 47(7):5545–5552, jul 2008.

[91] Takuya Hoshina, Tsutomu Furuta, Yoichi Kigoshi, Saki Hatta, Naohiro Horiuchi, Hiroaki Takeda, and Takaaki Tsurumi. Size effect of nanograined BaTiO3 ceramics fabricated by aerosol deposition method. *Japanese Journal of Applied Physics*, 49(9 PART 2), 2010.

[92] Hong-Ki Kim, Seung-Hwan Lee, Soo In Kim, Chang Woo Lee, Jung Rag Yoon, Sung-Gap Lee, and Young-Hie Lee. Dielectric strength of voidless batio3 films with nano-scale grains fabricated by aerosol deposition. *Journal of Applied Physics*, 115(1):014101, 2014.

[93] M. Suzuki and J. Akedo. Temperature dependence of dielectric properties of barium titanate ceramic films prepared by aerosol deposition method. *Japanese Journal of Applied Physics*, 49(9 PART 2), 2010.

[94] P. Muhammed Shafi and A. Chandra Bose. Impact of crystalline defects and size on x-ray line broadening: A phenomenological approach for tetragonal sno2 nanocrystals. *AIP Advances*, 5(5):057137, 2015.

[95] G. Arlt, D. Hennings, and G. de With. Dielectric properties of fine-grained barium titanate ceramics. *Journal of Applied Physics*, 58(4):1619–1625, 1985.

[96] Defeng Mo, Tingfeng Song, Yongjian Fang, Charles Luo, Machael Simpson, and Zhiping Luo. A review on diffusion bonding between titanium alloys and stainless steels. *Advances in Materials Science and Engineering*, 2018:1–15, 09 2018.

[97] Abdel-Aziz Mel. The kirkendall effect and nanoscience: hollow nanospheres and nanotubes. *Beilstein Journal of Nanotechnology*, 6:1348–1361, 06 2015.

[98] M.-H. Kim, Y.-W. Choi, H.-Y. Choi, and K.-B. Myung. Prurigo pigmentosa from contact allergy to chrome in detergent. *Contact Dermatitis*, 44(5):289–292, 2001.

[99] M.B. Hansen, S. Rydin, T. Menné, and J.D. Johansen. Quantitative aspects of contact allergy to chromium and exposure to chrome-tanned leather. *Contact Dermatitis*, 47(3):127–134, 2002.

[100] A. Mahto and B. De Silva. Leather sofa dermatitis due to contact allergy to chrome: An unusual cause of eczema in a child. *Br. J. Dermatol.*, 161:126–127, 2009.

[101] S.M Bruemmer and L.A Charlot. Development of grain boundary chromium depletion in type 304 and 316 stainless steels. *Scripta Metallurgica*, 20(7):1019–1024, 1986.

[102] T. Thorvaldsson and A. Salwén. Measurement of diffusion coefficients for cr at low temperatures in a type 304 stainless steel. *Scripta Metallurgica*, 18(7):739–742, 1984.

[103] Chu Liang, Yun Chen, Min Wu, Kai Wang, Wenkui Zhang, Yongping Gan, Haobo

Huang, Jian Chen, Yang Xia, Jun Zhang, Shiyou Zheng, and Hongge Pan. Green synthesis of graphite from co2 without graphitization process of amorphous carbon. *Nature Communications*, 12, 01 2021.

[104] Sujith Nair, Tuhin Saha, Pranab Dey, and Sambhu Bhadra. Thermal oxidation of graphite as the first step for graphene preparation: effect of heating temperature and time. *Journal of Materials Science*, 56:1–17, 02 2021.

[105] Z. Osváth, Al. Darabont, P. Nemes-Incze, E. Horváth, Z.E. Horváth, and L.P. Biró. Graphene layers from thermal oxidation of exfoliated graphite plates. *Carbon*, 45(15):3022–3026, 2007.

[106] Haiyan Wang, Yao Tian, Jinglei Li, and Xiao Chen. Experimental study on thermal effect and gas release laws of coal-polyurethane cooperative spontaneous combustion. *Scientific Reports*, 11:1994, 01 2021.

[107] Seshu B. Desu. Influence of stresses on the properties of ferroelectric BaTiO3 thin films. *Journal of The Electrochemical Society*, 140(10):2981–2987, oct 1993.

[108] Guifang Han, Jungho Ryu, Woon Ha Yoon, Jong Jin Choi, Byung Dong Hahn, Jong Woo Kim, Dong Soo Park, Cheol Woo Ahn, Shashank Priya, and Dae Yong Jeong. Stress-controlled pb(zr 0.52ti 0.48)o 3 thick films by thermal expansion mismatch between substrate and pb(zr 0.52ti 0.48)o 3 film. *Journal of Applied Physics*, 110(12), dec 2011.

[109] A. C. Dent, C. R. Bowen, R. Stevens, M. G. Cain, and M. Stewart. Effective elastic properties for unpoled barium titanate. *Journal of the European Ceramic Society*, 27:3739–3743, 2007.

[110] Terufumi Sasaki, Kenji Watanabe, Kiyohiko Nohara, Yutaka Ono, Nobuyuki Kond, and Shuzo Sat. Physical and mechanical properties of high manganese non-magnetic steel and its application to various products for commercial use*. 1982.

[111] Nasrin Lotfibakhshaiesh, Delia S. Brauer, and Robert G. Hill. Bioactive glass engineered coatings for ti6al4v alloys: Influence of strontium substitution for calcium on sintering behaviour. *Journal of Non-Crystalline Solids*, 356:2583–2590, 10 2010.

[112] J M Blamey and T V Parry. Strength and toughness of barium titanate ceramics. Technical report, 1993.

[113] Jörg Exner, Tobias Nazarenus, Dominik Hanft, Jaroslaw Kita, and Ralf Moos. What happens during thermal post-treatment of powder aerosol deposited functional ceramic films? explanations based on an experiment-enhanced literature survey. *Advanced Materials*, 32, 5 2020.

[114] Jungho Ryu, Shashank Priya, Chee Sung Park, Kun Young Kim, Jong Jin Choi, Byung Dong Hahn, Woon Ha Yoon, Byoung Kuk Lee, Dong Soo Park, and Chan Park. Enhanced domain contribution to ferroelectric properties in freestanding thick films. *Journal of Applied Physics*, 106(2), 2009.

[115] Malgorzata Anna, Joseph Henon, Olivier Durand-panteix, Grégory Etchegoyen, Valérie Coudert, Pascal Marchet, and Fabrice Rossignol. Growth of dense ti 3 sic 2 max phase films elaborated at room temperature by aerosol deposition method. *Journal of the European Ceramic Society*, 34(5):1063–1072, 2014.

[116] Jun ichi Itoh, Isamu Yashima, Naoki Ohashi, Isao Sakaguchi, Hajime Haneda, and Junzo Tanaka. Ni ion diffusion in barium titanate perovskite. *Journal of the Ceramic Society of Japan*, 109(1275):955–959, 2001.

[117] Muhammad Ali Siddiqui, Fayaz Hussain, M Sohail Hanif, and Ahmad Azmin Mohamad. Effect of calcination and sintering temperatures on physical properties of barium titanate ceramic. *International Journal of Electroactive Materials*, 6(4):42–47, 2018.

[118] Zhao Yao, Cong Wang, Yang Li, Hong Ki Kim, and Nam Young Kim. Effects of starting powder and thermal treatment on the aerosol deposited BaTiO3 thin films toward less leakage currents. *Nanoscale Research Letters*, 9(1), 2014.

[119] Hong Ki Kim, Seung Hwan Lee, Sung Gap Lee, and Young Hie Lee. Densification mechanism of BaTiO3 films on Cu substrates fabricated by aerosol deposition. *Electronic Materials Letters*, 11(3):388–397, 2015.

[120] Scooter D. Johnson, Fritz J. Kub, and Charles R. Eddy Jr. ZnS/diamond composite coatings for infrared transmission applications formed by the aerosol deposition method. In Randal W. Tustison and Brian J. Zelinski, editors, *Window and Dome Technologies and Materials XIII*, volume 8708, pages 173 – 184. International Society for Optics and Photonics, SPIE, 2013.

[121] Kensuke Mihara, Takuya Hoshina, Hiroaki Takeda, and Takaaki Tsurumi. Controlling factors of film-thickness in improved aerosol deposition method. *Journal of the Ceramic Society of Japan*, 117(1368):868–872, 2009.

[122] Takuya Hoshina, Satoshi Wada, Yoshihiro Kuroiwa, and Takaaki Tsurumi. Composite structure and size effect of barium titanate nanoparticles. *Applied Physics Letters*, 93(19):192914, 2008.

[123] Takaaki Tsurumi, Takuya Hoshina, Hiroaki Takeda, Youichi Mizuno, and Hirokazu Chazono. Size effect of barium titanate and computer-aided design of multilayered ceramic

capacitors. *IEEE Transactions on Ultrasonics, Ferroelectrics, and Frequency Control*, 56(8):1513–1522, 2009.

[124] Hironori Hatono, Tomokazu Ito, and Akihiko Matsumura. Application of BaTiO3film deposited by aerosol deposition to decoupling capacitor. *Japanese Journal of Applied Physics*, 46(10B):6915–6919, oct 2007.

[125] Kenji Uchino, Eiji Sadanaga, and Terukiyo Hirose. Dependence of the crystal structure on particle size in barium titanate. *Journal of the American Ceramic Society*, 72(8):1555–1558, 1989.

[126] Kenji Ishikawa, Kazutoshi Yoshikawa, and Nagaya Okada. Size effect on the ferroelectric phase transition in pbtio$_3$ ultrafine particles. *Phys. Rev. B*, 37:5852–5855, Apr 1988.

[127] S. Wada, K. Yako, K. Yokoo, H. Kakemoto, and T. Tsurumi. Domain wall engineering in barium titanate single crystals for enhanced piezoelectric properties. *Ferroelectrics*, 334(1):17–27, 2006.

[128] Encyclopedia of physics; 3d ed.; 2v. *SciTech Book News*, 30(1), 2006.

[129] Jong Min Oh and Song Min Nam. Causes of high leakage currents in thin BaTiO3 films prepared by aerosol deposition method. *Journal of the Korean Physical Society*, 56(12):448–452, 2010.

[130] Hong Ki Kim, Jong Min Oh, Soo In Kim, Hyung Jun Kim, Chang Woo Lee, and Song Min Nam. Relation between electrical properties of aerosol-deposited BaTiO3 thin films and their mechanical hardness measured by nano-indentation. *Nanoscale Research Letters*, 7:1–16, 2012.

[131] Jong Min Oh, Hyung Jun Kim, and Song Min Nam. Characterization of leakage current mechanisms for aerosol-deposited BaTiO3 thin films at room temperature. *Journal of the Korean Physical Society*, 57(41):1096–1101, 2010.

[132] Ashutosh Kumar Dubey, Ryota Kinoshita, and Ken Ichi Kakimoto. Piezoelectric sodium potassium niobate mediated improved polarization and in vitro bioactivity of hydroxyapatite. *RSC Advances*, 5(25):19638–19646, 2015.

[133] Takeshi Iwasaki, Yumi Tanaka, Miho Nakamura, Akiko Nagai, Kazuaki Hashimoto, Yoshitomo Toda, Keiichi Katayama, and Kimihiro Yamashita. Rate of bonelike apatite formation accelerated on polarized porous hydroxyapatite. *Journal of the American Ceramic Society*, 91(12):3943–3949, 2008.

[134] Koichi Marubashi, Takashi Yoshiyasu, Toshihito Kakiuchi, and Kunio Furusawa. Stabil-

ity of aqueous pigment dispersions with new microbial products. *Journal of the Society of Powder Technology, Japan*, 37(9):634–638, 2000.

[135] M.C. Blanco López, B. Rand, and F.L. Riley. The isoelectric point of batio3. *Journal of the European Ceramic Society*, 20(2):107–118, 2000.

[136] Sushree Swarupa Tripathy and Ashok M. Raichur. Dissolution properties of BaTiO3 nanoparticles in aqueous suspensions. *Journal of Experimental Nanoscience*, 6(2):127–137, 2011.

[137] Maria del Carmen Blanco López, Georgios Fourlaris, Brian Rand, and Frank L. Riley. Characterization of barium titanate powders: Barium carbonate identification. *Journal of the American Ceramic Society*, 82(7):1777–1786, 1999.

[138] M.C. Blanco-Lopez, B. Rand, and F.L. Riley. The properties of aqueous phase suspensions of barium titanate. *Journal of the European Ceramic Society*, 17(2):281–287, 1997.

[139] M.C. Blanco López, B. Rand, and F.L. Riley. Polymeric stabilisation of aqueous suspensions of barium titanate. part i: Effect of ph. *Journal of the European Ceramic Society*, 20(10):1579–1586, 2000.

[140] Achim Neubrand, Reinhard Lindner, and Peter Hoffmann. Room-temperature solubility behavior of barium titanate in aqueous media. *Journal of the American Ceramic Society*, 83(4):860–864, 2000.

[141] Chia Wen Chiang and Jau Ho Jean. Effects of barium dissolution on dispersing aqueous barium titanate suspensions. *Materials Chemistry and Physics*, 80(3):647–655, 2003.

[142] Zongru Li, Qingshan Fu, Yongqiang Xue, and Zixiang Cui. Effect of size on dissolution thermodynamics of nanoparticles: A theoretical and experimental research. *Materials Chemistry and Physics*, 214:499–506, 2018.

[143] Matthias M. Waegele, Charuni M. Gunathunge, Jingyi Li, and Xiang Li. How cations affect the electric double layer and the rates and selectivity of electrocatalytic processes. *Journal of Chemical Physics*, 151(16):1DUMMT, 2019.

[144] Eliezer Gileadi and Noam Eliaz. *Chapter 8: The Electrical Double Layer (EDL)*. Wiley-VCH, 2019.

[145] Xiong Lu and Yang Leng. Theoretical analysis of calcium phosphate precipitation in simulated body fluid. *Biomaterials*, 26(10):1097–1108, 2005.

[146] Abdul R. Chughtai, Robert Marshall, and George H. Nancollas. Complexes in calcium

phosphate solutions. *The Journal of Physical Chemistry*, 72(1):208–211, 1968. PMID: 5634900.

[147] Arne Erik Nielsen. Electrolyte crystal growth mechanisms. *Journal of Crystal Growth*, 67(2):289–310, 1984.

[148] M.C van der Leeden, D Kashchiev, and G.M Van Rosmalen. Precipitation of barium sulfate: Induction time and the effect of an additive on nucleation and growth. *Journal of Colloid and Interface Science*, 152(2):338–350, 1992.

[149] H. Mas Ayu, S. Izman, R. Daud, G. Krishnamurithy, A. Shah, S.H. Tomadi, and M.S. Salwani. Surface modification on cocrmo alloy to improve the adhesion strength of hydroxyapatite coating. *Procedia Engineering*, 184:399–408, 2017. Advances in Material Processing Technologies Conference.

[150] Larry L. Hench. Bioceramics: From concept to clinic. *Journal of the American Ceramic Society*, 74(7):1487–1510, 1991.

[151] Philips N. Gunawidjaja, Andy Y. H. Lo, Isabel Izquierdo-Barba, Ana García, Daniel Arcos, Baltzar Stevensson, Jekabs Grins, María Vallet-Regí, and Mattias Edén. Biomimetic apatite mineralization mechanisms of mesoporous bioactive glasses as probed by multinuclear 31p, 29si, 23na and 13c solid-state nmr. *The Journal of Physical Chemistry C*, 114(45):19345–19356, 2010.

Appendicies

7.1 Appendix A - TOPAS Pawley fit data

Table 7.1: Pawley fit data for samples BTSS 3.1 (As sprayed), BTSS 1.3 (400°C), BTSS 1.4 (550°C), BTSS 3.2 (650°C), BTSS 2.3 (750°C) with respect to tetragonal barium titanate (PDF 04-010-4893)

Condition	a(Å)	c(Å)	LVol-IB(nm)	Cell volume(Å^3)
As Sprayed	4.0095461	4.0601339	9.398	65.27258
400°C	4.0024438	4.0315418	11.838	64.58351
550°C	4.0062101	4.0330542	13.065	64.72939
650°C	4.0100080	4.0365630	15.474	64.90859
750°C	4.0106544	4.0368916	20.313	64.93481
Tetragonal	3.9998	4.0180	-	64.28

Table 7.2: BTTi Pawley fit data for samples BTTi 2.1 (As sprayed), BTTi 1.1 (400°C), BTTi 2.4 (550°C), BTTi 3.1 (650°C), BTTi 2.3 (750°C) with respect to tetragonal barium titanate (PDF 04-010-4893)

Condition	a (Å))	c (Å)	LVol-IB (nm)	Cell volume (Å^3)
As sprayed	4.0150212	4.0722836	8.861	65.64682
400°C	3.9959506	4.0335603	11.819	64.40636
550°C	3.9958758	4.0307846	13.554	64.35963
650°C	3.9983962	4.0259935	16.866	64.36425
750°C	4.0028319	4.0224167	20.703	64.44983
Tetragonal	3.9998	4.018	-	64.28

Table 7.3: BCZTTi Pawley fit data for sample BCZTTi 2.1 (As sprayed), BCZTTi 1.1 (400°C), BCZTTi 1.2 (550°C), BCZTTi 1.3 (650°C), BCZTTi 1.4 (750°C) with respect to tetragonal phase BCZT (PDF 01-086-8334)

Condition	a (Å)	c (Å)	LVol-IB (nm)	Cell volume ($Å^3$)
As sprayed	3.9774951	4.0382335	9.756	63.88674
400°C	3.9962699	4.0334726	10.092	64.41525
550°C	3.9835174	4.0360878	13.082	64.04630
650°C	3.9891990	4.0286885	14.603	64.11137
750°C	3.9948490	4.0224790	14.294	64.19401
Tetragonal	3.9836	3.9995	-	63.47

7.2 Appendix B - Sacrificial sample $d33$ measurements

Table 7.4: Negative values for BTSS samples measured with the coating facing up in the Berlincourtmeter after corona discharge poling.

Poling time (s)	0	10	30	60	180	300	420	540
1st measurement	-1.10	-2.60	-3.00	-3.20	-3.30	-4.10	-3.20	-3.70
2nd measurement	-1.30	-2.10	-3.10	-4.10	-4.10	-3.90	-5.30	-4.20
3rd measurement	-1.70	-2.80	-3.60	-4.90	-4.10	-4.60	-4.60	-6.80
Average	-1.37	-2.50	-3.23	-4.07	-3.83	-4.20	-4.37	-4.90
Standard deviation	0.31	0.36	0.32	0.85	0.46	0.36	1.07	1.66

Table 7.5: Positive values for BTSS samples measured with the coating facing down in the Berlincourtmeter after corona discharge poling.

Poling time (s)	0	10	30	60	180	300	420	540
1st measurement	0.50	0.50	1.10	1.10	1.90	1.90	1.30	2.20
2nd measurement	0.40	0.00	0.60	2.10	1.50	2.00	3.20	2.20
3rd measurement	-0.30	-0.60	1.70	2.30	2.10	2.50	2.20	4.50
Average	0.20	-0.03	1.13	1.83	1.83	2.13	2.23	2.97
Standard deviation	0.44	0.55	0.55	0.64	0.31	0.32	0.95	1.33

7.3 Appendix C - FS-XRD spectra soaking study

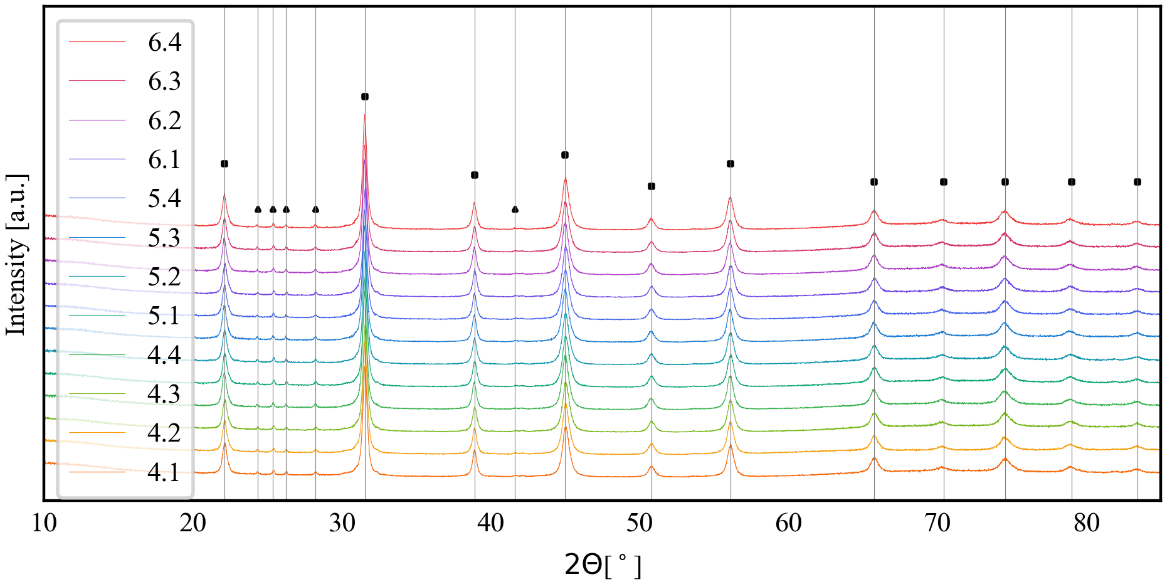

Figure 7.1: FS-XRD diffractogram for BTSS samples 4.1-6.4 after heat-treatment before soaking. Tetragonal $BaTiO_3$ (PDF 04-010-4893) (■) is present in all samples along with $BaCrO_4$ (PDF 04-008-7985) (▲)

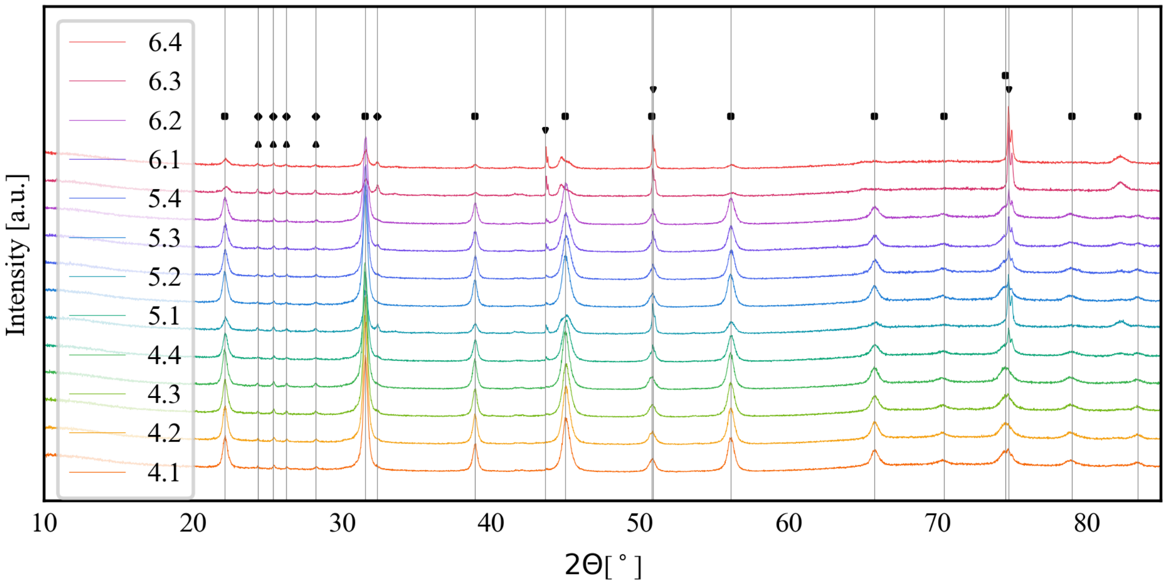

Figure 7.2: FS-XRD diffractogram for BTSS samples 4.1-6.4 after soaking in SBF. Tetragonal $BaTiO_3$ (PDF 04-010-4893) (■) is present in some coatings along with $BaCrO_4$ (PDF 04-008-7985) (▲). The appearance of calcium phosphate is marked by (PDF 00-050-0584)(◆) and shares some peaks with $BaCrO_4$. (▼) marks the stainless steel substrate (PDF 00-033-0397).

7.4 Appendix D - Hardness and Reduced Modulus data

Table 7.6: Calculated hardness and reduced modulus values for BTSS, BTTi and BCZTTi samples

Measurement	**BTSS 3.1 AS**		**BTSS 1.3 400°C**	
	E_r(GPa)	**H(GPa)**	**E_r(GPa)**	**H(GPa)**
1	118.822915	1.783123	109.276101	3.568092
2	117.942555	3.889626	114.059727	3.358693
3	128.940026	3.016572	131.345728	3.611975
4	88.391966	1.967674	138.585198	4.361951
5	107.427014	1.601712	92.685863	3.122592
6	102.676913	3.067098	138.167241	4.507856
7	141.627311	2.749131	105.210072	3.003444
8	98.468585	2.86548	-	-
9	-	-	-	-
Average	113.0371606	2.617552	118.4757043	3.647800429
Standard deviation	16.14881251	0.725328049	16.48814438	0.53877715
Measurement	**BTSS 1.4 550°C**		**BTSS 2.1 650°C**	
	E_r(GPa)	**H(GPa)**	**E_r(GPa)**	**H(GPa)**
1	113.303434	3.067151	63.083936	1.246058
2	122.979097	3.686396	86.074988	1.91465
3	115.656285	3.148579	140.629333	4.83512
4	117.19458	3.222409	100.010202	2.542281
5	108.651808	3.794746	67.042898	1.254006
6	129.139214	4.108186	97.724146	1.950254
7	86.189549	2.747296	157.716758	4.495569
8	151.472555	3.677418	-	-
9	-	-	-	-
Average	118.0733153	3.431522625	101.7546087	2.605419714
Standard deviation	17.30872379	0.42425639	32.96853093	1.369504728
Measurement	**BTSS 2.2 750°C**		**BTTi 2.1 AS**	
	E_r(GPa)	**H(GPa)**	**E_r(GPa)**	**H(GPa)**
1	155.565424	2.228854	42.522399	0.983939
2	109.540524	2.379041	81.183304	2.496089
3	116.456898	2.28903	75.369415	0.966763

Continued on next page

Table 7.6 – continued from previous page

4	63.78866	1.30425	105.119533	2.245961
5	78.708921	1.648621	137.013984	4.279127
6	167.22517	3.988833	120.260033	3.258915
7	110.627657	2.322286	158.724779	4.988291
8	83.269378	1.130712	94.138589	2.937006
9	93.970882	1.979449	85.278114	1.653693
Average	108.7948349	2.141230667	99.95668333	2.645531556
Standard deviation	32.43151946	0.783369777	32.94911025	1.306532289
Measurement	**BTTi 1.1 400°C**		**BTTi 1.2 550°C**	
	E_r(GPa)	**H(GPa)**	**E_r(GPa)**	**H(GPa)**
1	228.521398	4.455726	142.164774	2.283062
2	63.324698	0.738875	177.036143	2.894527
3	191.287137	6.810328	112.361285	1.437985
4	71.441766	0.889921	172.143244	5.749786
5	193.550031	5.0881	169.145681	3.367687
6	218.506058	6.255314	149.335895	2.993192
7	116.705407	3.511257	126.959501	4.288663
8	54.392223	0.391482	140.075583	4.562857
9	97.466891	1.338543	159.653229	3.604193
Average	137.2439566	3.275505111	149.8750372	3.464661333
Standard deviation	66.40664425	2.364157115	20.51758321	1.210445774
Measurement	**BTTi 1.3 650°C**		**BCZTTi 2.1 AS**	
	E_r(GPa)	**H(GPa)**	**E_r(GPa)**	**H(GPa)**
1	56.083081	1.23582	82.62435	2.110224
2	78.476121	1.858922	70.950458	1.58812
3	75.101679	1.494741	97.916513	3.593455
4	72.022562	1.991122	110.92527	2.197468
5	102.823922	4.191796	126.242833	3.97208
6	79.312612	2.166146	154.763258	5.170842
7	105.674324	2.382684	218.550182	7.647206
8	66.710705	1.566658	119.366011	2.462357
9	80.758886	1.527612	106.842354	3.851072
Average	79.66265467	2.046166778	120.9090254	3.621424889

Continued on next page

Table 7.6 – continued from previous page

Standard deviation	14.97667138	0.831933101	41.49767329	1.781797923
Measurement	**BCZTTi 1.1 400°C**		**BCZTTi 1.2 550°C**	
	E_r(GPa)	**H(GPa)**	**E_r(GPa)**	**H(GPa)**
1	161.607112	3.661877	169.508946	6.455775
2	138.485746	5.11426	138.394697	2.952134
3	101.976623	3.002713	161.274659	6.760861
4	141.676369	3.191937	98.279645	1.887996
5	78.232764	3.255537	156.589897	3.74325
6	128.028671	4.385061	117.63891	3.759293
7	135.482287	4.605697	263.011145	5.761425
8	-	-	130.491047	1.472105
9	-	-	93.49618	1.658924
Average	126.4985103	3.888154571	147.6316807	3.827973667
Standard deviation	25.69221668	0.754533903	47.96107376	1.944873582
Measurement	**BCZTTi 1.3 650°C**		**BCZTTi 1.4 750°C**	
	E_r(GPa)	**H(GPa)**	**E_r(GPa)**	**H(GPa)**
1	82.262829	3.340132	133.382181	4.143139
2	97.218747	2.826007	190.048006	8.585364
3	134.790773	3.275465	170.813622	4.779654
4	121.717836	8.409338	262.818842	11.892683
5	56.536555	1.336613	116.895844	2.442051
6	141.470895	6.524203	158.747786	3.358826
7	70.512665	1.784361	180.308988	5.055853
8	72.911382	3.544603	128.192149	3.281262
Average	97.17771025	3.88009025	167.6509273	5.442354
Standard deviation	29.90168195	2.242976394	43.46762707	2.995308741

7.5 Appendix E - Berlincourtmeter measurement values all material systems

Table 7.7: Berlincourtmeter d_{33} values for all material systems

Sample Condition	d_{33} (pC/N)		
	BTSS	**BTTi**	**BCZTTi**
As Sprayed	-0.1 ± 0.005	-0.4 ± 0.020	-0.9 ± 0.045
400°C	-8.7 ± 0.435	-1.1 ± 0.055	-8.9 ± 0.445
550°C	-8.7 ± 0.435	-2.8 ± 0.140	-9.0 ± 0.450
650°C	-2.7 ± 0.135	-1.0 ± 0.05	-0.9 ± 0.045
750°C	-2.1 ± 0.105	n/a	-1.0 ± 0.050

7.6 Appendix F - Nano-indentation force-displacement curves

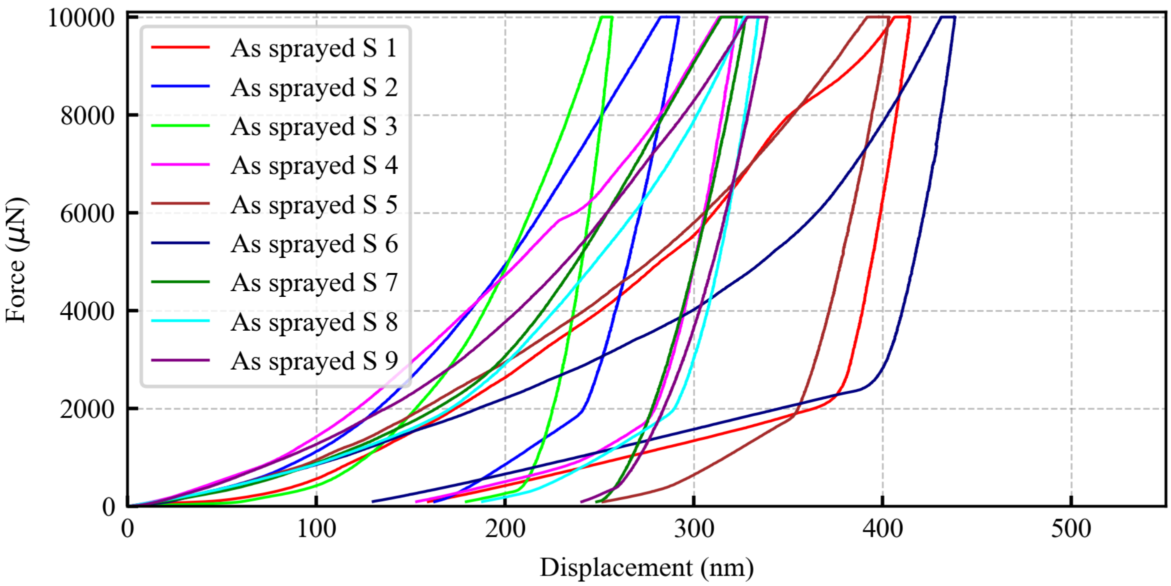

Figure 7.3: Force - displacement curve BTSS 3.1 As sprayed

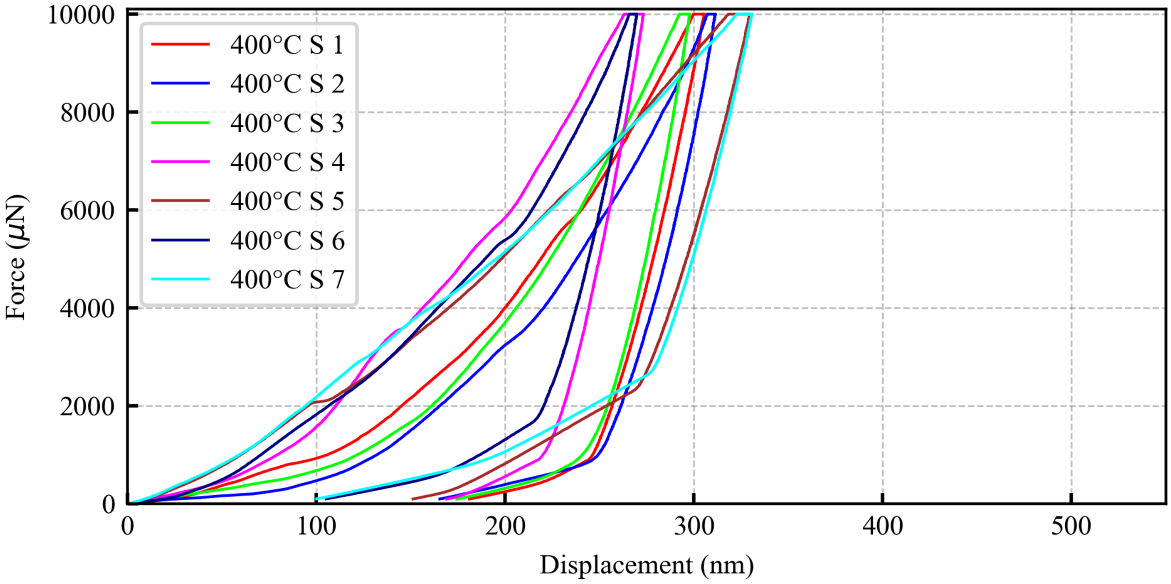

Figure 7.4: Force - displacement curve BTSS 1.3 400°C

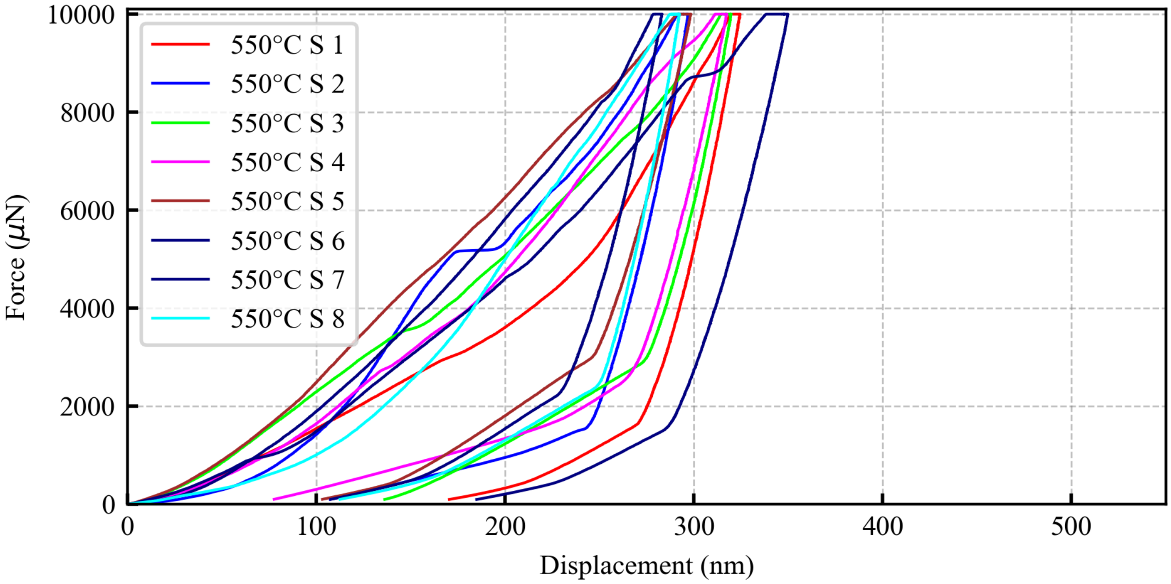

Figure 7.5: Force - displacement curve BTSS 1.4 550°C

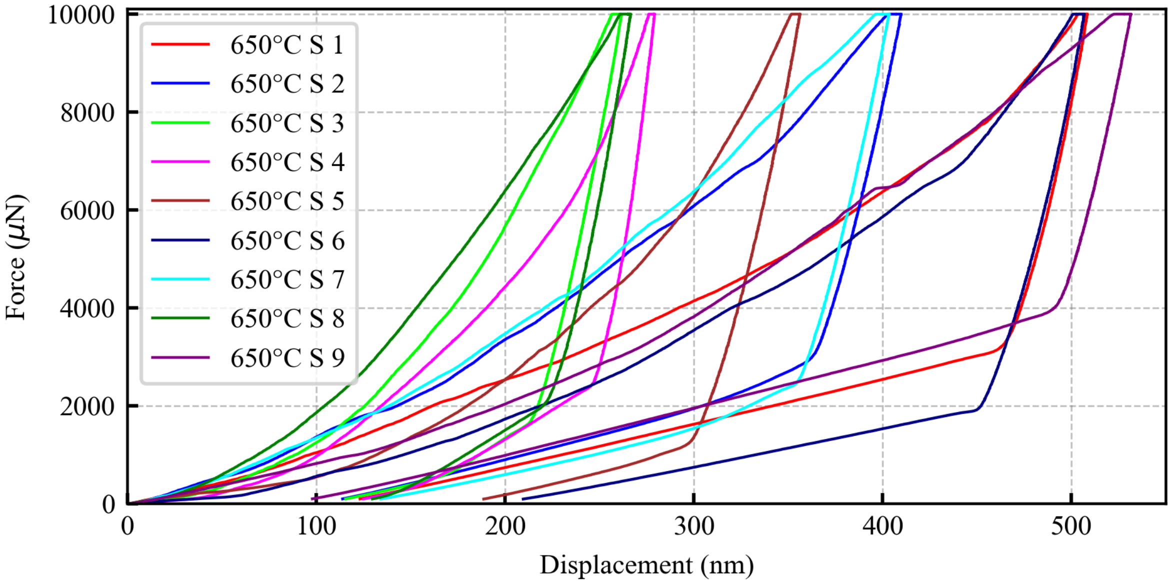

Figure 7.6: Force - displacement curve BTSS 3.2 650°C

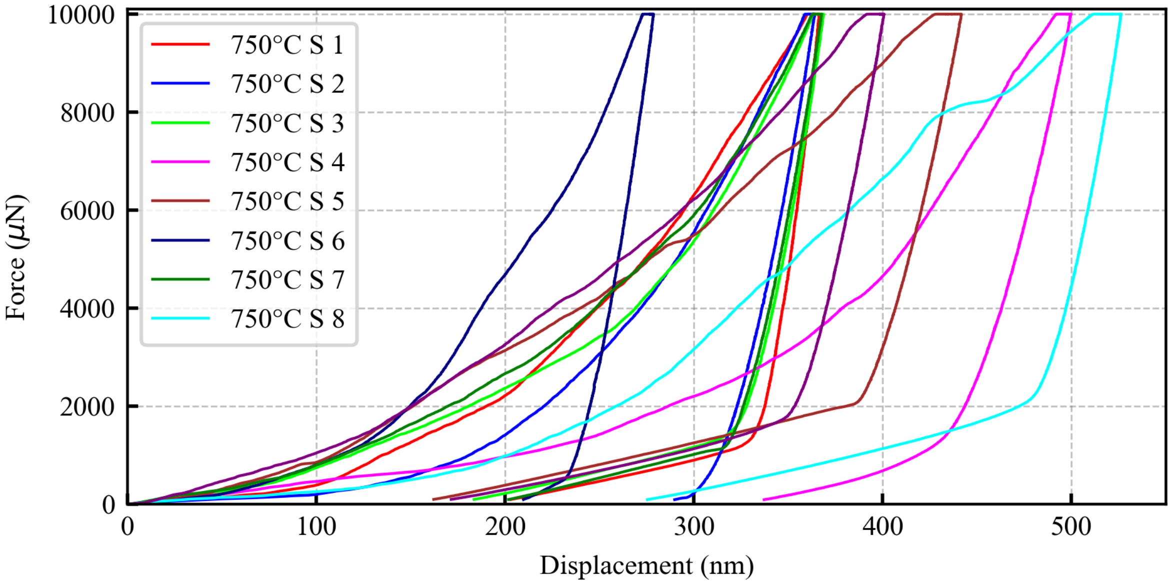

Figure 7.7: Force - displacement curve BTSS 2.3 750°C

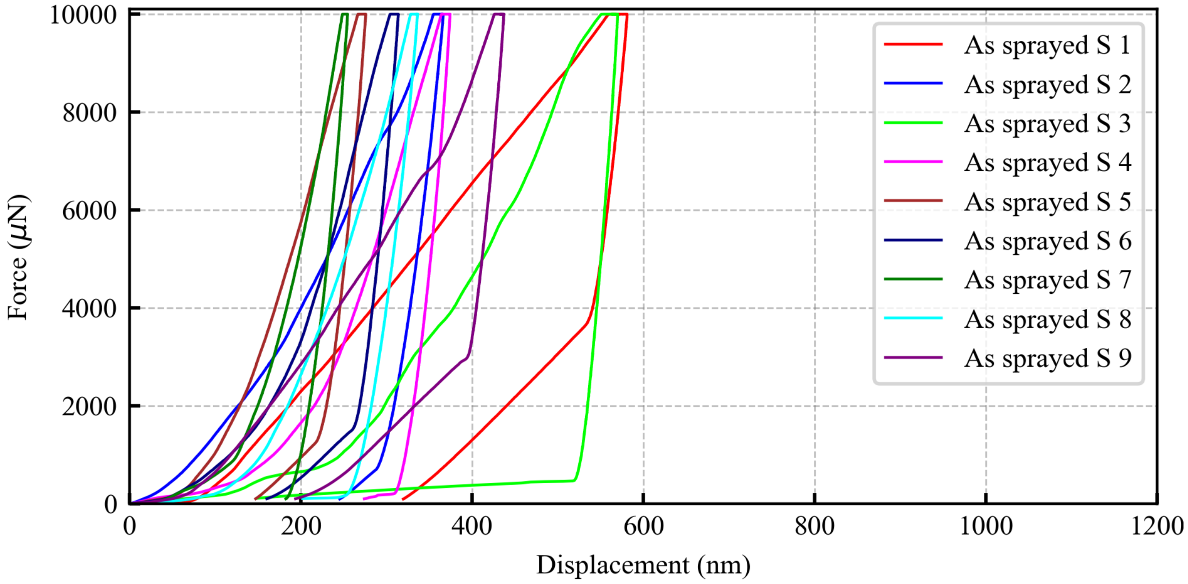

Figure 7.8: Force - displacement curve BTTi 2.1 As sprayed

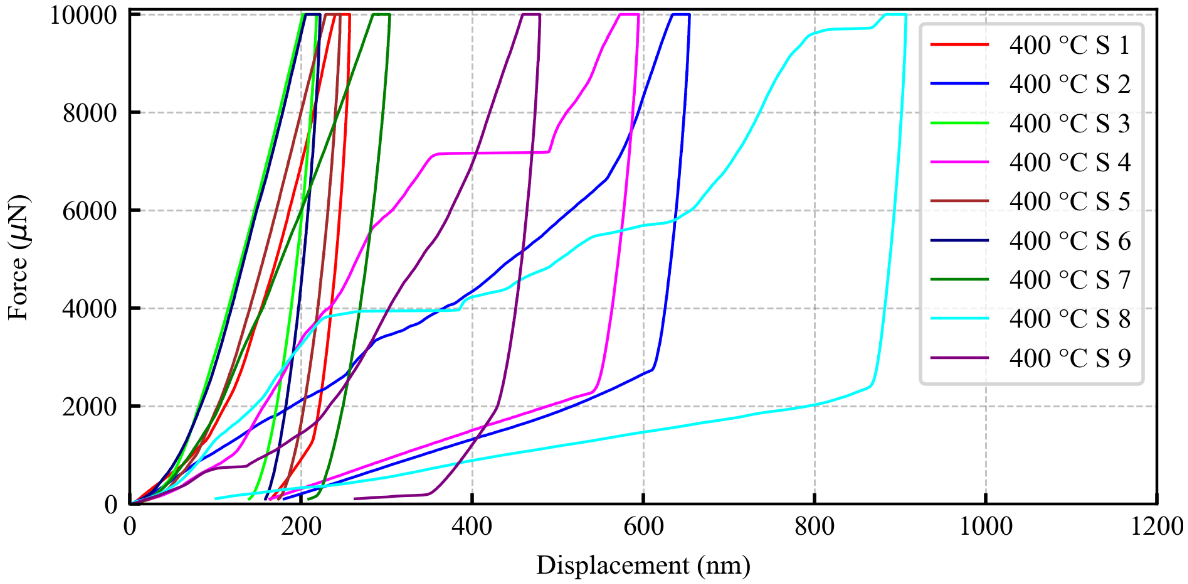

Figure 7.9: Force - displacement curve BTTi 1.1 400°C

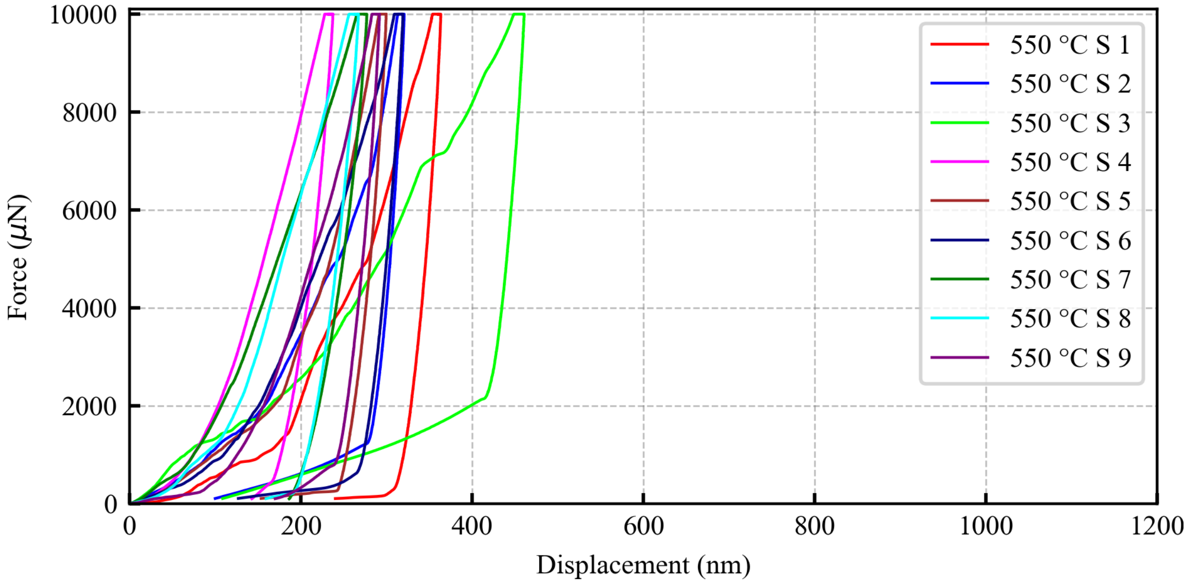

Figure 7.10: Force - displacement curve BTTi 2.4 550℃

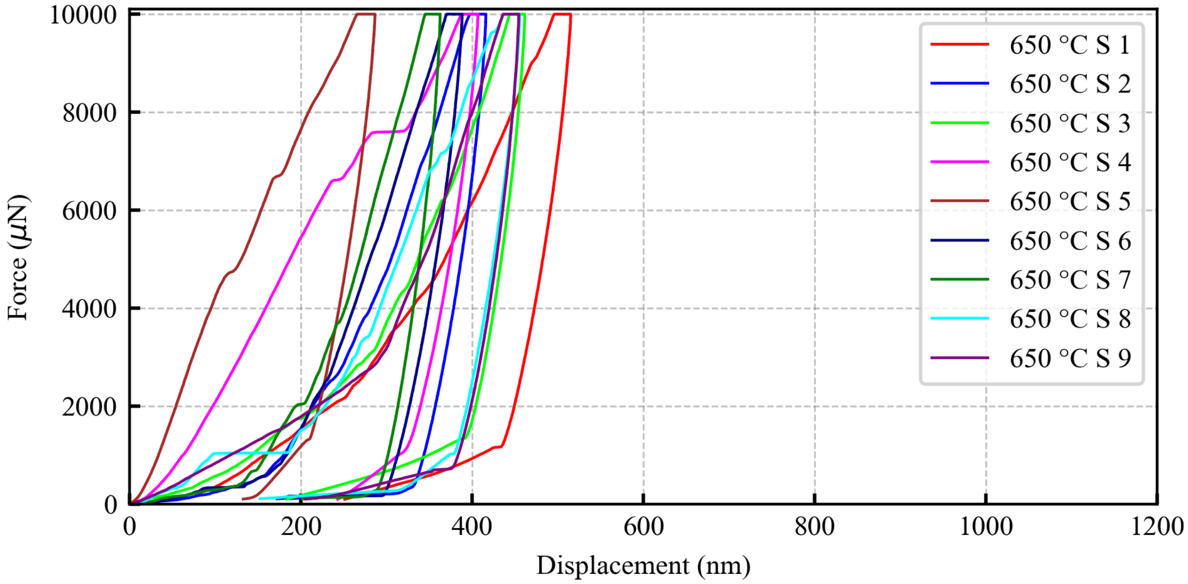

Figure 7.11: Force - displacement curve BTTi 3.1 650℃

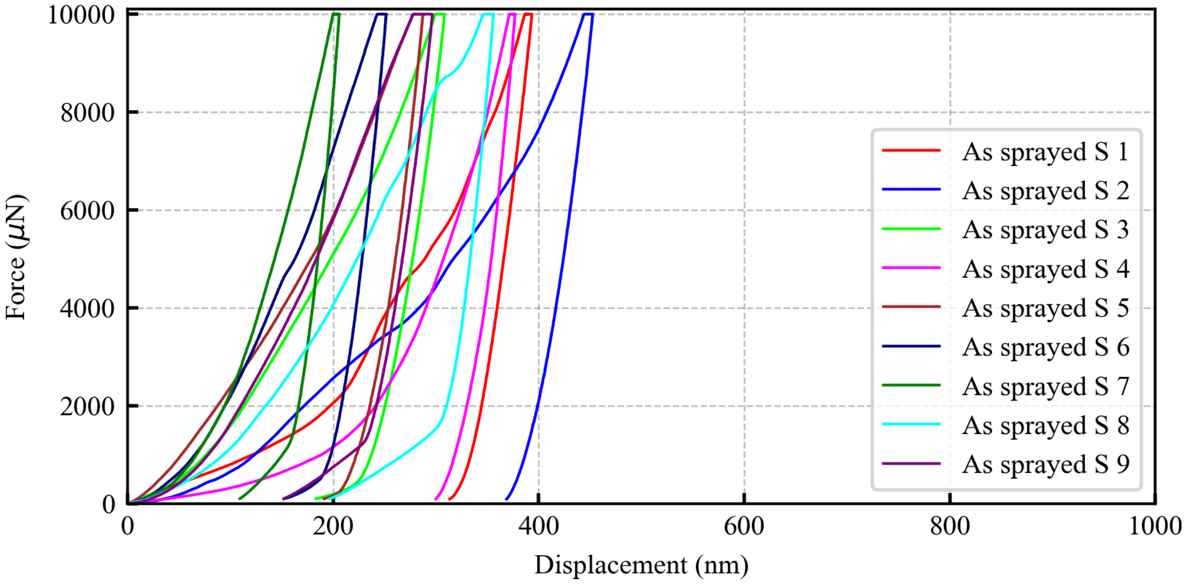

Figure 7.12: Force - displacement curve BCZTTi 2.1 As sprayed

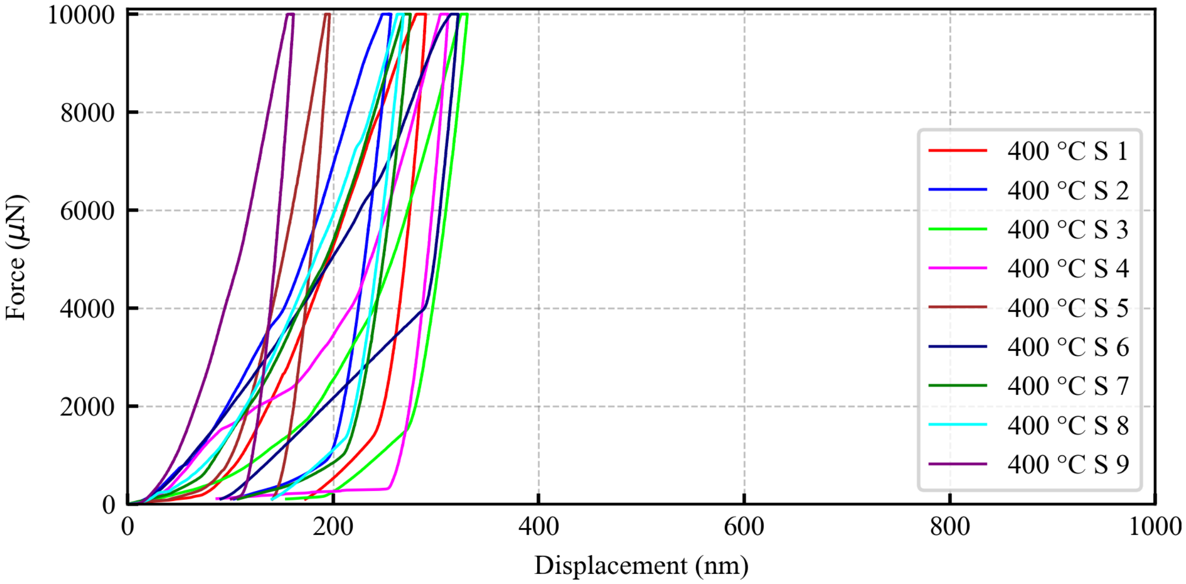

Figure 7.13: Force - displacement curve BCZTTi 1.1 400℃

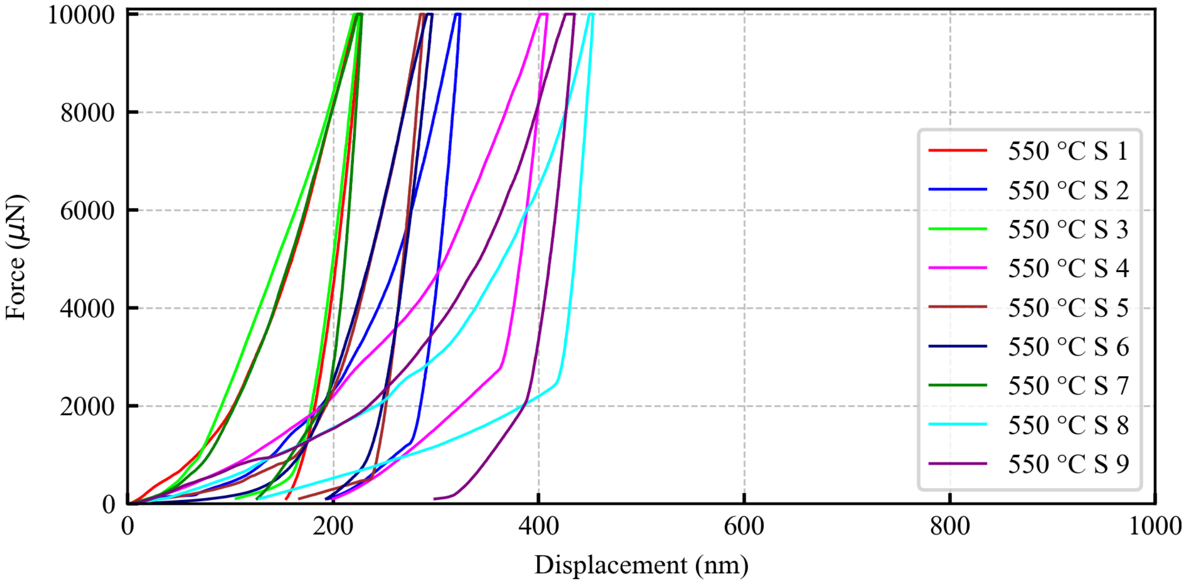

Figure 7.14: Force - displacement curve BCZTTi 1.2 550°C

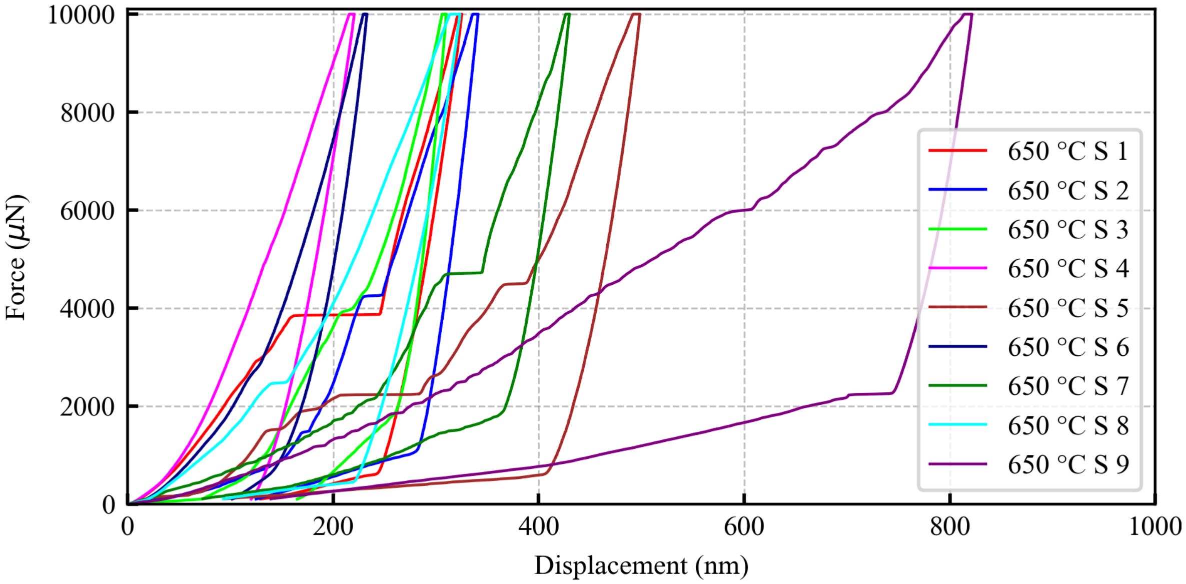

Figure 7.15: Force - displacement curve BCZTTi 1.3 650°C

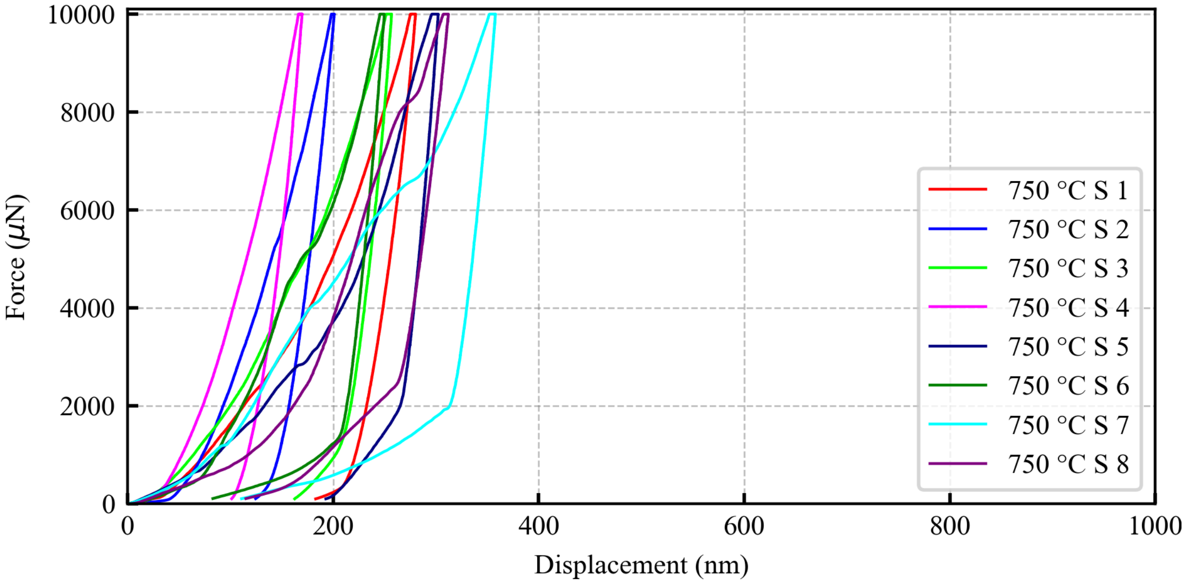

Figure 7.16: Force - displacement curve BCZTTi 1.4 750℃